Designing Nano-Therapeutic Carrier Embedded Multifunctional Injectable Silk Hydrogels for Localized Targeted Cancer Treatment

A Thesis

Submitted in Partial Fulfillment of the Requirements for the Degree of

DOCTOR OF PHILOSOPHY

by

ANKIT GANGRADE

Department of Biosciences and Bioengineering
Indian Institute of Technology Guwahati
Guwahati-781039, Assam, India

Date: 31st December 2020

Designing Nano-Therapeutic Carrier Embedded Multifunctional Injectable Silk Hydrogels for Localized Targeted Cancer Treatment

A Thesis

Submitted in Partial Fulfillment of the Requirements for the Degree of

DOCTOR OF PHILOSOPHY

by

ANKIT GANGRADE

Department of Biosciences and Bioengineering
Indian Institute of Technology Guwahati
Guwahati-781039, Assam, India

Date: 31st December 2020

Dedicated to my Family and Friends

INDIAN INSTITUTE OF TECHNOLOGY GUWAHATI

DEPARTMENT OF BIOSCIENCES AND BIOENGINEERING

STATEMENT

I hereby declare that this thesis's research findings are the result of research work carried out by me in the Department of Biosciences and Bioengineering, Indian Institute of Technology Guwahati, Guwahati, Assam, India, under the supervision of **Prof. Biman B. Mandal**.

As per the general norms of reporting research findings, due acknowledgments have been made wherever the research findings of other researchers have been cited in this thesis.

Date: 15/02/2021

Ankit Gangrade

INDIAN INSTITUTE OF TECHNOLOGY GUWAHATI

DEPARTMENT OF BIOSCIENCES AND BIOENGINEERING

CERTIFICATE

It is certified that the work described in this thesis entitled "**Designing Nano-Therapeutic Carrier Embedded Multifunctional Injectable Silk Hydrogels for Localized Targeted Cancer Treatment**" by **Mr. Ankit Gangrade** for the award of the degree of **Doctor of Philosophy (Ph.D.)** is an authentic record of the results obtained from the research work carried out under my supervision in the Department of Biosciences and Bioengineering, Indian Institute of Technology Guwahati, India, and this work has not been submitted elsewhere for the award of any other degree.

CERTIFIED

Biman B. Mandal, Ph.D.

(Thesis Supervisor)

Date: 15.02.2021

Ankit Gangrade

(Candidate)

Roll No: 136106016

ACKNOWLEDGEMENT

I feel privileged to pen down my wholehearted gratitude towards all the wonderful people who have directly or indirectly extended their valuable assistance and contributed imperatively to the completion of this thesis work. I am fortunate to acknowledge each one of them below for their consistent support during my years of scientific journey.

First and foremost, I would like to express my sincere appreciation to my thesis supervisor and mentor, **Prof Biman B Mandal**, who showed faith in me and agreed to guide me when I had to change my supervisor in the third year of my Ph.D. I would be forever indebted to him for the freedom he gave me at every step to conduct this project. Prof. Mandal's investment in scientific discussions, comments, and suggestions contributed significantly to the quality of this work. Moreover, his insight and knowledge in the subject matter steered me through this research. He has always been a constant source of encouragement and motivation during the entire course of study. His examples and the things that he taught me will undoubtedly help me in my future career. Besides, I would also like to acknowledge my former supervisor, Dr. Piruthivi Sukumar, for teaching me calmly during the initial days of my Ph.D. and shaping me as a better individual.

I would also extend my gratitude to the members of my Doctoral committee, Prof. Aiyagari Ramesh and Dr. Bithiah Grace Jaganathan of the Department of Biosciences and Bioengineering and Dr. Kingsuk Mahata of the Department of Chemistry for their valuable, constructive suggestions throughout this journey.

I would like to thank the present and former Heads of the Department, Prof. Latha Rangan, Prof. Kannan Pakshirajan, and Prof. V. Venkata Dasu, and the other faculty members for their support and teachings. I would like to acknowledge the Department of BSBE for providing the infrastructural facility for my research work. I would also like to recognize the Central Instrumentation Facility (CIF), IIT Guwahati, for providing high-end instruments to execute some of the experiments.

My Special thanks to Dr. Neeladri Das, Chemistry department, Indian Institute of Technology Patna, for including me in three collaboration projects and Dr. VGM Naidu, National Institute of Pharmaceutical Education and Research (NIPER) Guwahati for

providing access to the animal house facilities and constructive discussion on our tumor regression studies.

My special thanks to project collaborators and co-authors from other institutes Basweshwar Gawali (NIPER Guwahati), Khushwant Singh (IIT Patna), Achintya Jana (IIT Patna), Saurav Bhowmick (IIT Patna). I would also like to acknowledge MS Pharma students Dipak Sahu and Vijay Bahadur Singh from NIPER Guwahati and undergraduate student Princy Aggarwal from Banasthali Vidyapith, Rajasthan, and Anupam Mishra from IITG whom I mentored in the course of their project work. It was great working with you guys. I will always miss such a good team.

It is my pleasure to thank all members of the BBM lab group who have given me a friendly and happy environment in the lab. I want to acknowledge the help I got from Joseph, Prerak, Yogendra, and Bibhas da for their constant co-operation when I started my work. The very beginning of my Ph.D. journey would not have been so smooth without your help; thanks a lot! My heartfelt thanks to the co-authors and team members from the group, Dr. Praveen Kumar, for helping me in experimental works. My special thanks to Dr. Rajiv Borah for sharing his knowledge and helping me with critical experiments. I would also like to thank all the lab members Dimple, Shreya, Janani, Ashutosh, Bibrita, Chitra, Souradeep, and Suvro for their feedback, co-operation, and great discussions. I am also thankful to my former lab members Dr. Manishekhar, Dr. Rocktotpal, Dr. Chandramauli, Dr. Bhaskar, Dr. Biswajeet, Dr. Deepika, Dr. Aparajita, Dr. Vimal, Sangeeta, Monisha, Prerna, Triya, Sakshi, Tarishi, Namit, Omkar, Smriti, Rishabh, Kedarnath, and Sonu for their great company during my Ph.D. journey. My gratitude toward Dr. Nandana Ma'am for cheering with us in all the lab celebrations. Thank you all for constantly providing me a friendly environment in the lab. I am grateful to all of you for your constant support, encouragement, and suggestions for this work. We have gathered some great memories while working together as colleagues and even more recollections as friends. I would always cherish the memories I made with all of you, who have played varied roles of colleagues, life coaches, teachers, and mischief-makers, thus making the journey a memorable experience.

My next thanks go to my alma mater, IIT Guwahati, which gave me an opportunity of embarking on this exceptional endeavor of learning with ample facilities and an equally

enchanting natural bounty of the North-east. I have no words to explain the beauty of this campus.

Next, I would thank the funding agencies that provided me the financial support to conduct my research. I am grateful to the Ministry of Human Resource Development (MHRD) for the fellowship during my Ph.D. tenure. I would also like to acknowledge the funding support from the Science and Engineering Research Board (SERB), Govt. of India.

I wish to acknowledge my ex-labmates Anuj, Abhishek, Shweta, Vinod, Ajay, Vivek and friends Rakesh, Ashish, Amrendra, Reshmi, Neha, Karukriti, Gaurav, Debika, Dibakar, Mohan, Ananya, Bhuvan, Bapi, Anwesha, for having enriched me as a person. I would like to thank all the individuals who supported me throughout and contributed significantly to the outcome of this dissertation; their time and effort are greatly appreciated. A very big thanks to all these people and other people who have made my stay in Guwahati as a memorable and enjoyable journey.

Finally, I would like to remember my grandparent's late Shri Kanchan Lal Gangrade and Smt. Laxmi Bai Gangrade parents Shri Gopal Das Gangrade, Smt. Jaybala Gangrade and family Ankur bhaiya, Shalinee bhabhi, Aditya, Priya, and Geetu, for their never-ending love, support, and patience towards me. It is their numerous personal sacrifices that have enabled me to reach this juncture in life. Simple thanks are not enough to convey my deep respect and gratitude towards my family.

Thanks to the Lord, the Almighty, for showering his grace at each and every step!

Ankit Gangrade

CONTENTS

ABBREVIATIONS

2D	Two Dimensional
3D	Three Dimensional
5-FU	5-Fluorouracil
A549	Lung Cancer Cell Line
AA	*Antheraea assama*
AG	Silver
AGS	Stomach Cancer Cells
ALK	Anaplastic Lymphoma Kinase
AMD	Age-Related Macular Degeneration
AMF	Alternating Magnetic Field
ANOVA	Analysis of Variance
Apaf-1	Apoptotic Protease Activating Factor 1
Au	Gold
bFGF	Basic Fibroblast Growth Factor
BM	*Bombyx mori*
BMNP	*Bombyx mori* Silk Fibroin Nanoparticle
BMP-2	Bone Morphogenetic Protein-2
BSA	Bovine Serum Albumin
CF	Carboxyfluorescein
CM	Curcumin
CTCL	Cutaneous T Cell Lymphoma
CTZ	Ceftazidime
Cyt-c	Cytochrome c
DCFH-DA	Dichloro-Dihydro-Fluorescein-Diacetate
DDS	Drug Delivery Systems
DEB	Drug-Eluting Beads
DLS	Dynamic Light Scattering
DMSO	Dimethyl Sulfoxide

Dox	Doxorubicin
ECG	Electrocardiogram
EDC	1-(3-Dimethylamino Propyl)-3-Ethyl Carbodiimide Hydrochloride
EDEA	2,2′-(Ethylenedioxy)-Bis-(Ethylamine)
FA	Folic Acid
FDA	Food and Drug Administration
fDOX	Free Doxorubicin aqueous solution
Fe_3O_4	Iron- Oxide
FESEM	Field Emission Scanning Electron Microscopy
FETEM	Field Emission Transmission Electron Microscopy
FR	Folic Acid Receptor
FTIR	Fourier Transform Infrared
G’	Storage Modulus
G”	Loss Modulus
Gly	Glycine
GOx	Glucose Oxidase
H & E	Haematoxylin and Eosin
H_2SO_4	Sulphuric Acid
HNO_3	Nitric Acid
HRP	Horseradish Peroxidase
I	Current
ICMR	Indian Council of Medical Research
IGF-I	Insulin-Like Growth Factor-I
IL-2	Interleukin-2
KB	Oral Cancer Cell Line
LDH	Lactate Dehydrogenase
LVAW;d	Left Ventricular Posterior Wall Thickness Diastolic
LVAW;s	Left Ventricular Posterior Wall Thickness Systoli
LVE	Linear Viscoelastic
LVPW:d	Left Ventricular Posterior Wall Thickness Diastolic

LVPW:s	Left Ventricular Posterior Wall Thickness Systolic
mm	Millimeter
MPA	Medroxyprogesterone acetate
MTT	Methylthiazolyldiphenyl-Tetrazolium Bromide
MTX	Methotrexate
NHS	*N*-Hydroxysuccinimide Ester
NIR	Near-Infrared
nm	Nanometer
NT	Untreated
OPDA	O-Phenylene-Diamine
P(NIPAAm-*co*-IA)	Poly(*N*-Isopropylacrylamide-*Co*-Itaconic Anhydride
PAGE	Polyacrylamide Gel Electrophoresis
PCL	Polycaprolactone
PCR	Polymerase Chain Reaction
PDGF-BB	Platelet-Derived Growth Factor-BB
PDI	Polydispersity Index
PDT	Photodynamic
PEG	Poly(Ethylene Glycol)
PEI	Poly(Ethyleneimine)
P-HEMA	Poly (2-hydroxyethyl methacrylate)
PI	Propidium Iodide
PLGA	Poly (DL-lactic-co-glycolic acid)
PPy	Polypyrrole
PTCL	Peripheral T Cell Lymphoma
PTT	Photothermal
PTX	Paclitaxel
PVA	Polyvinyl Alcohol
Py-β-CD	Pyrene Modified β-Cyclodextrin
rlFN-7	Recombinant 7-Interferon
RNA	Ribonucleic Acid
ROS	Reactive Oxygen Species

RT	Reverse-Transcribed
SAHA	Suberoylanilide hydroxamic acid
SDS	Sodium Dodecyl Sulfate
SF	Silk Fibroin
Silk@BMNP	Bombyx mori nanoparticles embedded silk hydrogel
Silk@cisplatin	Anticancer drug cisplatin loaded silk hydrogel
Silk@fDOX	Anticancer drug doxorubicin loaded silk hydrogel
Silk@SWCNT-FA/DOX	Folic acid modified single walled carbon nanotube loaded with anticancer drug doxorubicin embedded in silk hydrogel matrix
SPLC	Space Charge Limited Conduction
SWCNT	Single-Walled Carbon Nanotubes
T	Temperature
TAM	Tamoxifen
TDD	Targeted Drug Delivery
TRIPOD	2,4,6-Tris(P-Formylphenoxy)-1,3,5-Triazine
TUNEL	Terminal Deoxynucleotidyl Transferase-Mediated dUTP Nick-End Labelling
UV	Ultra Violet
v	Volume
V	Voltage
VEGF	Vascular Endothelial Growth Factor
W	Weight
W	Watt
WHO	World Health Organization
wt%	Weight Percentage
β-actin	Beta-Actin
γ	Shear Strain
δT	Change in Temperature
λ	Wavelength
ω	Angular Frequency

LIST OF TABLES

LIST OF FIGURES

Chapter 1

Introduction and Literature Review

Introduction and Literature Review

1.1. Introduction

1.1.1. Cancer

Cancer is a disease in which abnormal cells keep dividing without control. It is a non-communicable disease which has been recognized as the leading cause of deaths worldwide. Incidents of cancer are growing, and the rate of mortality is rising. An estimated 25% of deaths in the United States are due to cancer [1], where breast cancer is contributing the most [2, 3]. As per World Health Organization (WHO) report, globally reported new cases and deaths related to cancer would be 22 million and 13 million by 2030, and India will have 1.73 million new cases and 0.8 million cancer deaths, according to the Indian Council of Medical Research (ICMR). The northeastern region in India is reported as the highest cancer-prone zone, where Assam records the highest number of cancer cases trailed by Meghalaya, Manipur, Mizoram, Nagaland, Arunachal Pradesh, and Tripura. Oral cancer is the most common cancer in the world. India accounts for 30-40% of oral cancer out of cancers at all other sites. However, the habit of chewing tobacco adds the highest count (10%) of oral cancer from the Northeast region [4-6].

1.1.2. Types of Cancer

Generally, cancer is classified as either benign or malignant. A benign tumor is not a life-threatening solid mass of the tumor; However, malignant tumor multiplies rapidly and invades other healthy tissues for its spreading [7]. Further, based on the type of cell affected cancer can be divided into carcinoma, sarcoma, leukemia, and lymphoma. Carcinoma is characterized by abnormal growth of epithelial cells that form inner or outer linings of various tissue/organs. The cancer of lung, skin, ovary, pancreas, oral, and gastric are some typical examples of carcinoma. Sarcoma is the cancer of the bone and other soft tissues such as cartilage, blood vessels, etc. Leukemia is the cancer of the blood, and lymphoma affects lymphocytes in the lymph nodes.

1.1.3. Treatment of Cancer

Cancer is a complex disease to treat. Many diseases such as typhoid, malaria, pneumonia, tuberculosis arise due to various microbial attack that is different than the host human cell type. Hence for curing such diseases, antibiotics are administered that specifically target the microbes without affecting the host cells. In contrast, cancer arises due to the aberration/mutation of the cells of our own body. Therefore, the selective killing of cancer cells without affecting healthy cells is a difficult task. For cancer therapy, three primary treatment options are available as follow –

Cancer is a complex disease to treat. Many diseases such as typhoid, malaria, pneumonia, tuberculosis arise due to various microbial attack that is different than the host human cell type. Hence for curing such diseases, antibiotics are administered that specifically target the microbes without affecting the host cells. In contrast, cancer arises due to the aberration/mutation of the cells of our own body. Therefore, the selective killing of cancer cells without affecting healthy cells is a difficult task. For cancer therapy, three primary treatment options are available as follow –

1.1.3.1. Surgery

In this method surgeon surgically remove the tumor along with the peripheral healthy tissue to make sure no cancer cell left behind. However, some tumors can not be removed due to their remote location or irregular shape/size.

1.1.3.2. Radiotherapy

In this method, a tumor is exposed to a high dose of radiation to kill or slow down the growth of cancer cells for its shrinkage. However, it also damages the surrounding healthy tissues, which causes various side effects on the patient.

1.1.3.3. Chemotherapy

Chemotherapy is the most fundamental treatment option as it is prescribed to each cancer patient at some stage of their therapy [8, 9]. When tumor size is more prominent and difficult to remove by surgery than chemotherapy is used to shrink the tumor size; also, post-surgery, chemotherapy helps to avoid further cancer relapse. However, delivering chemo drugs through a systemic route causes various undesired side effects such as

vomiting, infertility, hair loss, anemia, fatigue, weakness, loss of appetite, fertility issues, etc.

1.1.4. Routes of cancer chemotherapy

Various routes for delivering drug molecules to treat cancer are listed in **Table 1.1,** along with their advantages and disadvantages. However, a brief discussion of the same is as follow –

1.1.4.1. Oral route

The oral route is the most popular route for administering the drug. The drug passes through the gastrointestinal tract to reach systemic circulation for effect. The drug is placed in the mouth and swallowed. This route gives tablets, capsules, and various liquids preparations.

1.1.4.2. Intravenous route

This is a parenteral route of administration in which drug is injected directly into veins for rapid action.

1.1.4.3. Intramuscular route

Drugs are injected into the deeper layer to tissue into muscles. Once the drug reaches to muscles, it absorbed into the blood.

1.1.4.4. Intraperitoneal route

This is a systemic route of drug delivery where the substances are injected into the peritoneum body cavity**.**

1.1.4.5. Subcutaneous route

This is a localized route of drug delivery in which the drug is injected into the fatty layer beneath the skin after crossing the cutaneous layer. It is absorbed into the blood. The drug in this route doesn't follow the first-pass metabolism.

1.1.4.6. Intraarterial route

The drug is administered into the artery.

1.1.4.7. Inhalation

In the process, **t**he substances are administered through the air into the lungs.

Table 1.1. Various routes of anticancer drug administration for cancer chemotherapy.

Broad Classification	Drug Delivered	Type Of Cancer Treated	Advantage	Disadvantage	Ref.
Oral	Indolinone derivatives, Green tea catechins extract, Capecitabine, Thalidomide with dexamethasone, Curcumin, Idarubicin, Exemestane, SCH 66336, 5-Fluorouracil, Etoposide, PNU-159548, Temozolomide, Medroxyprogesterone acetate (MPA), STI 571 (imatinib)	Thyroid, Prostate, Colorectal, Breast, Pancreatic, Multiple myeloma, Colon, Testicular, Ovarian, Endometrial and small cell lung cancer.	Suitable for self-medication, Easy to take, Cheap, Acceptable by most people, The flexibility of time and flexibility of drug exposure	Compromised by irritant effects/presence of food, Enzymes action may limit effectiveness, Effect slow for emergencies, odynophagia, nausea, and vomiting	[10] [11] [12] [13] [14] [15] [16] [17] [18] [19] [20] [21]
Intravenous injection	Daunorubicin, Doxorubicin, Bortezomib, Abraxane, fluorouracil (fu)/leucovorin, Cyclophosphamide and cisplatin, PNU-159548, Amifostine, Cisplatin, Oxaliplatin	acute leukemias, Multiple myeloma, Mantle cell lymphoma, Metastatic breast, Colorectal, testicular Ovarian, head and neck cancer	Precise, accurate & Rapid action, The large volume of the drug can be administered, Avoid the first-pass metabolism	Relatively high cost, The skill needed for the administration, Risk of extravasation	[22] [14] [23] [24] [25] [26] [27] [28] [19] [29] [30]

Intra-muscular injection	4-Hydroxy-androstenedione, Fulvestrant, recombinant 7-interferon (rlFN-7), Epidermal growth factor-based cancer vaccine, recombinant baculovirus containing human CEA	Metastatic breast, and non-small-cell lung cancer	Bypass gastrointestinal tract, Depot, and slow-release preparations can be given, Good absorption	Irritation at site of injection, Skilled person required, Painful, Nerve damage	[31] [15] [32] [33] [34]
Intra-peritoneal injection	liposomal siRNA, Cyclophosphamide, Doxorubicin, Mitomycin, Cisplatin, Cytosine arabinoside, IL4-Pseudomonas exotoxin, Oxaliplatin, Irinotecan with 5-fluorouracil, Carboplatin, Docetaxel, Adriamycin	Ovarian, Peritoneal appendiceal, mesothelioma, Colorectal, Gastric, Pancreatic and Hepatic cancer	Useful for peritoneal dialysis, The most preferred route in laboratory animals	Painful, Risk of peritonitis	[35] [36] [37] [38] [30]
Sub-cutaneous injection	Amifostine (WR-2721), Bortezomib	Head and neck cancer, Multiple myeloma	Absorption is slow but complete, Bypass gastrointestinal tract, Produce local effects	Drugs can cause local tissue damage,	[29] [39]
Intra-arterial injection	drug-eluting microspheres/beads (DEB) loaded with doxorubicin	Liver cancer	Maximize drug concentration at the site		[40]

Inhalation	14Ctagged doxorubicin, Interleukin-2 (IL-2)	Lung cancer, renal cell cancer and melanoma	Rapid absorption, Avoid gut enzymes, Limits systemic absorption	Pain does not occur because the injection is not given, Need specialized drug delivery system	[41]

1.1.5. Nanocarriers for anticancer drug delivery

For cancer therapy, various potential chemotherapeutics have been explored, as shown in **Table 1.1** above; however, their inability to discriminate between healthy and cancerous tissue, loss of action in blood serum, and burst release limits their use. Additionally, their delivery is also an issue due to lack of solubility in water. Using nanocarrier for drug delivery is advantageous as it showed promising results in reducing the side effects of the anticancer drug by actively targeting it precisely into the tumor.

Nanocarriers are having a diameter size range of 1 to 1000 nm. The nanoparticles improve the anticancer drug therapeutic index by enhancing its uptake and localization in the target tumor site. Few examples of highly explored nanocarriers are listed in **Table 1.2** along with the column for the anticancer drug they carried and cancer treated as follow –

Table 1.2. A list of various nanocarriers carrying anticancer agents for cancer treatment.

Nano-carriers	Drug delivered	Type of cancer treated	Advantage	Ref.
Prodrugs	Capecitabine, Pracinostat (SB939), HDACi Zolinza (Vorinostat/ Suberoylanilide hydroxamic acid [SAHA]), Romidepsin (FK228)	cutaneous T cell Lymphoma (CTCL), peripheral T cell lymphoma (PTCL	Control release of the incorporated drug, Higher oral bioavailability, prevent drug from digestive degradation, Increase absorption of poorly soluble drugs, Stability & tunability	[42] [43]
Dendrimers	Doxorubicin, Doxorubicin, platinum-based drugs, Vinblastin, Vincristine, Topotecan, Paclitaxel	Metastatic stomach cancer	Enhance absorption of the drug, enhance permeability of co-administered drug, Alter gastrointestinal barrier	[43] [44]
Micelles	Paclitaxel, Doxorubicin, Platinum-based drugs, Camptothecin, Tamoxifen, Epirubicin	Metastatic or recurrent solid tumors, pancreatic, gastric, bile duct & colonic cancers	Act as a vehicle for poorly water-soluble drugs	[44]
Liposomes	Annamycin, Lurtotecan, Topotecan, Paclitaxel, 5-fluorouracil (5-FU) and methotrexate (MTX), Doxorubicin	Solid tumors, renal cell carcinoma, mesothelioma, ovarian and acute lymphoblastic leukemia, Ovarian cancer, Ovarian cancer and Kaposi's sarcoma	Protect the entrapped drug from digestive degradation, Enhance oral bioavailability, Increase absorption of poorly soluble drugs	[44] [43] [45]

Carbon nanotubes	Methotrexate, Taxoid, Doxorubicin, Cisplatin, Paclitaxel	Leukemia, Colon cancer, Squamous carcinoma, Nasopharyngeal epidermoid carcinoma etc, Cervical carcinoma, Breast cancer	Ultra-high surface area, Cross cellular barriers	[46] [47]

However, nanocarriers may induce the undesired immune response, and due to their systemic route of delivery, drug localization at the tumor site is insufficient. These limitations of current therapy motivated researchers to look into an alternate "localized" way for delivering drugs.[48, 49]

1.2. Review of Literature

1.2.1. Hydrogels for localized drug delivery

Cancer is a chronic disease which requires a long term of interaction with chemo drug for the efficacious therapeutic effects. Therefore, the local route of delivery could be a potential way of treating cancer. Wherein, the anticancer drug could be carried by a slow drug releasing reservoir while implanted near/intratumor site. Hydrogels are one of the preferred choices of drug reservoirs due to their injectable nature, which favors their implantation in a minimally invasive way. Hydrogels are three-dimensional, cross-linked networks of water-soluble polymers. Hydrogel, particularly those which are intended for drug delivery or biomedical purpose, should be made of biocompatible and biodegradable biomaterial. The polymeric biomaterials are classified as natural and synthetic based on their origin. The natural biomaterials include agarose, alginate, chitosan, gelatin, fibrin, silk fibroin, and hyaluronic acid. However, synthetic biomaterials include poly (DL-lactic-co-glycolic acid) (PLGA), poly(2-hydroxyethyl methacrylate) (P-HEMA), Poly(hydroxypropyl methacrylate), Poly(Acrylamide), Poly(Methacrylamide) and Derivatives, Poly(Vinyl alcohol), Polyelectrolyte complexes, Poly (N-Vinyl-2-Pyrrolidone) etc. [50-52]

Post local implantation, the drug release from the hydrogel can be triggered and controlled by either endogenous stimuli such as pH, redox condition, enzymes, or exogenous stimuli such as electric field, magnetic field, near-infrared laser, ultrasound or their multiple combinations. Such materials that respond to environmental change are known as “smart biomaterial.” It is exceptional to have all the smart properties in a single material. Therefore, the nanocomposite materials development approach is getting attention, wherein two materials with different properties are mixed to form a newer material having features of both of its constituents.[53, 54]

1.2.2. Silk fibroin

Silk fibroin is a natural protein polymer and has been utilized as a textile material from ancient times. Silk fibroin protein obtained from mulberry *Bombyx mori* cocoon has been extensively studied for biomedical applications due to its intrinsic properties like biocompatibility, high tensile strength, flexibility, water vapor permeability, tissue compatibility, high oxygen permeability, amenability to multiple processing formats and tunable biodegradation rates. Silk protein extracted from non-mulberry family e.g., tasar

(*Antheraea mylitta*), temperate oak tasar (*Antheraea pernyi*), muga (*Antheraea assama*), and eri (*Philosamia ricini*) has come into focus only recently. Studies have also revealed the comparative moisture regain ability and biocompatibility in terms of cell attachment, proliferation, migration and differentiation of different varieties of silk. In this context, various mulberry and non-mulberry based silk, due to their unique bio-physicochemical attributes, hold immense potential for the fabrication of injectable hydrogels. Aqueous solutions of silk fibroin undergo self-assembly giving rise to the formation of β sheets, which results in hydrogel formation. It is also possible to fine-tune the release kinetics by controlling the secondary structure of silk fibroin.[55-57]

1.2.3. Silk fibroin for delivery of bioactive molecules

SF, a well-characterized structure, with predominant hydrophobic block copolymer forms stimuli-responsive self-assembly in aqueous solution. Self-assembly of SF is highly controllable [58]. External stimuli such as fibroin concentration, pH, ionic strength, shear stress, and temperature of the solution increase its β-sheet content and form permanent intermicellar and interglobular crosslinks. The silk material format available to be used as DDS is mainly composed of β-sheets, β-turns, helices, and random coils [59]. External stimuli can be used to regulate the cross-linked network of SF scaffolds which is directly correlated with the controlled release of drug molecules through facilitated diffusion [60]. Proteolytic enzymes predominantly secreted in the body cleaves SF protein at several cleavage sites and release soluble amino acid or peptide fragments along with drug [61]. Therefore, by controlling the degradation pattern of silk structure, drug release kinetics can be regulated. The degradation profile of SF depends on several critical factors including (i) the site of implantation, (ii) concentration of SF, (iii) crystallinity of SF matrices, (iv) type of protease enzymes at the implantation site and (v) the animal model [62]. The conformation of the SF matrices can be directly tuned to control the release rate of the drug at the implantation site. For example, higher the β-sheet content, concentration, crystallinity of the SF matrices and lower the porosity of the SF matrices reduce the degradation rate, thus lowering the release profile of the drug [62, 63]. Due to these intrinsic characteristics, SF has been used in various formats like silk scaffolds in delivery of bioactive molecules with loading quantity and release profile are presented in **Table 1.3.**

Table 1.3. Various formats of implantable silk scaffolds in bioactive molecules delivery with release profile pattern.

Format	Delivered bioactive molecule	Release profile	Application	Ref
Porous Scaffolds	Bone morphogenetic protein-2 (BMP-2)	Sustained release for 21 days	Bone formation and repair	[64, 65]
	Antibody (IgG) and protein (5P12-RANTES)	Sustained release for 31 days	Prevention of HIV	[66]
	Cisplatin	Sustained release for 30 days	Localized neuroblastoma treatment	[67]
	Horseradish peroxidase (HRP)	NA	Enzyme stabilization	[68]
	BSA and FITC-Inulin loaded on calcium alginate beads	Tunable and sustained release for 35 days	Dual drug delivery system	[69]
	Gentamycin loaded on calcium alginate beads	Sustained release for 30 days	Drug delivery	[70]
	Aspirin	Sustained release (70 %) for 14 days	Treatment of *in vivo* Calvarial Defects	[71]
	PDGF-β and BMP-7 releasing recombinant adenovirus	Sustained release for 21 days	Bone regeneration	[72, 73]
	Insulin-like growth factor-I (IGF-I)	Linear correlation between loading and release for 29 days	Induction of chondrogenesis from human MSCs	[74]

	Vascular endothelial growth factor (VEGF)	Sustained release for 28 days	Bone regeneration	[75]
	Basic fibroblast growth factor (bFGF)	Sustained release for 24 h	Tissue regeneration	[76]
Films	HRP Glucose oxidase (GOx) from *Aspergillus niger* Lipase from *Candida rugosa*	Enzymes entrapped for 10 months at 37 °C	Stabilization of Enzymes	[77]
	VEGF	25% release for 4 days	For rapid vascularization	[78]
	Ocular drug delivery systems	NA	Transparent (>99 %) films	[79]
	Doxorubicin (Dox) and vincristine	Sustained release for 30 days	Deciphering silk-drug molecule interaction mechanism	[80]
	Anaplastic lymphoma kinase (ALK) inhibitors such as crizotinib and Dox	Sustained release for 30 days	Focal therapy of neuroblastoma	[81]
	Ciprofloxacin	Sustained release for 50 h	Wound healing	[82]
	Dox	45% release for 72 h	Cancer treatment	[83]
	Tetracycline hydrochloride	Release based on blending of SF/alginate ratio for 25 h	Antimicrobial drug release	[84]

	Azoalbumin, rifampicin and indigo carmine	Controlled release for 5 days	Regulated drug delivery	[85]
Nanofibers	Titanocene dichloride	Sustained release (85 %) for 6 days	Breast cancer treatment	[86]
	VEGF	Sustained release	Angiogenesis and bladder reconstruction	[87]
	Curcumin (CM)	Sustained release for 2 weeks	Implantable and controllable DDS for cancer treatment	[88, 89]
	Tamoxifen (TAM)	Sustained release for 22 days	Breast cancer therapy	[90]
	Ceftazidime (CTZ)	Controlled release for 6 h	To prevent infections for wound dressing	[91]
	Silver (AG)	65% release for 6 h	Antibacterial activity	[92]
	Dexamethasone	Prolonged release for 192 h	Inhibition of apoptosis and inflammatory damage in endothelial cells	[93]

Sterilization is a prime concern for any material to be used in drug delivery. *B. mori* SF possesses extraordinary mechanical strength and high thermal stability that helps to retain the structural stability during standard sterilization methods like autoclave without any degradation or change in properties [94]. Whereas, synthetic polymers such as PLGA or other natural polymers like collagen fails to retain structural stability. Aforesaid freedom to choose sterilization method makes silk a desirable matrix for sustained drug delivery [94]. Several research works have reported the cytocompatibility of the silk matrices using numerous cells types like fibroblast, keratinocytes, hepatocytes,

osteoblast, epithelial, endothelial, glial, stem cells and many more [55, 95, 96]. . *In vivo* implantation of different silk formats for DDS was also demonstrated. It is noted here, that reason behind some immunogenic response from SF is due to the presence of processing impurities (sericin) or contaminants like silkworm excretory products or dust [97]. Various formats of injectable silk scaffolds in delivery of bioactive molecules with loading quantity and release profile are presented in **Table 1.4**.

Table 1.4. Various formats of injectable silk scaffolds in bioactive molecules delivery with release profile pattern.

Form at	Fabrication metho	Delivered bioactive molecule	Release profile	Application	Ref
Hydro gels	Mulberry/non-mulberry silk fibroi blended with carbor nanotube	Dox	Triggered release for 14 days	Near infrared light dependent on demand drug release system	[55]
	Sonication induced gelation	miR-675 stem cell derived exosomes	Sustained release for 36 days	Prevention of aging induced vascular dysfunction	
	Sulfonic acid modified silk hydrogel	Cationic chemokine CXCL12	Sustained release for 5 weeks	Promoting stem/progenitor cell mobilization	[98]
	Temperature induce gelation	Diclofenac sodium	Sustained release for 35 h	Controlled drug delivery devices	[99]
	Vortex induced gelation	Graphene oxide, Dox	Triggered release for 21 days	Drug release system based on near infrared induction	[100]
	Chitosan/SF/glycero phosphate blends	Platelet-derived growth factor-BB (PDGF-BB)	Sustained release for 28 days	For stimulating DNA synthesis in Balb/c 3T3 fibroblasts and cell migration	[101]

	Silk/PEG blends	BMP-2, dexamethasone	Cumulative release for 60 days	Bone regeneration and to treat inner ear diseases	[102, 103]
	Temperature induce gelation	Dox	pH responsive drug release for 8 weeks	Localized breast cancer treatment	[104]
	Sonication induced gelation	anti-VEGF (bevacizumab)	Sustained release for 90 days	For the treatment of Age-related macular degeneration (AMD)	[105]
	SF/PVA/PEG blend	Aspirin, Indomethacin	Sustained release for 15 days	Drug release model	[106]
Micro / Nano sphere	Self-assembly of SI	FITC-Dextra	pH triggered release	Tunable drug release system based on external stimuli	[58]
	Ion induced SF nanoparticles	Lysozyme, dox, ibuprofen,	pH triggered release for 14 days	Controlled drug delivery system from non-mulberry silk	[61, 107, 108]
	Vortex induced silk nanospheres	Polyethylenimine , DNA	NA	Targeted gene delivery for treating cancer	[109]
	Ethanol precipitatio	BMP-2, BMP-9 or BMP-14	Controlled release for 14 days	Tissue engineering	[110]
	Acetone precipitation	Gentamicin	Release for 12 h	Showed antibacterial activity and supports adhesion, proliferation and differentiation of osteoblasts	[111]

Solvent diffusion method	Blue dextran 2000	Sustained release for 48 h	Controlled release based on ethanol	[59]
Encapsulation	Yeast cell wall polysaccharide loaded with carvedilol	Sustained release for 20 days	Core–shell biopolymer based drug delivery system	[112]

Traditional silk hydrogels usually possess inferior mechanical properties as well as lack multi-functionalities. Nano-sized particles/fillers, both inorganic and organic materials such as liposomes, dendrimers, polymeric micelles, carbon nanotubes, solid lipid nanoparticles, magnetic nanoparticles, silk fibroin nanoparticles have unique chemical, physical, and biological functions. They have been extensively studied for their efficient targeting and controlled drug release behavior for the treatment of cancer. The type of nanoparticle incorporated regulates the kind of stimuli that can be used to release the drug under the desired conditions, enhance the delivery in different parts of the body, allows the transport of hydrophobic drugs, or is responsible for multi stimuli-response behavior. Further, the functionalization of nanoparticles could deliver the incorporated drug to and nearby target cancer cells. Targeted delivery systems could deliver the drug with an effective dose to reduce systemic toxicity. Molecular targeting such as active or passive targeting can be accomplished for hydrogel nanoparticles for target site delivery of anticancer drugs. Nanocomposite hydrogels, which combine the advantages of both nano-fillers and hydrogel matrices, may result in improved mechanical and biological properties and find their potential applications in biomedical field.[55, 56, 113]

1.2.4. Nanocomposite smart hydrogels for stimuli triggered drug release

Nanotechnology has opened up new horizons in developing new modalities for delivery of therapeutic agents into targeted regions by having more efficient and high performance nanocarriers through which localized delivery is achievable [114, 115]. In this regard, designing nanosystems possessing multiple functionalities with great abilities has attracted the attention in developing DDSs. Smart materials having the capability to respond to various stimulus is becoming an important category of advance materials giving rise to stimuli responsive DDSs [114].

The triggering of drug release can be attained by local biological stimuli (e.g. pH, redox, enzymes) or by external sources (e.g. light/electromagnetic fields, focused ultrasound)[116]. Among these, multistimuli responsive DDSs have gained more attention due to their three dimensional (3D) hydrophilic polymer porous network that can be loaded with drug in considerable amount[117]. Drug diffusion into off- targeted regions is one of the major issue in DDSs. To overcome this, magnetic hollow porous carbon nanocarriers with pH, glutathione, and NIR triple-responsive property were fabricated. Also, multidrug resistance produced by chemotherapy was dealt by utilizing photo thermal conversion property of carbon and iron- oxide (Fe_3O_4). Tumor growth was effectively inhibited by efficient accumulation of nanoparticle at the tumor site with minimal side effects, as confirmed by in vivo studies[118]. Another liposomal system based on magnetic hyperthermia, photodynamic therapy and chemotherapy simultaneously enclosed by anticancer drug Doxorubicin enclosed in magnetic nanoparticles was reported. In vitro studies revealed that combined therapy almost completely eliminated the cancer cells[119].

The use of alternating magnetic field (AMF) to develop a non- invasive and localized heating by converting magnetic energy into local heat, has become very promising therapeutic modality in recent years. AMF have been preferred over other radiation methods, as it allows deeper penetration in the body with a less harmful ionization effect[116]. Light has been utilized in applications of intelligent targeted DDSs due to its ease of production, noninvasive nature and controllable intensity that can provide good control over the treatment process. However, all light activated systems suffer from limited light penetration into the tissue. Therefore, to have a better treatment plan internal stimulus can be combined with light activation leading to dual or multiresponsive smart DDSs[114]. Similarly, dual pH and thermo responsive DDSs are being extensively studied that are characterized by minimal toxicity, improved therapeutic efficacy and reduced exposure to normal cells[115]. **Table 1.5** shows the list of various smart materials for stimuli triggered drug release.

Table 1.5. Various stimuli for triggering drug release from smart biomaterials.

Stimuli	Material used	Drug delivered	Area targeted	Ref
pH & thermal responsive	poly(*N*-isopropylacrylamide-*co*-itaconic anhydride) [P(NIPAAm-*co*-IA)], poly(ethylene glycol) (PEG), and Fe_3O_4 nanoparticles	Doxorubicin	Cervical cancer	[117]
Enzymatic (proteinase K)	nanoparticles coated with glycine (F-Gly NPs)	MTX	Breast cancer	[120]
Ultrasound and static magnetic field	Calcined magnetic nanoparticle	MTX)	Colon and hepatocellular carcinoma	[121]
temperature-sensitive laser light drug release	Nanoparticle embedded in PEG–PLA polymeric composite	silibinin, SLB	NIH/3T3 fibroblast cells	[122]
Thermo/ chemotherapy *via* near-infrared (NIR) exposure	gold (Au)-coated implantable nanoturf	Doxorubicin	esophageal cancer model	[123]
pH- and near-infrared (NIR)-responsive	polypyrrole (PPy) coated paclitaxel (PTX)-loaded polycaprolactone (PCL) (PCL-PTX) mat	paclitaxel	Breast and colon cancer	[124]
Heat stimulus	methyl-terminated polyethylene glycol *N*-Hydroxysuccinimide ester (PEG-NHS)	carboxyfluorescein (CF)	FaDu human epithelial carcinoma cell line	[125]

1.2.5. Carbon nanotubes nanocomposites for drug delivery

CNTs are getting extra attention due to their potential advantages over other extensively studied metal nanoparticles (**Figure 1.1A**). The high aspect ratio of CNTs allows them to carry a heavy amount of drug molecules along with the ligand for ligand-target interaction. Besides, extremely low weight favors its cellular uptake, provides stability to the drug for its longer circulation time, enhance bioavailability and apt biodistribution [126-128]. SWNTs have extensively been investigated for their potential delivery of nucleic acid [129], protein [104], and drug molecules [130, 131]. Easy surface modifications of CNTs allow the conjugation of ligands for ligand-target interaction. Scientists have also reported the efficient tumor-targeted drug delivery using functionalized CNTs both *in vitro* and *in vivo* [132]. CNTs have also been explored for its photothermal property. Photothermal therapy involves the conversion of light energy into heat energy to kill the cancer cell. Near-infrared (NIR) light with a wavelength range from 650 to 1350 nm can penetrate deeply into biological tissue without its absorption. These nanoparticles, like CNTs, get heated when illuminated with NIR light. Interestingly, scientists have shown that CNTs destroy the solid malignant tumor due to excessive heat generated by continuous NIR irradiation. They have also reported the efficiency in terms of minimal side effects and non-recurrence of tumors [133, 134].

Although CNTs have been proved as an efficient carrier of the drug, however, they still have not passed the clinical trials. Since CNTs directly enter into the body it is essential to understand their interactions with biological tissue, did they initiate any cellular signaling pathway, how long they will stay in circulation, whether they are biodegradable, what are their byproducts, and if they are causing any toxicity; these clinical aspects remain unresolved limiting CNTs application in medicine. There is a controversy about the degradation of CNTs and their toxicity. A recent study has thrown light on CNT's feasibility to be enzymatically degraded by neutrophils and macrophages. The study also suggested that biodegradation of CNTs could be determinant of their inflammatory response [135]. CNTs have also been used as the substrate for the neuronal cell growth [136] and osteoblast cell [137] where surface charge and texture of CNTs determine the growth [138]. However, several reports suggested that dose and time-dependent exposure of CNTs to mice may cause adverse effects on the lungs [139], spleen [140], and liver [141]. CNTs also cause oxidative stress and affect embryonic

growth [142]. In summary, the toxicity of CNTs is dependent on the size, length, diameter, and whether they are functionalized or not.

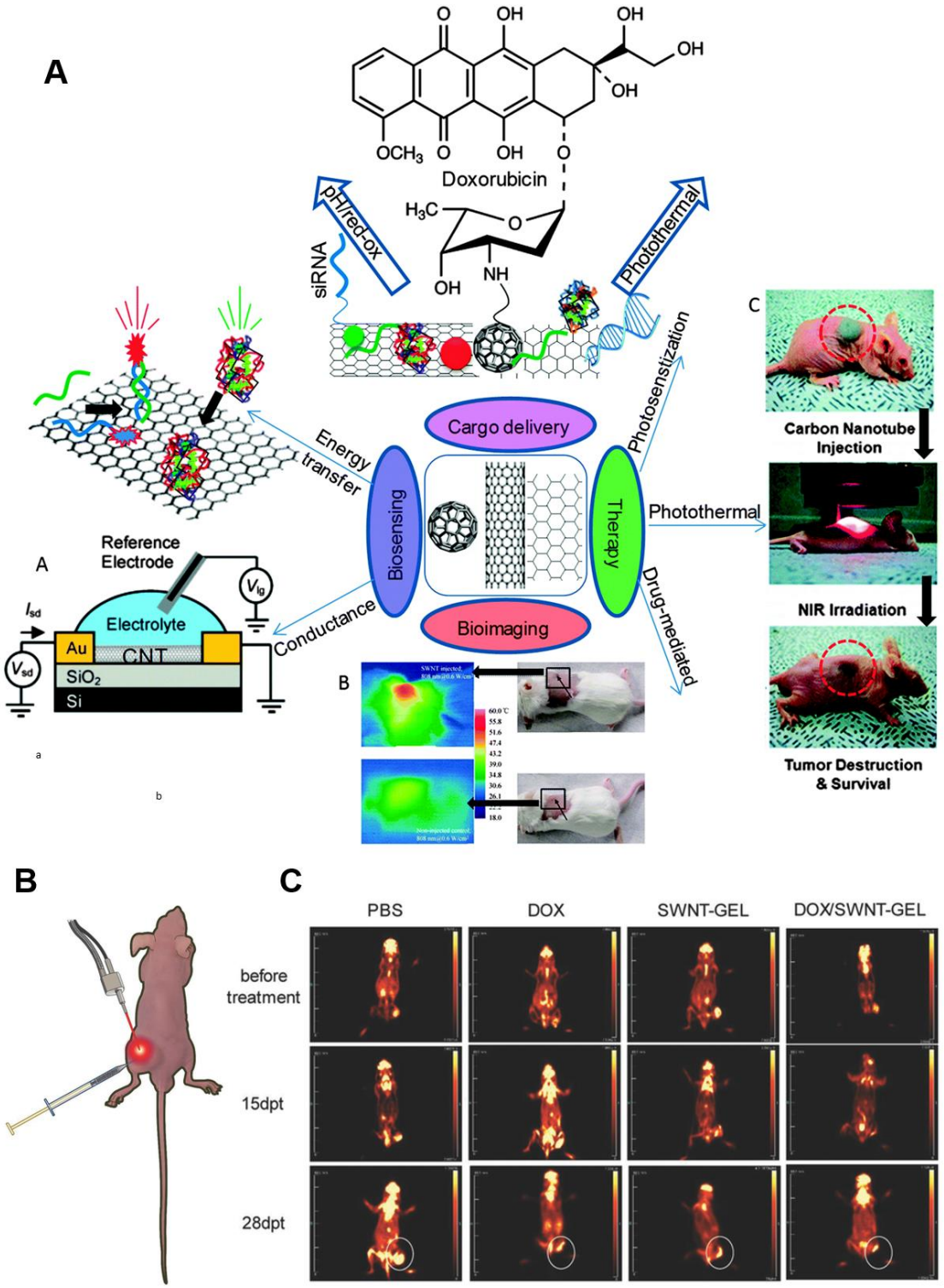

Figure 1.1. (A) *Biological application of CNTs (a) electrochemical sensor based on CNT, (b) CNT in thermal imaging in vivo (c) mice tumor therapy using CNT [143],* ***(B)*** *Intratumor injection of DOX/CNT-Gel nanocomposites into tumor mice model for photothermal therapy [144] and* ***(C)*** *Time-dependent tumor reduction observed through*

micro PET-CT scanning of mice post DOX/CNT-Gel delivery, illustrating the efficiency of chemo-photothermal treatment [144].

Scientists are now focused on how the toxicity and solubility issue of CNTs can be solved. Here incorporation of CNTs into a polymer for drug delivery could be advantageous. As polymer coating onto CNTs reduces their toxicity. The integration of CNTs into the hydrogel can be achieved by covalent or non-covalent interaction or their homogenous stabilization in the polymer chains of hydrogel matrix [145, 146]. Homenick et al., incorporated poly(ethyleneimine) (PEI) functionalized SWNTs or pristine SWNTs into collagen hydrogel and tested Young's modulus. It was observed that PEI-SWNT dramatically enhances the mechanical properties of collagen hydrogels as compared to pristine SWNTs. CNTs functionalized with pyrene modified β-cyclodextrin (Py-β-CD) is a water-soluble form which has been incorporated into gel via the host-guest interaction [146].

A very common issue in utilizing CNTs is their degradation by the immune system post-administration into the blood. To prolong their circulation time in blood, PEG-based functionalization is advisable. PEG is a synthetic, biocompatible, and non-immunogenic polymer. It encases around the CNTs to form nanocomposites and low down the immunogenicity and prevent its nonspecific phagocytosis by RES so that to increase their half-life in the blood. The authors have also detected the presence of PEGylated CNTs inside the liver and spleen macrophage for 4 months with great compatibility [147]. Intracellular tracking of FITC labeled PEGylated nanocomposite of CNT also confirms that it can pass through the nuclear membrane in an energy-independent manner [148]. Interestingly, CNTs did not affect the nuclear organization and its structure as well as cell cycle and growth kinetics for up to 5 days. Moreover, it was observed that CNTs intake and excretion are bidirectional reversible processes, i.e., if removed from the culture media, CNTs come out from the nucleus into the cytoplasm and then excreted out from the cells [148]. Scientists have also coated folic acid-terminated PEG (PEG-FA) on SWNTs in a facile non-covalent method followed by DOX to target cancer cells [149]. CNTs functionalized with chitosan were incorporated to poly(acrylamide-co-acrylic acid) hydrogels, and *in vitro* toxicity was assessed on intestinal cells [150]. In a similar approach, a crosslinker 2,4,6-Tris(p-formylphenoxy)-1,3,5-triazine (TRIPOD) has been used to form a chitosan-MWNTs nanocomposite hydrogel. The developed nanocomposite hydrogel was mechanically more robust with

enhanced stability. They also inhibited the burst release of drug initially and followed by slow and sustained release (at different pH conditions) compared to control chitosan hydrogel. Authors have also suggested that drug release can be tuneable by varying MWNTs concentration into chitosan hydrogel [151]. Gelatin-CNT hybrid nanocomposite films have been used to deliver anionic drugs and drug release studies were performed at variable temperature and voltage. Likewise, stimuli responsive drug release has also been observed in polymer/CNT nanocomposites [152].

The photo-thermal property of CNT can be utilized by its accumulation into the tumor. Intravenous delivery of CNTs causes its systemic distribution and lowers the chance of its gathering to the tumor. Therefore, scientists are trying to use polymeric hydrogel systems, which can hold the CNT and could be directly injected intratumorally as shown in **Figure 1.1B**. The strategy above is expected to have enhanced NIR triggered photothermal therapy [153]. Co-delivery of anticancer drugs loaded on to CNT-polymer nanocomposite has been tried, and subsequently, drug release triggered by photothermal effect has been reported. This may ensure better results due to chemo and photothermal therapy together (**Figure 1.1C**) [144, 154, 155].

MOTIVATION AND OBJECTIVES

OF THE PRESENT INVESTIGATION

MOTIVATION AND OBJECTIVES OF THE PRESENT INVESTIGATION

Among various cancer treatment options, chemotherapy remains the most common. Chemotherapy is often challenged by severe cytotoxic side effects, fluctuating blood concentrations, and limited drug assesses to cancer regions. These limitations of the traditional anticancer drugs are their side effects caused during and after the treatment. The current need of an injectable hydrogel system that could on-demand release the anticancer drug post its implantation in a minimally invasive way locally at near/intratumor site, motivated us to conduct the present study. Nanocarriers have unique properties and have been extensively studied in drug delivery applications. Nanocomposite hydrogels, which combine the advantages of both nano-fillers and hydrogel matrices, may result in improved mechanical and biological properties in the biomedical field. The origin of the present research work and the salient motivating factors are as follows::

1. The current conventional chemotherapy with multiple cycles of systemic administration has high systemic toxicity and low bioavailability in the hypoxic and necrotic zone of cancer, leading to low efficacy and higher recurrence. This motivated us to develop a novel minimal invasive injectable hydrogel system loaded with drugs that can be injected in the core of solid cancer under image guidance. We are hopeful that such a system may have higher efficacy, lower systemic toxicity, and may reduce the need for hospitalization of patients for repeated cycles of chemotherapy.
2. In drug delivery, despite numerous applications, there are no current systems available for controllable, sustained, and targeted drug delivery via fully degradable implants. Recently, injectable hydrogels that are formed in situ after injection have been receiving much attention for treating these problems. Currently available hydrogels face issues related to cost, allergic responses, poor tunability, and complicated manufacturing processes. In the context of the afore-stated issues, we intend to fabricate an injectable model system for drug delivery

that would be instrumental in elucidating a novel, facile, green and fast strategy based on the unique material properties of polymeric bioresource, i.e., silk.

3. Silk is an FDA approved natural biopolymer which has been shown tremendous biomedical application. Further, silk is a naturally degradable biopolymer having no harmful effects on the environment. The biomedical prospects of the endemic silk varieties of North East India, e.g., *A. assama*, the golden yellow fiber of Assam has received geographical indication status. Due to our Institute/laboratory location (Assam), we have direct access to this underexplored silk variety for manufacturing processes. The abundant silk protein availability and facile hydrogel fabrication methods further motivated us to work on this project.
4. In our lab, we developed a green method of silk hydrogel preparation, which does not require the use of any harsh chemicals or external stimuli such as vortex, sonication, heat, and pH to form the hydrogel. Interestingly, mulberry (*B. mori*) and non-mulberry (*A. assama*) silk protein blending induced the rapid formation of robust hydrogel within a few minutes. The blending method also provides feasibility to incorporate the drug(s) loaded nanocarrier for injectable nanocomposite hydrogel formation. The formed hydrogels can also be sterilized by autoclave, which brings another advantage to this system and motivates us to explore it further.
5. Although silk fibroin protein-polymer has numerous excellent properties, it is nonconductive and nonresponsive to external stimuli, which burst release all it's content. The flexibility to mix nanocarriers with silk polymer blend motivated us to develop new nanocomposite smart materials with superior drug-releasing properties.
6. The silk fibroin nanoparticles have been extensively studied all around the globe in delivering various hydrophilic/hydrophobic/charged anticancer drugs. In one of our approaches, we aim to embed the silk fibroin nanoparticles in the silk hydrogel to assess its sustained drug delivery efficacy.
7. Single-walled carbon nanotubes (SWCNT) offer many advantages individually for drug delivery applications. Their surface can be modified for target cancer cell-specific drug delivery. Additionally, SWCNTs exhibited electrical conductivity and NIR radiation-induced photothermal property. Motivated from these features, in our second approach, we aim to embed SWCNT in silk hydrogel

to explore the superior externally addressable properties of nanocomposite hydrogel for localized, targeted drug delivery.

8. In an extensive literature survey, we did not find any 3D cell culture system available to study the interaction between injectable hydrogels and cancer cells *in vitro* for its functionality assessment. This gap further opened the scope for us to design a silk-based scaffold prototype that can support the growth of the cancer cells and provide a space for the injectable hydrogels at the same time to study the long term interaction between cells and the hydrogel.

In light of the enormous scope of exploring various nanocarriers loaded anticancer drugs in association with silk biomaterials, we would like to develop smart hydrogels as vehicles for localized, cancer-targeted externally addressable drug delivery applications. We analyzed our different hypothetical strategies through the following objectives:

Objectives:

1. *B. mori* silk fibroin nanoparticle (BMNP) impregnated injectable silk hydrogel for sustained delivery of cisplatin and its *in vitro* functionality assessment in 3D cultured stomach cancer cell model.

2. Single-walled carbon nanotube (SWCNT) impregnated injectable silk hydrogel for folic acid receptor overexpressing oral cancer cell-targeted doxorubicin delivery.

3. Assessment of photo electro-active minimally invasive injectable silk hydrogel in *in vivo* breast tumor mice model for spatiotemporal controlled release and tumor therapy..

भारतीय प्रौद्योगिकी संस्थान गुवाहाटी
Indian Institute of Technology Guwahati

Chapter 2

Bombyx mori Silk Fibroin Nanoparticle (BMNP) Impregnated Injectable Silk Hydrogel for Sustained Delivery of Cisplatin and its *In Vitro* Functionality Assessment in 3D Cultured Stomach Cancer Cell Model

This Chapter discusses the preparation of silk-based nanohybrid hydrogel system and scaffolds to fill up the current gap in evaluating the soft injectable hydrogels in vitro for sustained drug delivery applications.

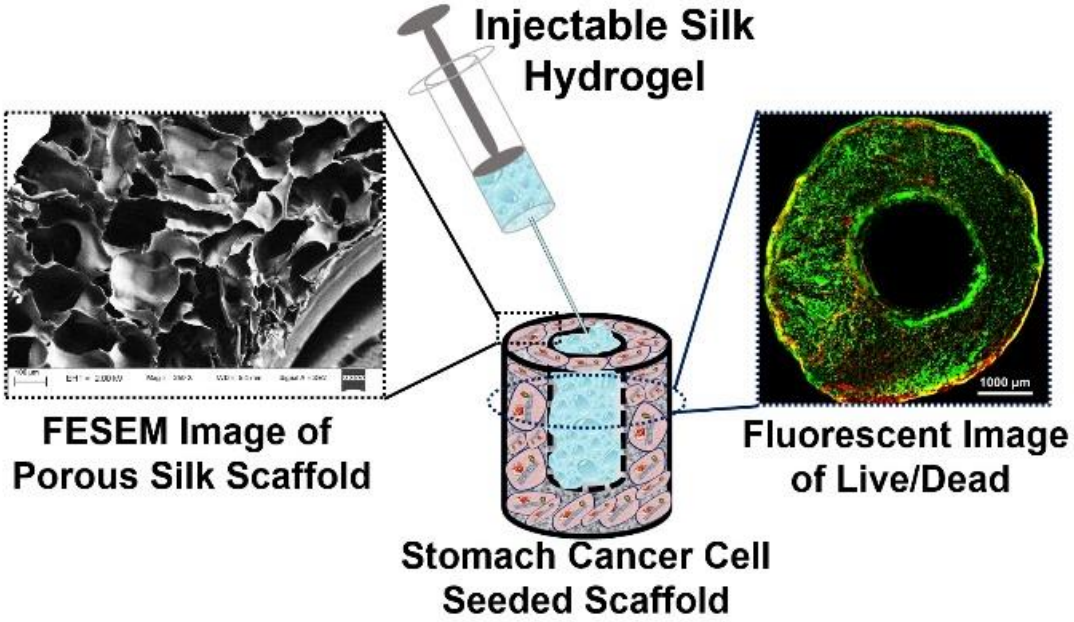

The work embodied in this chapter is published in a peer-reviewed journal as follow: **Ankit Gangrade** and Biman B. Mandal. "Development of 3D Porous Silk Scaffold for In Vitro Evaluation of Injectable Hydrogels Potential in Preventing Stomach Cancer Growth and Recurrence" ***ACS Biomaterials Science & Engineering*** 5, (2020) 6, 11, 6195–6206. (IF – 4.152).

ABSTRACT

Localized cancer chemotherapy through injectable hydrogels is a next-generation advanced substitute for the currently operative systemic route of drug administration. Recently, several hydrogels have been developed for prospective drug delivery applications; however, no *in vitro* disease model is available to evaluate its long term bioactivity in real-time. In this regard, we have designed a porous silk scaffold that provides a single platform to accommodate both soft hydrogel and cancer cells together. The stomach cancer (AGS) cells were seeded in the periphery of the silk scaffold, where they sit in the pores and form 3-dimensional (3D) spheroids. Further, the anticancer drug cisplatin loaded nanocomposite injectable silk hydrogel was filled in the central cavity of the scaffold to evaluate its 11-day extended bioactivity. In an attempt to model cancer recurrence, the AGS cells were reseeded on the second day of treatment. Our data revealed that the shelf life and cytotoxic effects of cisplatin, which was explicitly releasing out from the nanocomposite silk hydrogel, was considerably enhanced. Hence, the reseeded AGS cells did not survive further on the scaffold, which also indicates its ability to inhibit the cancer relapse. Conclusively, the current work showed a possible way to evaluate the long term efficacy and bioactivity of injectable hydrogel system *in vitro* for sustained drug delivery application.

2.1. Introduction

Cancer is a chronic disease that requires sustained/prolonged exposure to anticancer drugs for sound therapeutic effects.[156] The current gold standard cancer chemotherapy procedure involves the administration of anticancer drugs directly into the veins, which distributes these highly cytotoxic drugs all over the body and produce various undesired side effects.[157] Also, maintaining a steady blood plasma level of medications through the conventional/intravenous drug delivery method is a painful and challenging process. Due to insufficient accumulation of drugs at the tumor site, the probability of postoperative cancer relapse is also high. "Localized" near/intratumor drug delivery methods, however, have been introduced recently and is now emerging as an alternative methodology of currently in effect systemic intravenous drug delivery method.[158, 159] Wherein, a depot/reservoir is required to restrict the drug locoregionally at the diseased site that could prevent cancer recurrence and inhibit its diffusion to the nearby healthy tissues as well.

Based on the method of implantation, depots could be divided into two categories; first, surgically implantable scaffolds that include films, sponges, microchips, microneedles, electrospun mats etc. and second, minimally invasive injectable systems that include hydrogels.[55, 160-164] Hydrogels are three-dimensional structures that hold more than 95% of water, and therefore have properties of both solids and liquids. They are the preferred choice of depot due to their high drug loading efficiency and injectable nature, which permits its local implantation in a minimally invasive way.[156] Hydrogels made up of various natural (collagen, gelatin, chitosan, silk fibroin, fibrin) or synthetic [poly lactic-co-glycolic acid (PLGA), Polyvinyl alcohol (PVA), Polyethylene glycol (PEG)] polymeric materials have been extensively studied and reviewed for their advantages/disadvantage in drug delivery application.[156]

Silk fibroin (SF) is a natural protein-polymer available abundantly all over the world and has been used as a textile material for our ancient times. They are susceptible to various proteases for their biodegradation and produce biocompatible, nontoxic, resorbable, amino acids as a by-product, which sought the researcher's attention to utilize it as a biomaterial in tissue engineering, and drug delivery applications.[160, 164, 165] Further, the SF protein can be processed into various formats such as porous scaffolds, films, nanoparticles, microneedles, and hydrogels based on the desired health care

applications.[55, 162, 165, 166] The mechanical strength and biodegradation rate of the silk made scaffolds are also tunable and can be controlled by their final wt% concentration.[55] Different methods such as vortex, sonication, change in pH, freeze-thaw cycles, and blending have been explored to induce the sol to gel transition of aqueous SF solution.[3, 55, 161, 167, 168] At low wt%, SF protein form soft and injectable hydrogels suitable for drug delivery applications; however, they have the drawback of frequent content release due to the loose crosslinking.[55] The nanocomposite hydrogel formation by inserting cargos carrying nano vehicles into the hydrogel matrix displayed the sustained payload release for a prolonged time duration.[55, 165] Such nanocomposite hydrogels have shown superior properties than both of its counterpart. Besides, silk has also supported the growth of numerous types of cells on its surfaces such as chondrocytes,[169] osteocytes,[170] adipocytes,[169] stem cells,[170] pancreatic cells,[171] hepatocytes,[96] cardiomyocytes,[172] cancer cells,[173] etc., for various tissue engineering, 3D disease modeling, and drug screening applications.

Conventionally, the screening of anticancer drugs begins with a two dimensional (2D) cell culture technique.[174] Wherein cancer cells are grown as a monolayer over the plastic surface and treated with test compounds for their cytotoxicity measurement. However, it is not necessary that these drugs should show similar anticancer effects *in vivo,* as shown in the 2D cell culture system, which is due to the complex microenvironment and three-dimensional (3D) arrangement of cancer cells in the tumor. Therefore, culturing cancer cells in 3D as a spheroid or over hydrogels/scaffolds is introduced to assess the cytotoxicity of the anticancer drugs before its testing into animals.[175-177] 3D cell culture also bridges the gap between 2D monolayer and *in vivo* tumor microenvironment. Additionally, with 3D culture techniques, actual human diseased cells could be grown for testing, which would best recapitulate the disease to yield results with high predictive values for clinical outcomes. Also, the drawbacks of the conventional mouse model, such as their high cost and associated ethical considerations, could be by-passed.

However, to our knowledge, there has been no model/design is available, which can be used to directly assess the functionality of drug molecules releasing from the depots in real-time. Currently, two *in vitro* methods are available to evaluate the functionality of drug molecule releasing from the depot; first, by incubating drug depot

into a separate vessel with cell culture media and use this media to treat the cancer cells cultured separately in either 2D monolayer or 3D scaffold.[55, 158, 178] Second, by using transwell plates, in which the drug depot is placed on the top of transwell, and cells are cultured in the bottom as a 2D monolayer.[161] Both these *in vitro* assessment techniques provide limited information due to no direct cell to depot interaction. Also, the incubation of soft hydrogels directly into aqueous media solubilizes its content and may give false information.

In present work, we have designed a cylinder-shaped porous silk scaffold with one end open and one end closed. The open-end design of these scaffolds form a cavity/space; wherein, the anticancer drug-carrying soft hydrogel could be injected, and in the periphery, cancer cells could be grown as 3D spheroids. Here, we propose that such a model could predict the long term functional activity of sustainably releasing anticancer drug molecules in real-time and may yield data that is close to the experimental animal studies.

2.2. Materials and methods

2.2.1. Isolation of SF protein from *Bombyx mori* (BM) cocoon and *Antheraea assama* (AA) silkworm glands

BM SF protein aqueous solution was isolated from the cocoon as described previously.[55] Briefly, the chopped pieces of BM cocoon were boiled for 15 min in 0.02 M Na_2CO_3 to remove the sericin from silk fibers. The obtained silk fibers were dried and solubilized into 9.3 M LiBr solution. The working SF aqueous solution was collected post three days dialysis against Mili-Q water.

The AA SF protein aqueous solution was isolated directly from worm glands instead of the cocoon. The AA SF was squeezed from the gland manually in distilled water using forceps and dissolved in 1% sodium dodecyl sulfate (SDS) solution. The working AA SF solution was collected post four h dialysis against Mili-Q water.

2.2.2. Preparation and characterization of BM nanoparticle (BMNP)

BM SF nanoparticle (BMNP) was prepared using the desolvation method as previously done with modification.[179] 1.2 wt% BM SF solution was injected into 20 ml continuously stirring acetone through a syringe to form BMNP. The formed BMNP was aqueously suspended after acetone evaporation, and collected in supernatant post centrifugation at 8000g for 8 min. The aqueous BMNP was processed by lyophilization and obtained as the powder for further studies. The concentration of BMNP was determined by Bradford assay using BSA standard plot.

The characterization of BMNP was done using field emission transmission electron microscopy (FETEM), field emission scanning electron microscopy (FESEM), and dynamic light scattering. For the characterization, lyophilized BMNP was dispersed into water. A drop of approximately 10 µg/ml BMNP was dried over coverslip, and placed on the top of carbon tape. Successively, the coverslip was coated with gold before FESEM analysis. For FETEM analysis, BMNP dispersed in water air-dried over the carbon grid. Size distribution and zeta potential were determined using Malvern Zetasizer ZS90. For size distribution, 1 ml of BMNP water suspension was filled into a cuvette, and three measurements were performed where each measurement included 11 runs. For zeta potential 1 ml BMNP sample was added into U-shape cuvette, and three measurements were performed where each measurement was a result of 20 runs.

2.2.3. Preparation and rheological characterization of BMNP loaded nanocomposite silk hydrogel

Silk hydrogel was prepared by blending SF proteins isolated from BM cocoon and AA silkworm glands. For the preparation of hydrogel working stock of BM and AA SF solutions were blended in a 1:1 wt% ratio to make up to the final 2 wt% silk hydrogel. While blending two SF solutions, the aqueous suspension of BMNP was mixed at 25, 50, and 100 µg concentration to form the crosslinker free nanocomposite silk hydrogel.

The nanocomposite hydrogel formation was rheologically characterized using the Anton Parr MCR302 rheometer. For gelation time measurement, the blend of BM:AA:BMNP at 1:1:X wt% ratio was placed under the 1 mm gap of the parallel plate of the rheometer (where X is the variable concentration of BMNP). The parameters like shear strain (γ, 0.001%), angular frequency (ω, 20 rad/s), and temperature (T, 37 ^{o}C) were kept constant. The storage modulus (G') and loss modulus (G") values were recorded with increasing time and plotted to determine the gelation time. For the amplitude sweep determination, shear strain from 0.01 to 100 % was applied over the hydrogel/nanocomposite hydrogel, and angular frequency was kept constant at 3 rad/s. The obtained G' and G" values were plotted against shear strain. The frequency sweep was performed by applying variable angular frequency in the range from 1 to 100 rad/s and keeping shear strain constant at 10 %. We determined 10 % shear strain value under the linear viscoelastic region through amplitude sweep, hence it was selected and kept constant to conduct the frequency sweep test. The obtained G' and G" values were then plotted against angular frequency. From the frequency sweep experiment, loss factor (tan δ) and complex viscosity were also calculated, and both were plotted against angular frequency. The thixotropy study of hydrogel was done by applying low shear strain (10 %) and high shear strain (100 %) repeatedly for 3 times by keeping the angular frequency constant at 10 rad/s. The obtained G' and G" values were then plotted against time.

2.2.4. Preparation of BMNP-cisplatin conjugate and Silk@BMNP-cisplatin nanocomposite hydrogel

1 mg lyophilized BMNP was suspended into 1 ml water or a buffer of pH 4, 7.4, and 9.1. Cisplatin 3 mg/ml stock solution was then mixed with 1 mg/ml water/buffer suspended BMNP and incubated overnight at room temperature with shaking. The BMNP-cisplatin conjugate was separated by centrifugation as pellet, and free cisplatin was measured by

a colorimetric method in the supernatant to determine the cisplatin loading capacity over BMNP in a different pH buffer solution.

BMNP-cisplatin (100 µg BMNP-170 µg cisplatin) conjugates without removing the unbound cisplatin were prepared at pH 9.1 buffer and blended with BM and AA at 1:1 wt% ratio to form Silk@BMNP-cisplatin nanocomposite hydrogel. The equivalent amount of cisplatin was blended directly with BM and AA at 1:1 wt% ratio to form Silk@cisplatin hydrogel as a control.

2.2.5. *In vitro* drug release studies from Silk@cisplatin and Silk@BMNP-cisplatin hydrogel

The cisplatin drug release study from Silk@BMNP-cisplatin nanocomposite hydrogel and Silk@cisplatin hydrogel was carried out in three different buffers of pH 4, 7.4, and 9.1. The incubation buffer was collected at prefixed timepoint until 21 days study and replaced every time with a new buffer, respectively. The free cisplatin released was calculated by the colorimetric O-phenylene-diamine (OPDA) method by taking absorbance at 706 nm wavelength using Tecan Infinite Pro, Switzerland, multi-plate reader. The study was conducted in triplicates and plotted as percentage cumulative drug release vs. time.

2.2.6. Fabrication of tubular silk scaffold

The tubular scaffolds with one open end were prepared using the blended solution of BM and AA silk proteins in the optimized wt% ratio of 2:1, respectively. Manually in the bottom of a 96 well plate, small pieces of wooden toothpicks were pasted. BM and AA were blended in a separate vessel, and 300 µl of blend solution was added to each well. The plate was immediately frozen at -80° C and lyophilized. The lyophilized scaffolds were then separated from the well plate and incubated overnight in 70% ethanol at 4° C. Post ethanol crosslinking the wooden toothpicks were removed gently from each scaffold, and these one end open silk scaffolds were replaced into 70% ethanol until further use.

For the FESEM study, the lyophilized silk scaffolds were fixed over the stub through carbon tape and then images were captured using FESEM to determine the surface morphology and porosity.

2.2.7. *In vitro* 3D culture of stomach cancer cell (AGS) on tubular silk scaffold

The tubular silk scaffolds were washed 3-4 times with water to remove the ethanol content. For sterilization, scaffolds were autoclaved and conditioned overnight in complete media before seeding the cancer cells. Pre- calculated number of AGS stomach cancer cells were seeded onto the periphery of the scaffolds and allowed to adhere/infiltrate into the pores of the scaffold by gently adding the cell culture media. The culture media was replaced by fresh media every alternate day, and these conditions were followed for further functional studies. The histology was performed to confirm the cell infiltration in the porous scaffold. Cell-seeded scaffolds were cryosectioned at a thickness of 15 µm using Cryostat, Leica. The sections were collected on a glass slide for Haematoxylin and eosin (H & E) staining to determine the cell distribution inside the scaffolds. Live/dead assay was carried out to check the viability of the silk scaffolds cultured cells. The live/dead solution containing 1 µl of calcein-AM and 4 µl of ethidium homodimer-1 was prepared in 2 ml PBS.[180] The cultured scaffolds were carefully washed twice with sterile PBS, followed by the addition of 300 µl of live/dead solution. The scaffolds were then incubated at 37° C for 25 - 30 min. After the incubation period, the live/dead solution was discarded, and the images of the scaffold were captured using the fluorescence microscope (EVOS XL digital microscope).

2.2.8. Efficiency assessment of different anticancer therapeutic formulation (nanocomposite hydrogel) on 3D cultured AGS cells

Cell proliferation and cytotoxicity for AGS cells were analyzed by quantifying the reduction of Alamar blue dye at specified timepoints. 5000 stomach cancer cells per scaffold were seeded after conditioning of the scaffolds in cell culture media. Briefly, the cultured media was taken out, and Alamar dye (diluted 1:10 in complete DMEM medium) was added to the culture followed by incubation at 37 °C and 5% CO2 for 3 h. After the incubation period, the used dye was pipette out in a well plate, and absorbance was taken at 570 nm and 600 nm using a microplate reader for calculating the dye reduction by the live cells. % reduction of Alamar blue was calculated as per the manufacturer's instruction.

The study was continued for 21 days, initially, without any drug treatment, Alamar readings were taken for 8 days at specified time points. On the 9th day of the study, cell-seeded scaffolds were segregated into five groups. Group 1 was untreated

control. Group 2, 3, 4, and 5 were treated with Silk@cisplatin hydrogel, Silk@BMNP-cisplatin nanocomposite hydrogel, free cisplatin, and free BMNP-cisplatin, respectively. All the treatment groups received an equal 335 µg/ml cisplatin dose. The nanocomposite silk hydrogel was injected into the central cavity of the silk scaffold using a syringe. The scaffolds were then dispersed in media and incubated at the standard conditions. After two days of treatment, i.e., on 11th day (short term), Alamar reading was recorded, followed by reseeding of the same AGS cells to recapitulate the recurrence of tumor, which is the major aspect in cancer treatment and Alamar reading was further taken at 15th day. The study continued for 21 days (long term) to assess the effect of treatment given on 9th day. Later, a table was plotted for the percentage cells population increased or decreased from treatment day (9th day) using the following formula –

Percentage cell population change [(final Alamar unit – initial Alamar unit)/final Alamar unit] x 100

Where initial Alamar unit data was obtained from treatment day (day 9), and the final Alamar unit was derived from day 11, day 15, and day 21.

2.2.9. Gene expression analysis

The gene expression analysis of cell-seeded scaffolds was performed as previously done.[170] The cell-seeded scaffolds treated with Silk@cisplatin hydrogel and BMNP-Silk@cisplatin nanocomposite hydrogel were collected at 2nd day and 6th day of treatment along with untreated control. The scaffolds were disintegrated in Tri reagent (Sigma, USA) to isolate the ribonucleic acid (RNA). 1 µg RNA was reverse-transcribed (RT) into cDNA using a high capacity RT kit (Applied Biosystem, USA). The specific apoptosis gene markers were amplified using power SYBR green PCR master mix (Applied Biosystems, USA) in a real-time PCR machine (Applied Biosystems 7500, Thermo Fisher Scientific, USA). The nucleotide sequences of individual forward and reverse primers used are listed in **Table 2.1**. The relative gene expression was calculated with reference to endogenous housekeeping control beta-actin (β-actin) using -ΔCT method as follow –

$R = 2^{-(CT_{(GOI)} - CT_{(GAPDH)})}$, where R is relative gene expression, and GOI is the gene of interest.

Table 2.1 – List of primers used for gene expression analysis using real-time PCR.

No	Short name	Primers	Accession number
1	hBax (F)	CCTGTGCACCAAGGTGCCGGAACT	NM_001291431.1
	hBax (R)	CCACCCTGGTCTTGGATCCAGCCC	
2	hBcl 2 (F)	TTGTGGCCTTCTTTGAGTTCGGTG	NM_000657.2
	hBcl 2 (R)	GGTGCCGGTTCAGGTACTCAGTCA	
3	hBcl-xL (F)	GGAGTCAGTTTAGTGATGTGGAAGAG	NM_001322240.1
	hBcl-xL (R)	CATCTCCGATTCAGTCCCTTCT	
4	hCaspase-8 (F)	CTGCTGGGGATGGCCACTGTG	NM_001080125.1
	hCaspase-8 (R)	TCGCCTCGAGGACATCGCTCTC	

2.2.10. Statistical analysis

All the statistical analyses were done using OriginPro 8.5 software. The one-way Analysis of Variance (ANOVA) test was performed on triplicate raw data at a 0.001 significance level, and the significant difference is marked in the figures with the asterisk (*) wherever applicable.

2.3. Results

2.3.1. Preparation and characterization of BMNP

The spherical shape of lyophilized BMNP aqueous suspension was spotted in the FETEM and FESEM image, as shown in **Figure 2.1A & 2.1B** and **Figure 2.1C,** respectively. The size of dried BMNP was approximately 10 nm without any aggregation. However, the actual size of BMNP after water dispersion was determined by DLS as 63.13 ± 12.02 nm with a very low PDI of 0.270 ± 0.031, indicating its monodisperse distribution **(Figure 2.1D)**. Approximately five times, the difference in the size obtained by FETEM and DLS is noticeable. FETEM determines the actual size of nanoparticle in its dried state. Whereas, DLS measured the hydration sphere diameter and therefore showed a larger particle size than actual. BMNP is a protein nanoparticle that carries various hydrophilic functional groups on its surface. These surface groups help in the formation of hydrogen/non-covalent bonds with water, which ultimately leads to an increase in the hydrodynamic size of the nanoparticle. Additionally, protein nanoparticles also get swell up due to their hydration. The zeta potential of BMNP was recorded as -31.4 ± 0.351, which represents a very high negative charge present on its surface that plays a crucial role in its stability and monodispersity **(Figure 2.1E)**. Due to high negative zeta potential, BMNP repels each other and less likely to form an aggregation. The small-sized, highly stabile BMNP nanocarriers could, therefore, be employed as a preferred candidate for therapeutics delivery applications.

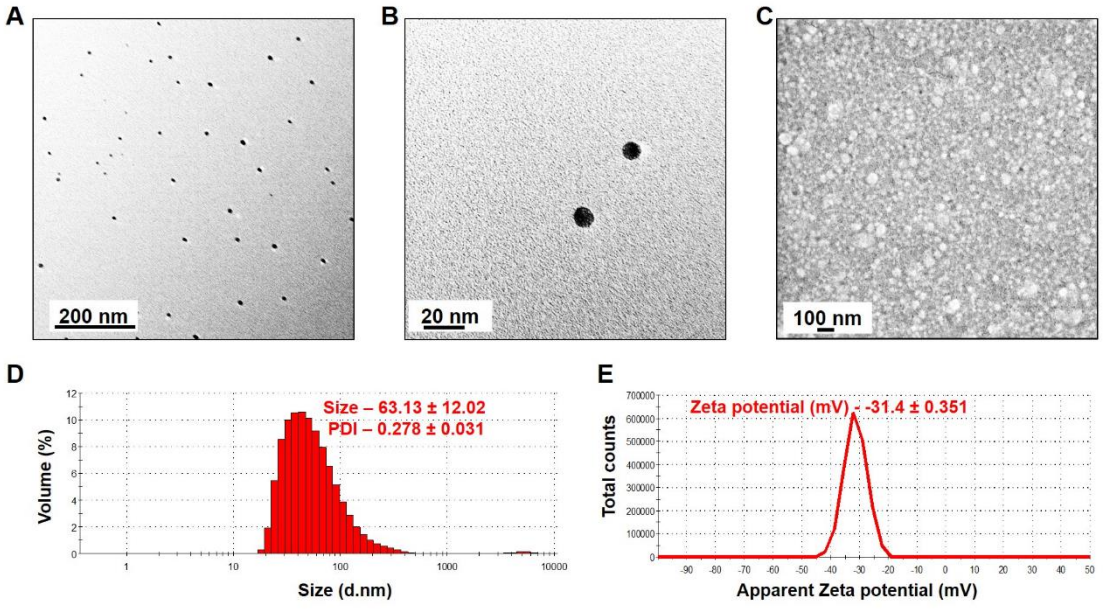

Figure 2.1. *B. mori nanoparticles (BMNP) prepared by acetone desolvation method and characterized by* ***(A)*** *FETEM at low magnification and* ***(B)*** *high magnification.* ***(C)*** *FESEM at 40K X magnification.* ***(D)*** *Size distribution and* ***(E)*** *zeta potential in water solvent system.*

2.3.2. Preparation and characterization of BMNP embedded silk hydrogel

BMNP was embedded into BM/AA blended silk hydrogel. The BM and AA SF were blended in a ratio of 1:1 (wt% : wt%) along with BMNP at different concentrations. BMNP incorporation into silk hydrogel drastically decreases the gelation time. A mixture of 1:1 wt%, BM and AA took 22.5 min to gel when blended alone without BMNP, which was due to low wt% (2%) of SF. Increasing the final wt% of silk hydrogel also increases the strength of the hydrogel and makes it stiffer, which is difficult to inject.

Interestingly, the addition of 25, 50, and 100 µg of BMNP reduced the gelation time in a concentration-dependent manner to 20.5, 18, and 13 min, respectively. BM and AA on blending reassemble to form secondary β-pleated sheet structures due to the differences in their hydrophobicity and structural composition, which results in the formation of a hydrogel. Both BMNP and hydrogel were prepared from the SF solution having similar amino acid compositions. Therefore, the β-pleated sheet of BMNP might provoke further reassembly within the BM/AA blend, which quickly triggers the gelation and reduce the gelation time **(Figure 2.2A)**. The amplitude sweep illustrated more or less similar yield points for all the gel, which attributed no additive effect of BMNP on the strength of the nanocomposite hydrogel **(Figure 2.2B)**. Keeping shear strain constant at 10 % frequency sweep was performed for all the gels. The integrity of all the hydrogels was consistent until the frequency of 70 rad/s; however, a further increase in the rate disintegrated the hydrogels, which is attributed by a sudden drop in storage modulus shown in **Figure 2.2C**. Loss factor less than one for all gels described its viscoelastic nature. However, the addition of BMNP enhances the viscous property of the gel **(Figure 2.2D)**. Viscosity plot showed the shear thinning of all the gels, which is described by a decrease in the viscosity with the increase in shear strain **(Figure 2.2E)**. Due to the shear-thinning property, the silk hydrogel could be easily injected at the site of disease, where it may act as a depot for the sustained release of the drug. Thixotropy of all the gels also remained unaltered post-BMNP addition. For the thixotropy, the shear strain was first set under the LVE region, which then changed to the above LVE region. This cycle was

repeated three times, and hydrogel disintegration and recovery were attributed by the high and low storage modulus, respectively **(Figure 2.2F)**.

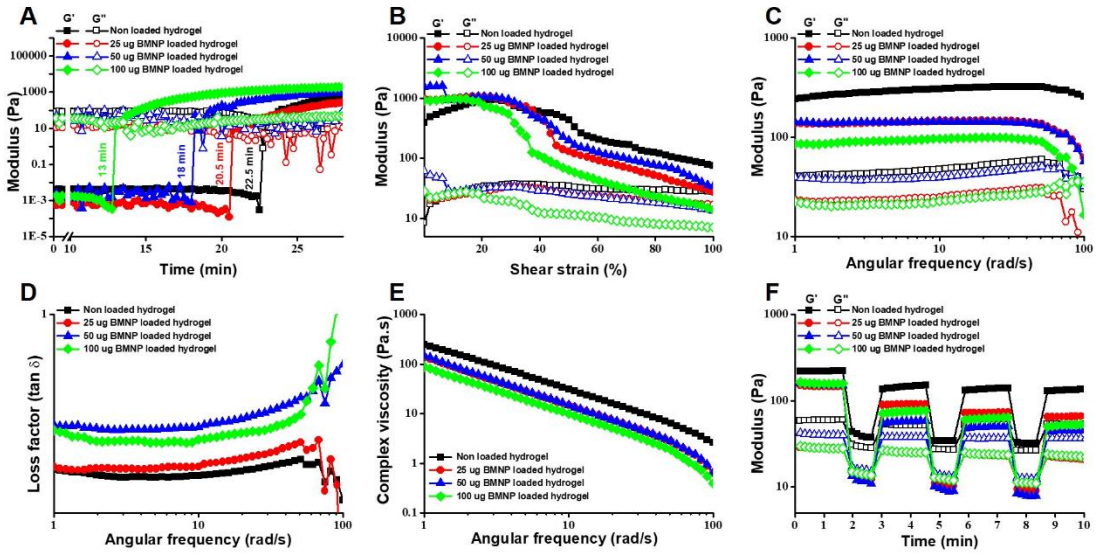

Figure 2.2. *Rheological characterization of 25, 50, and 100 µg BMNP embedded in 2 wt% silk hydrogel (1:1; BM:AA).* ***(A)*** *Gelation time,* ***(B)*** *amplitude sweep* ***(C)*** *frequency sweep,* ***(D)*** *loss factor,* ***(E)*** *viscosity, and* ***(F)*** *thixotropy.*

2.3.3. Determination of cisplatin loading capacity of BMNP

The loading of cisplatin to BMNP was determined by the colorimetric OPDA method. Various concentrations of cisplatin from 0 to 100 µg/ml were subjected to the standard protocol and presented in **Figure 2.3A** the absorbance scan plot. A characteristic absorption maximum at 706 nm wavelength was chosen to plot a straight line standard plot showing as an inset in **Figure 2.3A**.

To 1 mg/ml BMNP 3 mg/ml cisplatin was mixed initially in water and buffers of pH 4, 7.4, and 9.1. All the tubes were incubated for 48 h with continuous mixing on rotospin and then centrifuged to calculate the loading efficiency. We observed approximately 20, 10, 18, and 40% loading of cisplatin to water, pH 4, 7.4, and 9.1 buffer, respectively **(Figure 2.3B)**. Therefore, due to the significantly high cisplatin loading efficiency, pH 9.1 buffer was selected for further experiments.

The FTIR spectra of pure cisplatin powder, lyophilized BMNP, and BMNP-cisplatin powder showed in **Figure 2.3C**. Cisplatin showed strong absorption bands at 1300 cm^{-1} and 805 cm^{-1}, which represented symmetric amine bending and the stretching vibration peaks of −Cl, respectively.[181] However, both BMNP and cisplatin showed

strong absorption bands at 1500/1535 $cm^{-1,}$ and 1632 cm^{-1} indicated the asymmetric amine bending. BMNP showed absorption bands at 1358 cm^{-1}, which were characteristic absorption peaks of carboxyl groups in silk fibroin. The FTIR spectra of BMNP-cisplatin illustrated the intensity of the stretching vibration peaks of −Cl in cisplatin at 805 cm^{-1} decreased, indicating that the coordinate bond between −Pt and −Cl had fractured in the process of combining the cisplatin and BMNP. Besides, the stretching vibration of the carboxyl groups of BMNP at 1358 cm^{-1} disappeared, demonstrating that the carboxyl groups were binding Pt from cisplatin. The loading process of cisplatin onto BMNP was achieved via a ligand exchange reaction of Pt from the chloride to the carboxyl groups in the BMNP. In corroboration with our observation Qu et al. has also reported the coordination linkage between the silk nanoparticles and cisplatin previously.[182]

The BMNP-cisplatin conjugate was blended with BM and AA SF solution to form Silk@BMNP-cisplatin nanocomposite hydrogel, with injectable properties, as shown in **Figure 2.3D.** The EDX analysis also confirmed the presence of Pt in the nanocomposite silk hydrogel **(Figure 2.3E)**. The other prominent elemental peaks of carbon, oxygen, nitrogen, chlorine, sodium, potassium, and sulfur in EDX analysis is due to the salt/carbon tape used in the processing of the sample.

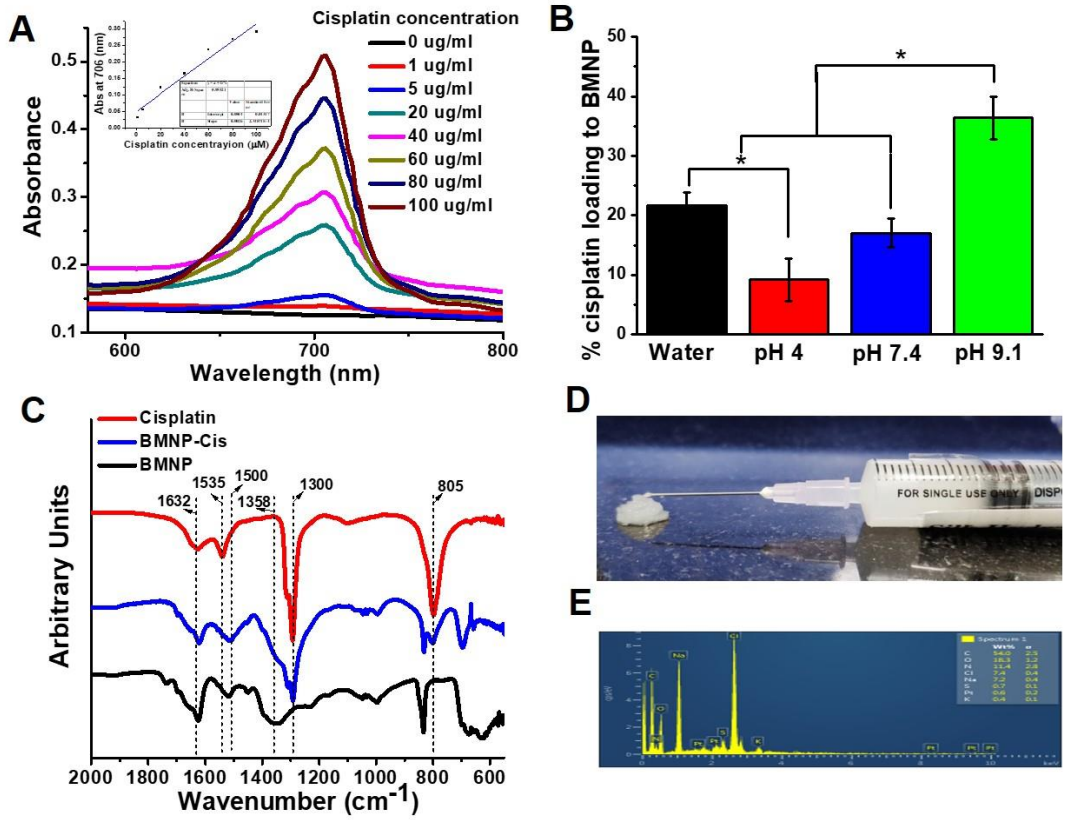

Figure 2.3. ***(A)*** *Absorbance scan plot of cisplatin using O-phenylenediamine diamine (OPDA) colorimetric method. The inset is showing a cisplatin standard plot at 706 nm wavelength.* ***(B)*** *% cisplatin loading to BMNP in water and buffers of pH 4, 7.4, and 91.* ***(C)*** *FTIR spectra of cisplatin, BMNP-cisplatin, and BMNP lyophilized powder.* ***(D)*** *Representative injectable Silk@BMNP-cisplatin nanocomposite hydrogel and* ***(E)*** *its EDX elemental analysis.* *p < 0.001.

2.3.4. *In vitro* drug release studies from Silk@cisplatin and Silk@BMNP-cisplatin nanocomposite hydrogel

The Silk@cisplatin hydrogel **(Figure 2.4A)** and Silk@BMNP-cisplatin nanocomposite hydrogel **(Figure 2.4B)** were incubated in different pH buffer (4, 7.4, and 9.1) system for the comparison of drug release efficiency. The cisplatin release from both the silk hydrogel was pH-dependent. The release at pH 7.4 and 9.1 was approximately 30 to 45% in 21 days for both the hydrogels, which attributes the electrostatically linked or surface adsorbed cisplatin release. However, at low pH buffer (pH 4) burst release of cisplatin from Silk@cisplatin hydrogel was recorded compared to sustained release from Silk@BMNP-cisplatin nanocomposite silk hydrogel. The initial burst release observed in **Figure 2.4A** at acidic pH 4 showed approximately 60% of the drug release within one day, followed by no further release until seven days. However, sustained and slow release was recorded in **Figure 2.4B** at acidic pH 4, with a total of 80% drug in 21 days. Due to BMNP, the nanocomposite hydrogel held the cisplatin for a longer duration and released it slowly on hydrolysis at lower pH.

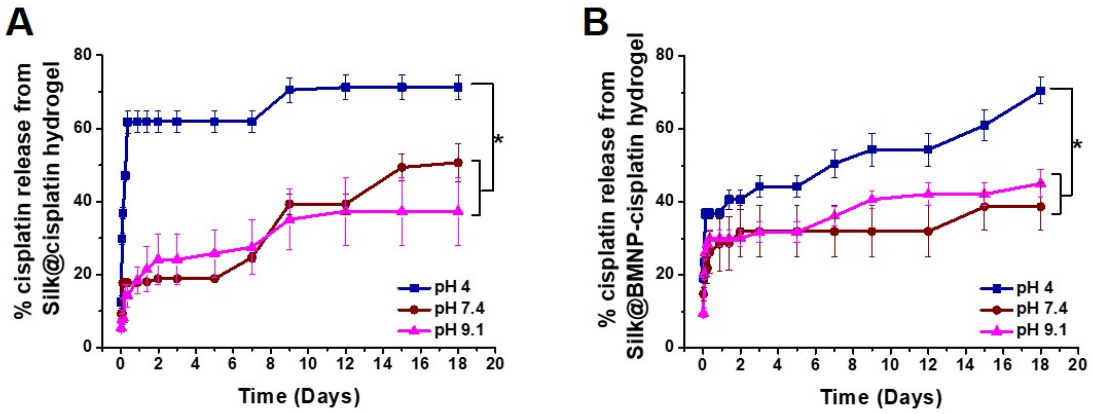

Figure 2.4. *In vitro pH-dependent drug release study by incubating* ***(A)*** *Silk@cisplatin hydrogel and* ***(B)*** *Silk@BMNP-cisplatin nanocomposite hydrogel, at different pH (4, 7.4 and 9.1) buffer. *p < 0.001.*

2.3.5. *In vitro* 3D culture of stomach cancer AGS cell on the periphery of porous silk scaffold

The key obstacle in the screening of anticancer drugs is a complex tumor microenvironment. Here, the silk 3D scaffold was designed to support the cell growth in the periphery to provide a tumor environment, as shown in **Figure 2.5A**, and space in the center to hold the hydrogel for *in vitro* drug delivery/screening applications. The diameter of the tubular silk scaffold was 6 mm, where the ~2x3 mm central cavity was surrounded by a ~4x6 mm periphery, as depicted in **Figure 2.5B**. FESEM analysis revealed the porous and interconnected interior structure of the scaffold **(Figure 2.5C)**. The average pore size is approximately 200 to 400 µm, which is sufficient for cells to infiltrate and propagate in a 3D environment. The histological H&E stained images in **Figure 2.5D** confirmed the presence of AGS cells all around the pores of silk scaffolds. The low magnification image in **(Figure 2.5Di)** indicated the cancer cell even distribution; however, high magnification **(Figure 2.5Dii)** image revealed the formation of several spheroids or tumoroids like structures. The pores of the scaffold provided space for the cancer cells to infiltrate and form aggregates, which later took the shape of the spheroid. Such an environment, which contain several tumoroid like structure, makes an ideal condition for screening the efficiency of anticancer drug.

Live/ dead assay was carried out to examine the viability of stomach cancer cells seeded over silk scaffolds. The scaffolds were treated with a mixture of 4 µM calcein AM and 2 µM ethidium homodimer-1 dye. Live cells emit green fluorescence (λex/em ~ 495/515 nm) due to the uptake of calcein-AM only by metabolically active cells. In contrast, dead cells emit red fluorescence (λex/em ~ 495/635 nm) due to the internalization and binding of ethidium homodimer-1 to nucleic acids only by the damaged/dead cells.[180] A fluorescent microscope captured the significantly high numbers of green fluorescent live granular spheroid like structures in **Figure 2.5Ei** and **Figure 2.5Eiv**, as compared to the negligible red fluorescent dead cells in **Figure 2.5Eii** and **Figure 2.5Ev,** indicating the biocompatibility and cell growth supporting capability of the silk scaffold. The red fluorescence observed in **Figure 2.5Eii** and **Figure 2.5Ev** could be due to the silk autofluorescence, as shown in **Figure A2.1**. The merged image **Figure 2.5Eiii** and **Figure 2.5Evi** further confirmed the silk autofluorescence and alive spheroids of cancer cells.

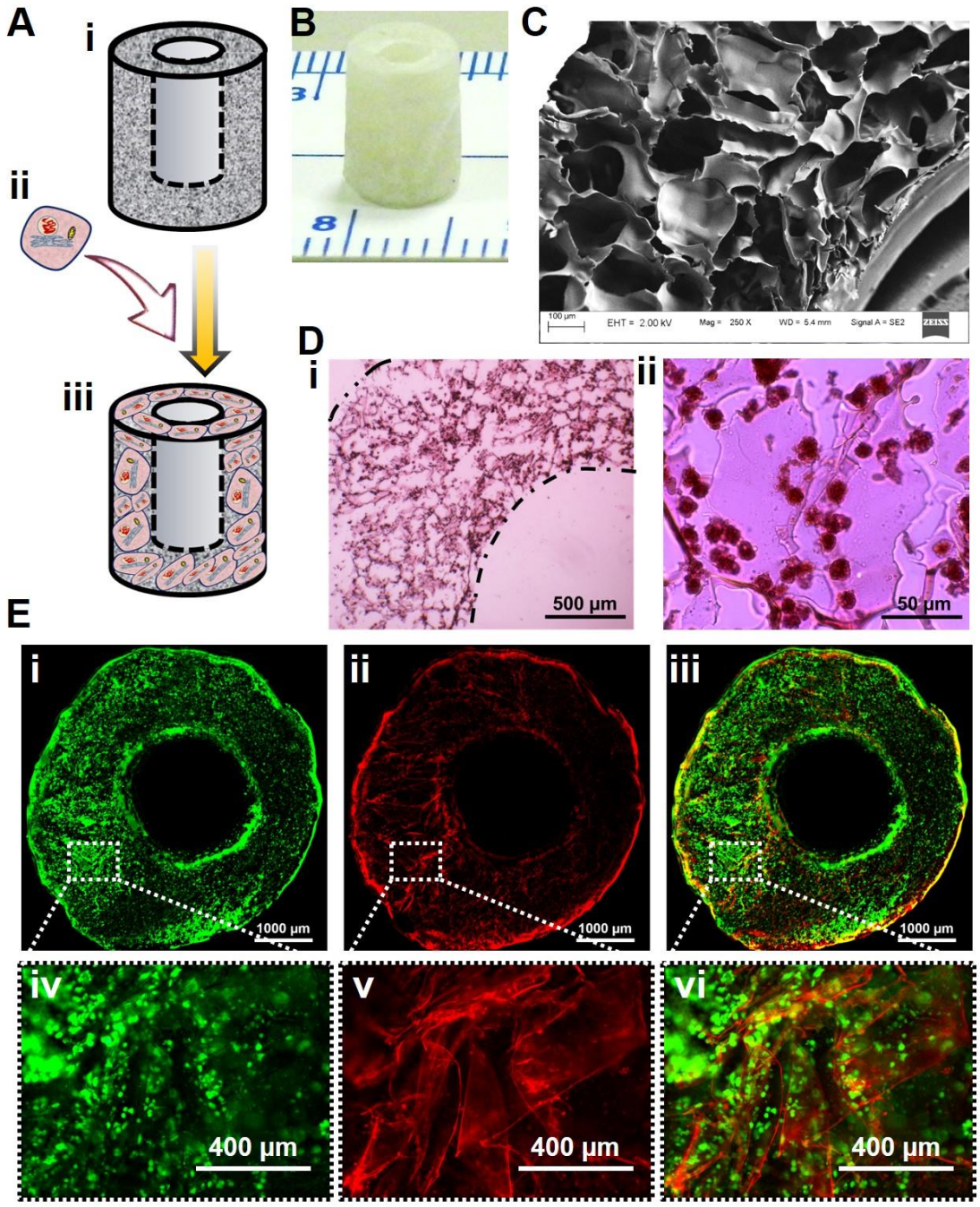

Figure 2.5. *A pictorial representation* ***(A)*** *and working model* ***(B)*** *of porous tubular silk scaffold with one end open.* ***(C)*** *The FESEM image of the silk scaffold showing its porosity.* ***(D)*** *H&E stained transverse section of stomach cancer AGS cell-seeded scaffold at (i) 4X and (ii) 40X magnification.* ***(E)*** *Live (left green), dead (middle red), and merged (right) images of the cell-seeded scaffold at 4X (top panel) and 40X (Bottom panel) magnification by calcein-AM and ethidium homodimer dye. The 4X images (top panel) shown here are the composite of several pictures captured at the same excitation exposure using a fluorescence microscope to cover the entire scaffold.*

2.3.6. Assessment of nanocomposite hydrogel on 3D cultured AGS cancer cells

Stomach cancer AGS cells were seeded onto tubular silk scaffold and allowed to grow to assess the efficacy/functionality of the cisplatin molecule in the long term, that is releasing from the nanocomposite silk hydrogels. The experimental scheme is depicted in **Figure 2.6A**. Three Alamar readings, on days 2, 4, and 9 were taken before the treatment to assure the equal cell seeding/growth rate in all the scaffolds. On day 9, the scaffolds were divided into five groups with n=3. Group 1 was untreated control; group 2 was treated with Silk@cisplatin hydrogel; group 3 with Silk@BMNP-cisplatin nanocomposite hydrogel; group 4 with an equivalent amount of free cisplatin solution; and group 5 with BMNP-cisplatin suspension containing equivalent cisplatin dose.

Initially, until day 9, a similar growth rate was recorded from all the scaffolds. However, a sudden drop in the Alamar units values on day 11, represented the cell growth inhibition of all the four treated groups in contrast to the untreated group **(Figure 2.6B)**. To further continue the experiment, the scaffolds of treatment groups were reseeded with AGS cells, and Alamar readings were recorded until day 21. The Alamar units of all the treatment groups were increased except group 3, which was treated with Silk@BMNP-cisplatin nanocomposite hydrogel. The positive/negative percentage cell population was calculated from the Alamar unit of treatment day and presented in **Table 2.2**. On day 11, the untreated group showed positive 13.8 ± 3.7 % cell proliferation compared to all the treated groups that showed a 30 to 50 % cell growth inhibition. The AGS cell reseeding caused the cells to grow further on the scaffold, and all the groups showed consistent positive 20 to 35 % cell proliferation from day 15 to day 21 in contrast to group 3 treated scaffold that showed steady 4 to 5 % cell growth inhibition. The BMNP-cisplatin loaded silk nanocomposite hydrogel did not allow the cells to grow further due to sustained release and cytotoxic functionality of cisplatin. However, post reseeding the increase in the cell population of group 2 treated scaffold at day 15 indicated that cisplatin might be burst released or stopped releasing from the hydrogel. Later, until 21 days saturation phase was observed in all the scaffolds, which might be due to the unavailability of space in the scaffold. However, the long term (from day 9 to day 21) effect of treatment was observed in BMNP-cisplatin nanocomposite silk hydrogel, which indicated that this way, stomach cancer cell growth could be inhibited for effective therapy.

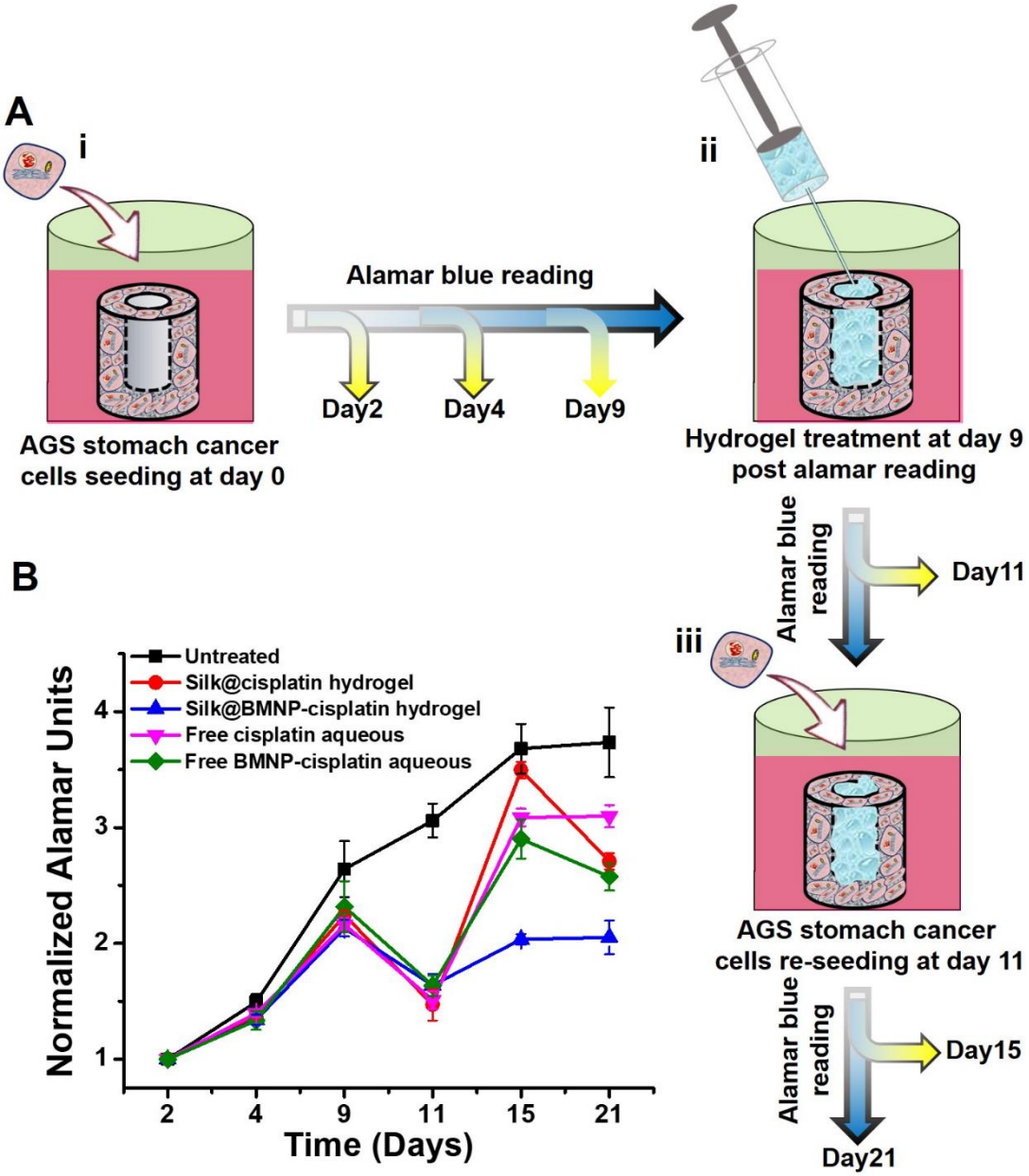

Figure 2.6. (A) *A pictorial representation showing an experimental scheme followed for functionality assessment of injectable silk hydrogel over AGS cells cultured on 3D silk scaffold. The experiment started with (i) cell seeding followed by (ii) treatment with injectable hydrogel in the center of the tubular scaffold and (iii) reseeding of cells. Cell proliferation was assessed at indicated time points using Alamar blue reagent.* ***(B)*** *the calculated normalized Alamar units were plotted against time.*

Table 2.2. Percentage determination of short term (day 11) and long term (day21) effect of respective treatment groups from the day of treatment (day 9). (+) and (-) indicates the percentage proliferation and inhibition of cell viability with respect to treatment day.

	Untreated	**Silk@cisplatin hydrogel**	**Silk@BMNP-cisplatin hydrogel**	**Free cisplatin**	**Free BMNP-cisplatin**
	Average (%) ± SD	Average (%) ± SD	Average (%) ± SD	Average (%) ± SD	Average (%) ± SD
Short term therapy followed by cell reseeding (day 11)	+13.8 ± 3.7	-53.0 ± 13.2	-30.1 ± 3.8	-43.3 ± 7.4	-41.4 ± 9.3
Mimicking cancer recurrence (day 15)	+27.7 ± 11.1	+35.9 ± 1.1	-4.8 ± 5.2	+29.9 ± 0.6	+20.1 ± 5.1
Long term therapy (day 21)	+24.9 ± 4.8	+17.2 ± 3.3	-4.3 ± 9.1	+30.1 ± 0.5	+10.0 ± 7.0

2.3.7. Gene expression analysis

The AGS cell death in response to cisplatin releasing from the hydrogel was assessed by gene expression analysis. Bax, Bcl-2, Bcl-xl, and Casp-8 gene markers expression was determined using their respective primers; the sequences of those were obtained from previously published articles.[55] The untreated control sample showed a basal level of expression for all the genes tested with no significant change between the samples collected on the 2nd day and 6th day of the experiment, which indicates the healthy growth of cancer cells cultured on untreated scaffold until six days **(Figure 2.7)**. Bax is a pro-apoptotic marker which significantly overexpressed in both Silk@cisplatin, and Silk@BMNP-cisplatin hydrogels treated scaffolds suggesting a probable apoptotic induced pathway for cell death. However, the Bax expression was markedly higher in Silk@BMNP-cisplatin nanocomposite hydrogel treated samples compared to both Silk@cisplatin hydrogel treated and untreated samples indicating its higher cytotoxicity **(Figure 2.7A)**. Bcl-2 and Bcl-xl are anti-apoptotic gene marker which showed an enhanced level of expression in both the treated groups compared to untreated Which may be due to some initial resistance induced by cancer cells against the cisplatin. On treatment with BMNP- Silk@cisplatin hydrogels, no change was recorded in the

expression of Bcl-2; however, with Silk@cisplatin hydrogel treatment, Bcl-2 expression was increased further at 6th day compared to 2nd day. This may be due to the absence or insufficient cisplatin available to Silk@cisplatin hydrogel treated scaffolds until 6th day to cause the cell cytotoxicity **(Figure 2.7B)**. The expression level of Bcl-xl showed a significant reduction at 6th day compared to 2nd day in both the treatment suggesting the progression of apoptosis **(Figure 2.7C)**. Caspase-8 is a marker protein of apoptosis pathway which expression significantly enhanced in Silk@BMNP-cisplatin hydrogels treated scaffolds from 2nd day to 6th day **(Figure 2.7D)**. In summary, the gene expression analysis suggesting the long term sustained functionality of cisplatin releasing from Silk@BMNP-cisplatin nanocomposite hydrogel for the induction of the apoptosis pathway.

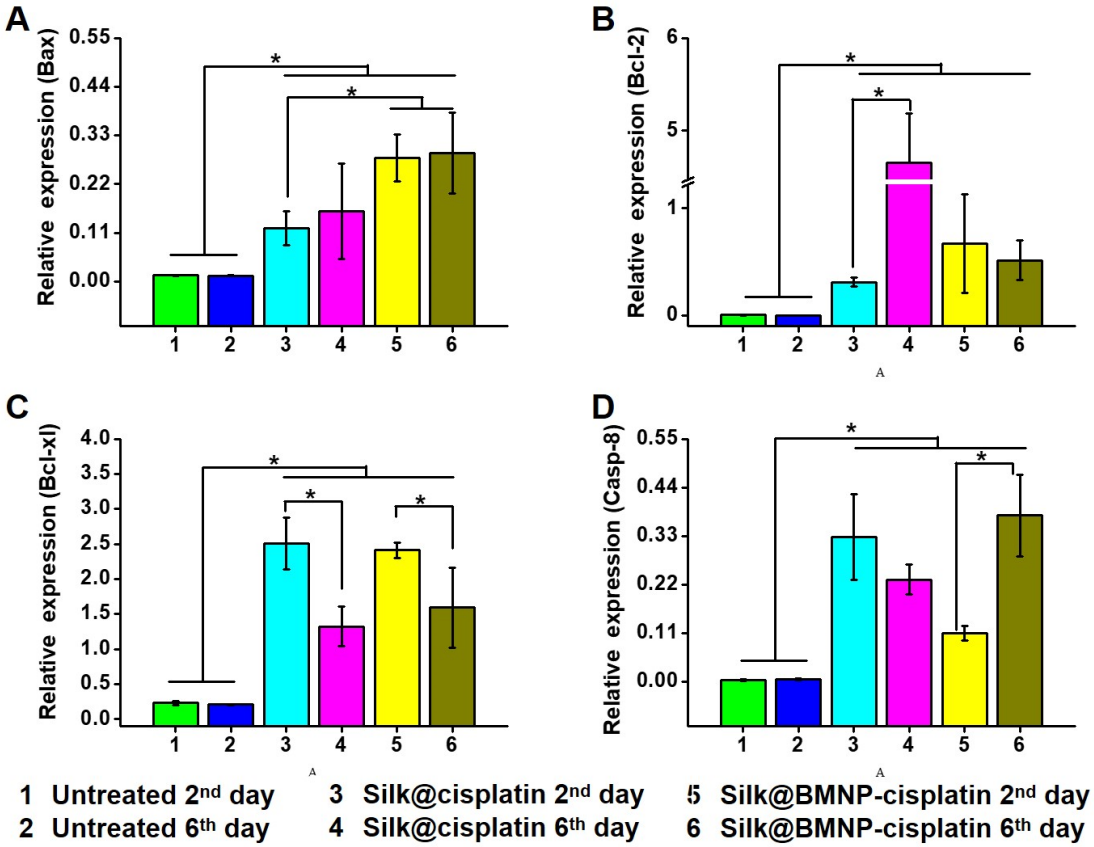

Figure 2.7. *Relative gene expression of* ***(A)*** *Bax,* ***(B)*** *Bcl-2,* ***(C)*** *Bcl-xl, and* ***(D)*** *Caspase-8 through real-time PCR for the samples collected on 2nd day and 6th day of Silk@cisplatin hydrogel and Silk@BMNP-cisplatin nanocomposite hydrogel treatment and compared with untreated samples.* *p < 0.001.

2.4. Discussion

Nanocomposite biomaterials are preferred over their counterpart due to synergistic enhancement in the properties of pure polymers on the addition of metal/nonmetal nanoparticles.[165] The nanocomposite hydrogels have extensively shown their applications in tissue engineering, biosensors development, electronics, water treatment, and drug delivery. Cisplatin is a gold standard FDA approved anticancer drug prescribed to the patient as the first line of treatment against epithelial malignancies, including stomach cancer. The cisplatin mediates apoptosis pathways in cancer cells by damaging DNA and inducing oxidative stress for tumor inhibition.[183] However, systemic delivery also causes apoptosis in healthy renal tubular cells, auditory sensory cells, and optic nerve cells, which arise nephrotoxicity, ototoxicity, and optic neuropathy, like side effects in patients. Additionally, tumors also develop resistance against cisplatin due to insufficient drug supply, reduction in its accumulation at the tumor site, quick repair of the cisplatin-induced anomaly, and upregulation of anti-apoptosis factors.[183, 184] Recently, many efforts have been made towards target-specific delivery of cisplatin to reduce its side effects.[185, 186] In the present work, we used silk as a base material to prepare nanoparticles, hydrogels, and porous scaffolds. All these components were characterized extensively. The nanocomposite silk hydrogel exhibit sustained cisplatin release and could be a potential candidate for localized drug delivery. The scaffold was specifically designed to support the growth of cancer cells spheroids in 3D for the long-term efficacy/functionality assessment of injectable hydrogel systems. The biological assays were conducted to investigate the cell growth/death on the scaffolds with/without the hydrogel treatment.

Our prepared BMNP showed a highly regular spherical shape and monodisperse distribution in the aqueous phase. The SF nanoparticles have been extensively studied all around the globe in terms of their preparation and applications in delivering various hydrophilic/hydrophobic/charged anticancer drugs[160, 163, 166, 182] SF protein consists of different hydrophilic/hydrophobic and charged amino acids that, by hydrophobic/electrostatic interactions, bind to different types of cationic/anionic anticancer drugs and release them on various endogenous cues such as pH, protease degradation, water hydrolysis etc.[165, 166] The binding of cisplatin with BMNP was due to the combined effects of electrostatic interactions and coordination linkages.[182] The high loading of cisplatin to BMNP at pH 9.1 attributes the electrostatic interaction

between cisplatin and negatively charged BMNP. However, FTIR data also suggest the formation of coordination linkage between the COOH group of BMNP and Pt of cisplatin.

The BMNP-cisplatin embedded silk hydrogel released the cisplatin sustainably as compared to the burst release by cisplatin alone embedded silk hydrogel at low pH, which is described by a pH-responsive behavior of SF polymer.[55, 161] The low pH induces the reassembly of silk hydrogel, which allows the penetration of water into its matrix for water hydrolysis dependent cisplatin release. The Silk@cisplatin hydrogel contains free cisplatin, which released immediately due to water hydrolysis; however, Silk@BMNP-cisplatin nanocomposite hydrogel contains the BMNP as a barrier for cisplatin release and release it in three phases. In the first phase, the burst release of free cisplatin occurred. In the second phase, electrostatically bound cisplatin was released, and finally, the coordination linked cisplatin was released at the end. Contribution of all the interactions resulted in sustained cisplatin release until 21 days from Silk@BMNP-cisplatin nanocomposite hydrogel.

Various methods for the fabrication of SF hydrogel has been reported previously.[168] The 3 wt% SF hydrogel is considered as the standard concentration for drug delivery applications as increasing the concentration of SF protein also increases the strength of the hydrogel, which might be difficult to inject. Also, the small pore size and low rate of degradation of high wt% silk hydrogel affect the release rate of the drug. In the present work, we have blended two different varieties of SF protein in equal wt% to form the 2 wt% hydrogel without using any crosslinker/toxic chemical. The difference in the amino acid composition induces the gelation in the blend as described in details previously.[55, 167] However, as confirmed by rheology data, the 1:1 wt% (BM:AA) silk blend took ~23 min to gel at 37 ^{O}C, which is a long incubation time. The addition of BMNP in this blend drastically reduced the gelation time in a concentration-dependent manner without affecting its strength/viscosity/shear thinning property. The rheology data further suggested the silk hydrogel is viscoelastic and has shear-thinning properties, which explained its injectability. Hydrogels usually experience high pressure while extruded out through a needle. Such high pressure may lead to a loss in the hydrogel network integrity. However, our thixotropy data indicating that silk hydrogel regained its structural integrity as soon as the high pressure was released. Therefore, the silk

hydrogel once injected could take up the vessels shape and release its content for the purpose.

Screening drugs in a 2D culture dishes does not warrant the close interpretation of drug toxicity *in vivo* due to the complex tumor microenvironment. 3D tumor models have emerged as the cheapest alternative of experimental animal disease models.[176, 187] The growth and infiltration of AGS stomach cancer cells on our designed porous silk scaffold **(Figure 2.5)** showed the evidence of its biocompatibility. Due to the large pores of the scaffold, AGS cells grown in the form of spheroids, which dictate it as an excellent model for anticancer drug screening/testing. Researchers have demonstrated various methods where hanging drop, microwell, and suspension are usual to produce spheroids for drug screening applications.[175, 188] However, the spheroid formation by these methods are mostly governed by passive aggregation of multiple cells and, therefore, tends to attach loosely. In the present work, the formation of masses of spheroids in the pores of the silk scaffold could be a result of single-cell multiplication, which should have more close similarities to *in vivo* tumoroids concerning intercellular crosstalk and cell to extracellular matrix interaction. Wang et al. have also shown comparable prostate cancer spheroid formation in the chitosan-alginate scaffold for targeted gene delivery.[177]

The application of injectable hydrogel system for the treatment of chronic diseases such as arthritis, cancer, skin wounds, etc., have been recognized all around the globe.[3, 156, 164, 189] However, the current *in vitro* cell culture models lacks the ability to accommodate both the hydrogel and cells together.[55, 158, 178] As shown in **Figure 2.6** the silk scaffold has encompassed both injectable nanocomposite hydrogel in the central cavity and stomach cancer spheroids around its periphery space. Also, cisplatin activity was preserved by the nanocomposite hydrogel, as we recorded its persistent action in 12 days (from day 9 to day 21) treatment period. Further, in our current approach, we tried to mimic cancer recurrence. The development of *in vivo* cancer recurrence model is difficult and painful for the animals, wherein a layer of the tumor surrounding the skin is left voluntarily to construct the postoperative cancer recurrence model. Recently many reports have shown the ability of anticancer drug-loaded injectable hydrogel for the prevention of cancer recurrence in such small animals models.[190-193] Seib et el has used a transwell plate wherein the authors have reseeded the cancer cells in 2D to mimic the cancer relapse.[194] However, no 3D *in vitro* model

is available yet to study the same. In this regard, we reseeded the AGS stomach cancer cells post-treatment, when the growth of pre-seeded cancer cells was inhibited. The toxic effects of Silk@BMNP-cisplatin nanocomposite hydrogel further inhibited the recurring growth of reseeded AGS cells, in contrast to other treatment groups where AGS cells proliferated well. The qPCR data in **Figure 2.7** further confirmed the apoptosis induced toxicity, referring to the regular activity of the released cisplatin drug.

2.5. Significant findings

The significant findings from this chapter are as follow –

1. We have successfully fabricated a porous silk scaffold that accommodated both tumoroids and hydrogels together for the bioactive molecule functional study.

2. The silk fibroin nanoparticles of 10 to 50 nm diameter were successfully prepared and conjugated with anticancer drug cisplatin.

3. The sustained cisplatin release through Silk@BMNP-cisplatin nanocomposite hydrogel makes it superior to the burst releasing Silk@cisplatin hydrogel.

4. The nanocomposite silk hydrogel has also enhanced the shelf life of the loaded cisplatin as specified by 11 days *in vitro* experiment. The nanocomposite hydrogel had shown the growth inhibition of stomach cancer spheroids due to long term toxicity and functionality of released cisplatin drugs.

5. The nanocomposite hydrogel effectively prevented the growth of reseeded cancer cells and revealed its ability to inhibit the recurrence.

6. The preliminary data generated by such a model may further extend in determining the effective number and frequency of hydrogel doses for future animal studies.

Hence, we propose that the system used in the current study has the potential to fill up the current gap in evaluating the soft injectable hydrogels *in vitro* for sustained drug delivery applications.

Chapter 3

Single-Walled Carbon Nanotube (SWCNT) Impregnated Injectable Silk Hydrogel for Folic Acid Receptor Overexpressing Oral Cancer Cell-Targeted Doxorubicin Delivery

This chapter explores the development of extenally addressable nanocomposite hydrogel and extensively assessed in vitro as a potential candidate for targeted and localized cancer therapy.

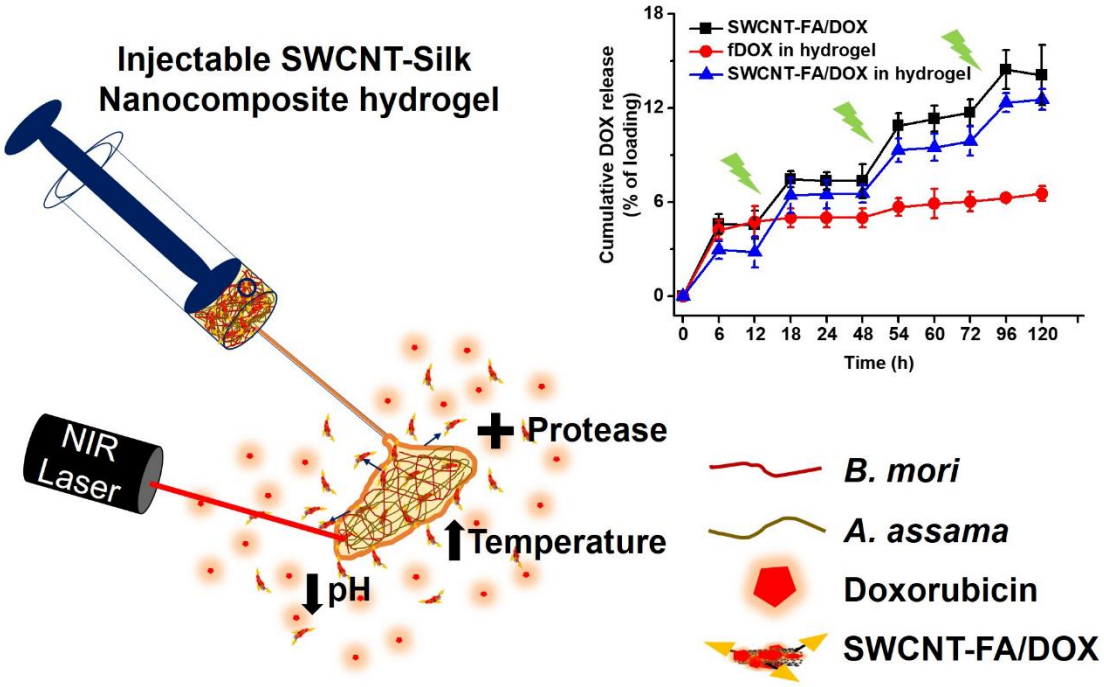

The work embodied in this chapter is published in a peer-reviewed journal as follow:
Ankit Gangrade and Biman B. Mandal. "Injectable Carbon Nanotube Impregnated Silk Based Multifunctional Hydrogel for Localized Targeted and On-Demand Anticancer Drug Delivery." ***ACS Biomaterials Science & Engineering*** 5, no. 5 (2019): 2365-2381.

ABSTRACT

The major limitation of traditional method of anticancer drug delivery includes its systemic distribution and frequent administration intravenously. To address these issues, in our present approach, we have fabricated a nano hybrid silk hydrogel system for localized, targeted and on demand delivery of anticancer drugs. The hybrid system contains a blend of two varieties of silk protein and doxorubicin (DOX) loaded folic acid functionalized single-walled carbon nanotubes (SWCNT-FA/DOX). Owing to the single-walled carbon nanotubes (SWCNT) incorporation, the mechanical strength of hybrid silk hydrogel composite enhanced significantly. A slow and sustained DOX release was recorded over a 14-day study. The amount of DOX released was determined by concentration of SWCNT-FA/DOX payload, rate of silk degradation, pH of the released medium and incubation temperature. The intermittent exposure of near-infrared light to the hybrid gel system stimulated on demand DOX release. The *in vitro* studies demonstrated the active targeting of SWCNT-FA/DOX to folic acid receptor-positive (FR^{+ve}) cancer cells. The silk hydrogel being viscoelastic in nature is easily injectable to the targeted site. Hence, the developed silk hybrid gel system may allow its near or intra-tumoral implantation, where it may act as a depot for anticancer drug-loaded nanoparticles. The sustained, targeted and external stimuli dependent DOX release at localized tumour site is expected to reduce its systemic side effects and showed an efficient way to treat the cancer.

3.1. Introduction

The incidence and mortality rate associated to cancer is increasing worldwide [195]. Chemotherapy is a major and most fundamental therapeutic approach for cancer treatment. Researcher have developed several potent anticancer drugs until date and continued to develop new ones. However, hydrophobic nature of drug molecules, inability to discriminate between normal and cancer cells, fluctuating plasma level, development of drug resistance by cancer cells and loss of activity in blood circulation limits the use of these drugs in cancer treatment. Alternatively, in recent times, efforts have been made towards the development of new and efficient strategy to deliver these potent drug molecules straight to the tumour to reduce the cytotoxic effects [104, 194, 196, 197]. In such approaches, nanotechnology, which employs the non-reactive inert nano-sized carrier to ferry and deliver anticancer drugs at target site exhibited promising results [198]. However, its multiple dosages are required due to a systemic distribution which requires frequent patient visits. Hence, the idea of using injectable hydrogel is introduced to further improve the cancer therapy [199]. The hydrogel is a 3D network of polymer consisting of more than 95% of water and may be used as a reservoir for the drug at the tumour site. The sustained release of drug from hydrogel helps in retaining these active molecules at the tumour site thus enhancing its effeciency in cancer therapy[199].

Silk fibroin (SF) is a natural protein polymer biomaterial having innate properties like biocompatibility, high tensile strength, flexibility, water vapour permeability, tissue compatibility, high oxygen permeability, amenability to multiple processing formats and tunable biodegradation rates [200]. It is pertinent to note that silk obtained from *Bombyx mori* (BM), a member of the Bombycidae (domesticated, mulberry silk) family has been extensively studied for biomedical applications. However, silk extracted from other sources including members of the family Saturniidae (wild, non-mulberry silk) e.g., *Antheraea mylitta*, *Antheraea pernyi*, *Antheraea assama* (AA), and *Philosamia ricini* have come into focus only recently [201, 202]. Studies have also revealed the comparative moisture regain ability and biocompatibility in terms of cell attachment, proliferation, migration and differentiation within different varieties of silk [200]. In this context, various mulberry and non-mulberry based silk, due to their unique bio-physico-chemical attributes hold immense potential for fabrication of injectable hydrogels [197, 203, 204].

SF forms hydrogel post application of various stresses such as change in pH, vortexing, sonication, electrical current stimulation etc.[104, 197, 205-208]. By virtue of these external stimuli, the major α-helix structure of aqueous silk solution reassembles into the β-sheet structure to form hydrogel network [206]. These properties make it suitable for drug delivery and tissue engineering applications. The release kinetics of the drug from the hydrogel is dependent on the payload amount, crystallinity and degree of crosslinking. These parameters are tunable by varying the concentration of SF and degree of stimulus [197, 204]. The controlled and sustained release of anticancer drugs [104, 194], monoclonal antibody [207], anti-inflammatory drugs [103, 209] and growth factors [208] from silk hydrogel have also been demonstrated.

Targeted drug delivery (TDD) for cancer therapeutics is an approach which utilizes the principle of identification of cancer cells based on their cell-specific marker overexpression such as receptors and their abnormal behaviour for delivering drug molecule. The overexpression of folic acid receptor by many cancer cells has been extensively studied [210]. It is a 38 kDa glycosylphosphatidylinositol-anchored protein and has been considered as a potent target for a tumour specific drug delivery [211]. FR has a very high affinity (K_d < 1 nM) to folic acid (FA). FA is a vitamin required for normal metabolism of all cells. However, the requirement of FA in fast dividing cancerous cells is higher because of their over-consumption and fast metabolic rate. To satisfy the extra need of FA, cancer cells overexpress the FR and uptake the FA via receptor-mediated endocytosis [210, 211].

Several nanoscale drug delivery vehicles have been evaluated till date [198]. In this regard, carbon nanotubes (CNT) are getting attention due to their potential advantages over other extensively studied metal nanoparticles. This includes a high length to width aspect ratio to carry a heavy dosage of drug molecules along with the ligand for ligand-target interaction. Its extremely low weight favour the easy cellular uptake, provide stability to the drug for its longer circulation time, enhanced bioavailability and apt biodistribution [127, 131, 212]. CNTs have extensively been investigated in free and composite form (mixed with some polymer) for their potential to deliver nucleic acid, protein and drug molecules for anticancer therapy [113]. Near infrared light (NIR) (700 nm to 1000 nm) can penetrate the biological tissue hence attracted tremendous attention from researchers to apply it as a stimulus for drug

delivery. CNTs also exhibited photothermal cancer therapy by producing heat and triggering on-demand drug release by absorbing NIR radiation [213].

The CNTs have been extensively employed as a nanofiller of different plymer matrix such as chitosan, gelatin, poly ethylene glycol (PEG), polyvinyl alcohol (PVA) etc., to form nanocomposite hydrogel. The addition of CNTs to these polymer matrix showed the enhanced mechanical, electrical and thermal properties of their nanocomposite form [214]. The pulsatile drug release profile was obtained in response to electric field application to CNT-polymethylacrylic acid hybrid hydrogel [215]. Whereas, Zhou, Liu et al. presented NIR light responsive CNT loaded thermosensitive hydrogel for chemo photo thermal therapy [144]. Therefore, nanocomposite smart materials exhibits outstanding applications in drug delivery applications [214].

As stated, both silk and CNT offer many advantages individually for drug delivery applications. However, there has been no report available which deals with SWCNT and silk hydrogel combination for localized targeted on-demand drug delivery. In the present work, we have investigated to utilize the individual properties of both to form a conductive, NIR light responsive nanocomposite silk hydrogel. Extensive in vitro cell culture study was performed to confer the specific toxicity on FR^{+ve} cancer cells by DOX-loaded FA functionalized SWCNT. Silk nanocomposite hydrogels were characterized through rheology. Further, DOX and SWCNT release from the hybrid hydrogel was monitored in presence of protease, pH, temperature and NIR laser stimulation.

3.2. Materials and methods

3.2.1. Materials

Carboxylic acid functionalized single-walled carbon nanotubes (COOH-SWCNT) was procured from Nanoshel Pvt. Ltd., USA. 1-(3-Dimethylamino propyl)-3-ethyl carbodiimide hydrochloride (EDC) from Himedia, India. 2,2′-(ethylenedioxy)-bis-(ethylamine) (EDEA), folic acid (FA), Methylthiazolyldiphenyl-tetrazolium bromide (MTT), doxorubicin (DOX), Propidium iodide (PI), protease XIV from *streptomyces griseus* and Lactate dehydrogenase (LDH) release assay kit from Sigma, Aldrich, USA. Nitric acid (HNO_3) and Sulphuric acid (H_2SO_4) from Merck, India.

3.2.2. Preparation of SWCNT-FA/DOX

Dispersion of COOH-SWCNT into the water was performed with the modification of previously published protocol[216]. Briefly, COOH-SWCNT were probe sonicated (5 s on/ 5 s off cycle, 34 % amplitude) in the mixture of H_2SO_4 and HNO_3 in 3:1 (v/v) ratio for 30 min. Acid was removed by centrifugation at 40,000 g for 1 h, washed and COOH-SWCNT were re-dispersed in sodium phosphate buffer pH 5.5 by 15 min sonication. COOH-SWCNT were amine functionalized by using one-step EDC crosslinking. COOH-SWCNT:EDC:EDEA weight ratio was maintained to 1:3:3 at pH 5.5 for 4 h with continuous mixing on rotospin (Tarson Pvt. Ltd., India). The resultant NH_2-SWCNT were then collected by centrifugation at 40,000 g for 1 h followed by its washing with pH 5.5 buffer. Similarly, folic acid dissolved in 0.5 N NaOH was cross-linked to NH_2-SWCNT by EDC. NH2-SWCNT:EDC:FA were mixed in a ratio of 1:3:3 at pH 5.5 for 4 h with continuous mixing on rotospin. The resultant SWCNT-FA was collected by centrifugation at 40,000 g for 1 h followed by its washing and re-suspension in sodium carbonate buffer pH 9.1. Further, DOX was added to SWCNT-FA in a ratio of 1:3 (w/w). Free DOX (fDOX) remained unadsorbed and was removed by centrifugation at 40,000 g for 1 h followed by washing until supernatant becomes colourless. The loading efficiency was calculated using following formula –

$$\% \text{ DOX loading efficiency} = 100 \times [(W_{\text{feed DOX}} - W_{\text{free DOX}})/W_{\text{feed DOX}}]$$

Where, $W_{\text{feed DOX}}$ = weight of total DOX added, $W_{\text{free DOX}}$ = weight of fDOX remained in the supernatant after centrifugation **(Figure A3.1)**.

3.2.3. Physical characterization of prepared SWCNT-FA/DOX

Field emission scanning electron microscope (FESEM) and Field emission transmission electron microscope (FETEM). Approximately 100 µl of COOH-SWCNT (100 µg/ml) dispersed in pH 7.4 buffer was spread over the coverslip and air-dried overnight. The coverslip fixed on stub through carbon tape was followed by gold sputtering and then images were captured using FESEM (Zeiss, Sigma). Approximate length and diameter of COOH-SWCNT were estimated using ImageJ software (Wayne Rasband, National Institute of Health, USA) (100 SWCNT were measured). For FETEM 10 µl of COOH-SWCNT (100 µg/ml) was dried over carbon grid and images were captured using FETEM, Jeol, Japan.

Dynamic light scattering (DLS). Polydispersity Index (PDI), hydrodynamic radius and zeta potential of all the synthesized construct at 10 µg/ml concentration was measured using Malvern Zetasizer Nano, UK. COOH-SWCNT dispersed in PBS pH 5.5, pH 7.4 and sodium carbonate buffer pH 9.1. Whereas, NH_2-SWCNT, SWCNT-FA and SWCNT-FA/DOX dispersed in PBS pH 7.4. Size and zeta potential were measured at 90^o angle light scattering for 3 measurements of automatically calculated time.

Fourier transform infrared (FTIR) spectroscopy. The infrared spectra of all the construct formed at different steps were recorded using FTIR (Perkin Elmer BX). Samples were mixed with KBr to form a pellet and scanned from the frequency range of 400 to 4000 cm^{-1} and averaged over 4 runs. Data was represented in the region of interest between 800 to 1800 cm^{-1} in results section.

UV-visible spectroscopy. UV-visible spectroscopy of all the samples was carried out in Varian Cary 100 spectrophotometer (Agilent Technologies, USA). fFA (25 µg/ml), fDOX, SWCNT and SWCNT-DOX (50 µg/ml), SWCNT-FA and SWCNT-FA/DOX (10 µg/ml) were scanned from 200 nm to 600 nm wavelength to plot absorption spectra. SWCNT-FA and SWCNT-FA/DOX were diluted due to high loading of DOX and folic acid modification. Standard plot for SWCNT concentration determination was plotted at 808 nm **(Figure A3.2).**

3.2.4. Extraction of silk fibroin (SF) protein from *Bombyx mori* (*BM*) cocoons and *Antheraea assama* (*AA*) silkworm glands

The method for isolation of SF protein was described elsewhere[217]. In brief, mulberry BM cocoons were chopped into small pieces. To remove sericin, cocoon pieces were degummed into boiling 0.02 M Na_2CO_3 and obtained silk fibres were washed with distilled water and dried overnight. Silk fibres were then dissolved in 9.3 M LiBr and dialyzed against milli-Q water for 3 days to remove LiBr. Whereas, nonmulberry AA silkworm glands were isolated from fully-grown fifth-instar mature larvae. The silk protein was isolated from these glands and dissolved in 1% (W/V) SDS followed by its dialysis against milli-Q water for 4 hr. SF protein concentration in terms of percentage was determined by the gravimetric method.

3.2.5. Preparation of injectable Silk@SWCNT-FA/DOX nanocomposite and Silk@fDOX hydrogel

Injectable silk hydrogel was prepared by blending mulberry (BM) and nonmulberry (AA) SF protein. The final protein weight percent in hydrogels was maintained by *BM* to *AA* weight % ratio. 3% Injectable silk hydrogel was prepared by blending BM and AA in 1.5:1.5 (1.5 wt% BM blended with 1.5 wt% AA), 2:1 (2 wt% BM blended with 1 wt% AA) and 1:2 (1 wt% BM blended with 2 wt% AA) weight % ratio, however, for 4% they were blended in 3:1 (3 wt% BM blended with 1 wt% AA) ratio. The predetermined concentration of DOX and SWCNT-FA/DOX were incorporated during the blending of two silk proteins.

3.2.6. Rheological studies

Gelation time. BM and AA silk solution in 1:2 weight % ratio along with SWCNT-FA was mixed, and the blended solution was placed on the rheological platform under the parallel plate at 1 mm gap distance. At constant shear strain (0.2%), angular frequency (ω) (10 rad/s), and temperature (37 °C), the measurement was performed for 20 min using Anton Parr MCR302 rheometer. The obtained storage modulus (G') and loss modulus (G") was plotted against time to calculate the gelation point.

Amplitude sweep. Shear strain from 0.01 to 100 % was applied over the 1:2 (BM:AA) nonloaded, 100 µg SWCNT-FA/DOX, and 100 µg fDOX loaded silk hydrogel by keeping the angular frequency constant at 1 rad/s. The obtained G' and G" was then

plotted against percentage shear strain and used to calculate linear viscoelastic (LVE) region and yield point for all gels.

Frequency sweep. Angular frequency from 0.1 to 100 rad/s was applied over the different hydrogels with their respective LVER shear strain. The obtained G', G" and complex viscosity was plotted against angular frequency. The obtained loss factor and complex viscosity were also plotted against angular frequency.

Thixotropy. The hydrogels were subjected to low shear strain (LVE region) and high shear strain (above yield point) for multiple times to assess the recoverability of prepared gel.

3.2.7. Swellability and degradation of the hydrogel

Injectable silk hydrogel prepared by blending of different weight % ratio of BM and AA were placed in a PBS buffer (pH 7.4). The swelling was calculated by weighing the hydrogel before and after the placement of hydrogel in PBS buffer. For the degradation study 2 U/ml protease was added to PBS (pH 7.4) and every 3rd day, PBS was removed and hydrogel weight was measured. The % of hydrogel degraded was calculated using the following formula[217] –

% mass degraded = [(Wi – Wt)/Wi] x 100

Where Wt is the weight of hydrogel at a given interval, and Wi is the initial weight of the hydrogel.

3.2.8. Release studies

DOX release from SWCNT-FA/DOX. DOX release from SWCNT-FA/DOX was observed at various combinations of incubation temperature (37 °C and 45 °C) and pH (7.4 and 4.5) of the medium over time. The release was also determined post-NIR light irradiation. The SWCNT-FA/DOX suspension was centrifuged at 40,000g for 1h after pre-decided time point, and the supernatant containing fDOX was replaced with fresh buffer. The fDOX release was calculated from the collected supernatant by DOX fluorescence standard plot (excitation 480 nm, emission 560 nm), as shown in **Figure A3.3**.

SWCNT-FA/DOX release from hybrid silk hydrogel. 100 µl hybrid silk hydrogel containing predetermined concentration (50, 100, 150, and 200 µg) of SWCNT-FA/DOX per gel were prepared in Eppendorf tubes. These gels were placed in a PBS pH 7.4 containing 1 U/ml of protease. The release of SWCNT-FA/DOX due to hydrogel degradation was observed by DOX characteristic fluorescence detection.

Two sets of 100 µl hybrid hydrogel containing 100 µg SWCNT-FA/DOX were placed in PBS pH 7.4 and pH 4.5 buffer. One set was then incubated at 37 °C and another at 45 °C temperature incubator. 200 µl of PBS was collected at a predetermined time point for SWCNT-FA/DOX release. The DOX fluorescence was measured by excitation at 480 nm, and emission was collected at 560 nm using Tecan Infinite Pro, Switzerland.

The response of SWCNT-FA/DOX and nanocomposite hydrogel to NIR laser was also measured. Pig skin was sourced from local abattoir, which was further cleaned and sterilized overnight. Silk@fDOX hydrogels and Silk@SWCNT-FA/DOX nanocomposite hydrogels were prepared in Eppendorf tube and immersed into PBS pH 7.4. The nanocomposite hydrogel was covered with pig skin from the top and NIR laser of 500 mW output power, and 808 nm wavelength was shined through the pig skin. DOX release was then measured by fluorescence detection, as mentioned earlier.

3.2.9. *In vitro* studies

3.2.9.1. Cell culture

Folic acid receptor-positive (FR^{+ve}) Oral cancer cell line KB and Folic acid receptor-negative (FR^{-ve}) lung cancer cell line A549 were procured from NCCS, Pune, and cultured in high glucose DMEM (Invitrogen, USA) in 5% CO_2 incubator and 37 °C temperature. All the experiments were performed in folic acid deficient high glucose DMEM (Himedia, India).

3.2.9.2. Cell viability assay

MTT is a yellow color compound, which reduced by active mitochondrial dehydrogenase enzyme to form purple color formazan, which further solubilized in dimethyl sulfoxide (DMSO) and absorbance was recorded at 570 nm. The absorbance is directly proportional to the number of viable cells. Approximately 10^4 cells were seeded into each well of 96 well plates. After 24 h of seeding cells were treated with SWCNT-FA, fDOX and SWCNT-FA/DOX for 24 h, however, untreated cells were used as a control. Post-

treatment 10 µl of MTT (from 5 mg/ml stock) was added to each well and incubated at 37 °C for 3 h. Formed purple color formazan was then re-suspended in 100 µl of DMSO and absorbance was taken at 570 nm wavelength in the Multiplate reader (Tecan Infinite Pro, Switzerland).

3.2.9.3. Reactive oxygen species (ROS) measurement

2 x 10^5 Cells were seeded in 6 well plate and treated with 0.5 µg/ml SWCNT-FA/DOX and fDOX. Post 48 h of treatment cells were incubated with 10 µM dichloro-dihydro-fluorescein-diacetate (DCFH-DA) for 1 h at 37 °C followed by its trypsinization and analysis through BD FACS Calibur (BD Biosciences, USA).

3.2.9.4. Lactate dehydrogenase activity assay

To determine the cellular damage LDH assay was performed. LDH is an oxidoreductase enzyme, which released out from cell due to cellular damage. 10^4 cells (both KB and A549) were seeded in each well of 96 well plate and allowed to adhere for 24 h followed by treatment with 0.5 µg/ml of fDOX and SWCNT-FA/DOX for 48 h. post-treatment 50 µl of supernatant was collected for LDH release assay. LDH assay was performed as per manufacturer protocol (Sigma Aldrich, USA).

3.2.9.5. Cell apoptosis assay

Cell apoptosis was determined using Alexa Fluor 488 annexin V/sytox red (Invitrogen) dead cell apoptosis kit as per the manufacturer protocol (catalog no-V13241). Sytox red (catalog no-S34859) was used in place of propidium iodide (PI) to avoid DOX-PI fluorescence spillover. The data acquisition was carried out using BD Accuri C6 Plus flow cytometer and represented as a dot plot.

3.2.9.6. Cell cycle analysis

The cell cycle was analyzed through PI. Cells (KB and A549) seeded in 6 well plates were treated with 0.5 µg/ml of fDOX and SWCNT-FA/DOX for 6 h, 24 h, 48 h, 72 h, and 96 h. Post-time-dependent treatment cells were trypsinized, centrifuged, and fixed in 70% chilled ethanol. After fixation overnight at -20 °C, ethanol was removed by centrifugation at 1500 rpm for 5 min, and the cell pellet was washed with PBS twice. To avoid non-specific binding of PI to RNA, 50 µg/ml of RNase treatment was given at 37

°C for 1 h. 10 µg/ml of PI was then added with gentle pipetting and cell cycle was analysed through BD FACS Calibur (BD Biosciences, USA).

3.2.9.7. SWCNT-FA Specific uptake assay

To track SWCNT-FA inside the cell, the construct was tagged with FITC. SWCNT-FA:FITC ratio was maintained to 1:3 (w/w), and the mixture wrapped with aluminum foil was kept on rotospin for 4 h at room temperature. Sodium carbonate pH 9.1 buffer was used for the reaction. Finally, SWCNT-FA/FITC conjugate was recovered as a pellet after centrifugation at 40,000g for 1 h. Remaining free FITC was decanted, followed by a 3-4 round of washing (till the supernatant become colorless).

2 x 10^5 cells (both KB and A549) were seeded in each well of the 6-well plate. Cells were cultured in high glucose DMEM without FA to stimulate the overexpression of folic acid receptor. Post 24 h of seeding, the cells were treated with 5 µg SWCNT-FA/FITC for 2 h followed by washing with PBS pH 7.4. The cell nucleus after treatment was stained with Hoechst-33342 (Sigma Aldrich, USA) for 2 min, and images were captured with a fluorescence microscope (EVOS XL Digital microscope). The pathway for the uptake of SWCNT-FA was deciphered by preventing the endocytosis pathway using NaN_3, cytochalasin, and nystatin. To further confirm the FR-based SWCNT-FA uptake 2 mM free FA (fFA) treatment was given pre SWCNT-FA/FITC treatment.

3.2.9.8. Gene expression studies

Both KB and A549 cells were treated in 6 well plates similar to our previous experiment. RNA was isolated manually using Tri-reagent (Sigma Aldrich, USA). Briefly, 250 µl of TRI-reagent was directly spread over tissue culture plate followed by pipetting and transferred it into the Eppendorf tube. Cell debris was removed by centrifugation at 13000 rpm for 15 min, and the supernatant was transferred into another tube. 25 µl of chloroform was added by vortex and tubes incubated at RT for 1 h. Due to phase separation, three layers were formed by centrifugation. The top layer contains RNA, the middle layer contains DNA, and the bottom layer contains proteins. Gently the top layer was collected in the new tube. An equal volume of ice-chilled isopropanol was added, followed by the vortex. RNA precipitates were observed after 4 h of incubation at -20 °C. Centrifugation at 13,000 rpm for 20 min formed the pellet. The RNA pellet was washed with ice-cold 70% DNase RNase free ethanol. Finally, RNA pellets were dissolved in 20 µl water and preserved at -20 °C [218] for further use.

1 µg of RNA was used for the synthesis of cDNA using Applied Biosystems cDNA synthesis kit following manufacturer protocol. Synthesized cDNA was further diluted 10 times for real-time PCR analysis. Primers used for real-time PCR are given in **Table 3.1**.

Table 3.1 – List of primers used for gene expression analysis using real-time PCR.

Short name	Primers	Accession number
hFas Receptor (F)	TGAAGGACATGGCTTAGAAGTG	NM_001320619.1
hFas Receptor (R)	GGTGCAAGGGTCACAGTGTT	
hCaspase-8 (F)	CTGCTGGGGATGGCCACTGTG	NM_001080125.1
hCaspase-8 (R)	TCGCCTCGAGGACATCGCTCTC	
hP53 (F)	GCCCAACAACACCAGCTCCT	NM_001126115.1
hP53 (R)	CCTGGGCATCCTTGAGTTCC	
hBcl 2 (F)	TTGTGGCCTTCTTTGAGTTCGGTG	NM_000657.2
hBcl 2 (R)	GGTGCCGGTTCAGGTACTCAGTCA	
hBax (F)	CCTGTGCACCAAGGTGCCGGAACT	NM_001291431.1
hBax (R)	CCACCCTGGTCTTGGATCCAGCCC	
hApaf-1 (F)	TGGAATGGCAGGCTGTGGGA	NM_013229.2
hApaf-1(R)	TGCACTCCCCCTGGGAAACA	
hCyt-c (F)	ATGGTCTCTTTGGGCGGAAG	NM_018947.5
hCyt-c (R)	GGCAGTGGCCAATTATTACTCA	
hFA Receptor (F)	GGACAGACATGGCTCAGCG	NM_016725.2
hFA Receptor (R)	TGTGGTGCTTGGCGTTCATG	

3.2.9.9. *In vitro* functional bioactivity assessment of Silk@SWCNT-FA/DOX nanocomposite hydrogel

100 µl silk hydrogel loaded with either 100 µg SWCNT-FA/DOX or fDOX or 33 µg SWCNT-FA (equivalent to SWCNT-FA concentration in SWCNT-FA/DOX). Each hydrogel (n=3) was incubated in 2 ml DMEM cell culture media supplemented with 10% FBS and 1 % antibiotic. For in vitro cytotoxicity, A549 and Kb cell were culture in a 96 well plate separately and all hydrogels were incubated in a 37 °C incubator separately. The hydrogels were exposed to NIR light at a predefined interval (8 h before leachate

collection) for 15 min under the sterile condition. The leachate (media containing SWCNT-FA/DOX or fDOX or SWCNT-FA released from silk hydrogel) was collected at 12 h, 36 h, 72 h and 120 h. The media of both A549 and KB cells were replaced with the leachate and 0.5 µg/ml concentration of free form of SWCNT-FA/DOX and fDOX. Cells were maintained in CO2 incubator for 48 h and percentage cell viability was assessed using MTT afterward as described previously.

3.2.10. Statistical analysis

All the experiments were performed in triplicate (n = 3) and results were expressed as a mean ± standard deviation. One-way analysis of variance (ANOVA) and Turkey's test was performed to statistically analyse the data and to check for any significant difference among sampling groups (OriginPro 8.0 software). Statistically, significance among the groups was then represented as *p < 0.05 unless otherwise mentioned in the figure legends.

3.3. Results

3.3.1. Preparation and physical characterization of SWCNT-FA/DOX

The dispersion of SWCNT into the water was obtained by its pre exposure to the mixture of acid followed by ultrasonication. As presented in **Table 3.2** the hydrodynamic radius of COOH-SWCNT varies with pH. The hydrodynamic radius of COOH-SWCNT was lowest in alkaline pH 9.1, with a highly negative zeta potential of -31.2 ± 0.65 which prevent the formation of any aggregation and represent its stability. However, at low pH hydrodynamic radius increased with less negative zeta potential (-16.9 ± 0.71). The Smaller polydispersity index (PDI) of 0.29 ± 0.04 confirmed the even distribution of COOH-SWCNT. The COOH group present over the surface of SWCNT was replaced by primary amine group using EDC crosslinking. Structurally EDEA is a linear polymer with a primary amine group at its both ends. At pH 5.5 EDC reacts with COOH group of SWCNT to form an unstable complex which further replaced by EDEA amine group to form an amide bond and leaves free primary amine group on to SWCNT (NH_2-SWCNT) surface. The less negative zeta potential of -12 ± 0.68 and reduced hydrodynamic size of 666.1 ± 23.98 nm of NH_2-SWCNT confirms the reaction. Similarly, COOH functional group of FA activated with EDC and cross-linked to NH_2-SWCNT to form SWCNT-FA had a negative surface charge of -21.4 ± 0.65 and 447.6 ± 5.03 nm hydrodynamic size. However, 0.33 ± 0.05 PDI of SWCNT-FA signifies its stability and even distribution.

One of the principal advantages of using SWCNT is its ability to accommodate the high amount of drug. SWCNT due to tube-like structure and high negative surface charge encapsulates the cationic drug DOX into the cavity as well as adsorb it onto the surface. Combining all the factors together like molecular structures, electrostatic interactions and Vander wall forces three times weight by weight DOX was loaded onto SWCNT-FA (i.e. each microgram of SWCNT carried approximately 3 µg of DOX). Hence the hydrodynamic size of DOX-loaded SWCNT-FA was further increased to 777 ± 23.73 nm and zeta potential moved towards neutral to -3.96 ± 0.386 with PDI of 0.505 ± 0.035.

Table 3.2 – Hydrodynamic radius, polydispersity index and zeta potential of differently modified SWCNTs through DLS.

Sample name	Size (nm)	PDI	Zeta Potential
COOH-SWCNT, pH 9.1	723.2 ± 9.27	0.32 ± 0.02	-31.2 ± 0.65
COOH-SWCNT, pH 7.4	1675 ± 63.51	0.34 ± 0.01	-23.3 ± 1.39
COOH-SWCNT, pH 5.5	1198 ± 72.34	0.29 ± 0.04	-16.9 ± 0.71
NH_2-SWCNT, pH 5.5	666.1 ± 23.98	0.34 ± 0.02	-12 ± 0.68
SWCNT-FA	447.6 ± 5.03	0.33 ± 0.05	-21.4 ± 0.65
SWCNT-FA/DOX	777 ± 23.73	0.50 ± 0.03	-3.9 ± 0.38

In agreement with our DLS data FETEM image also confirm the SWCNT dispersion as shown in **Figure 3.1A** Observed average length and diameter of SWCNT calculated from FESEM image was 914.73 ± 409.83 nm and 46.05 ± 14.43 nm respectively **(Figure A3.4)**. UV-visible spectra in **Figure 3.1B** also confirms the presence of different characteristic absorbance peak. FA absorbance spectra gave a characteristic strong peak at 250 nm and 360 nm [219]. COOH-SWCNT, however, have no absorbance maxima (λ_{max}) but when it was functionalized with FA to form SWCNT-FA, FA characteristic peaks were detected. The λ_{max} of DOX was observed at 480 nm, which appeared in SWCNT-FA/DOX as well as SWCNT/DOX. However, the absorbance peak at 480 nm was very small due to the hindrance caused by SWCNT.

The modification of SWCNT with functional groups was analysed using FTIR **Figure 3.1C**. Carboxylate functional group characteristic peak at 1583 cm^{-1} and 1384 cm^{-1}, C=O stretch at 1225 cm^{-1} and OH out of plane bending at 871 cm^{-1} was observed in COOH-SWCNT but disappeared when it was modified to NH_2-SWCNT. However, characteristic amide functional group at 1651 cm^{-1} and primary amine C≡N stretch at 1085 cm^{-1} appeared in NH_2-SWCNT and SWCNT-FA spectra. A very weak COOH shoulder peak was also observed in SWCNT-FA, which might be coming from unreacted COOH group of FA. A strong COOH group specific peaks again appeared in SWCNT-FA/DOX spectra due to the presence of adsorbed DOX onto SWCNT-FA surface [220].

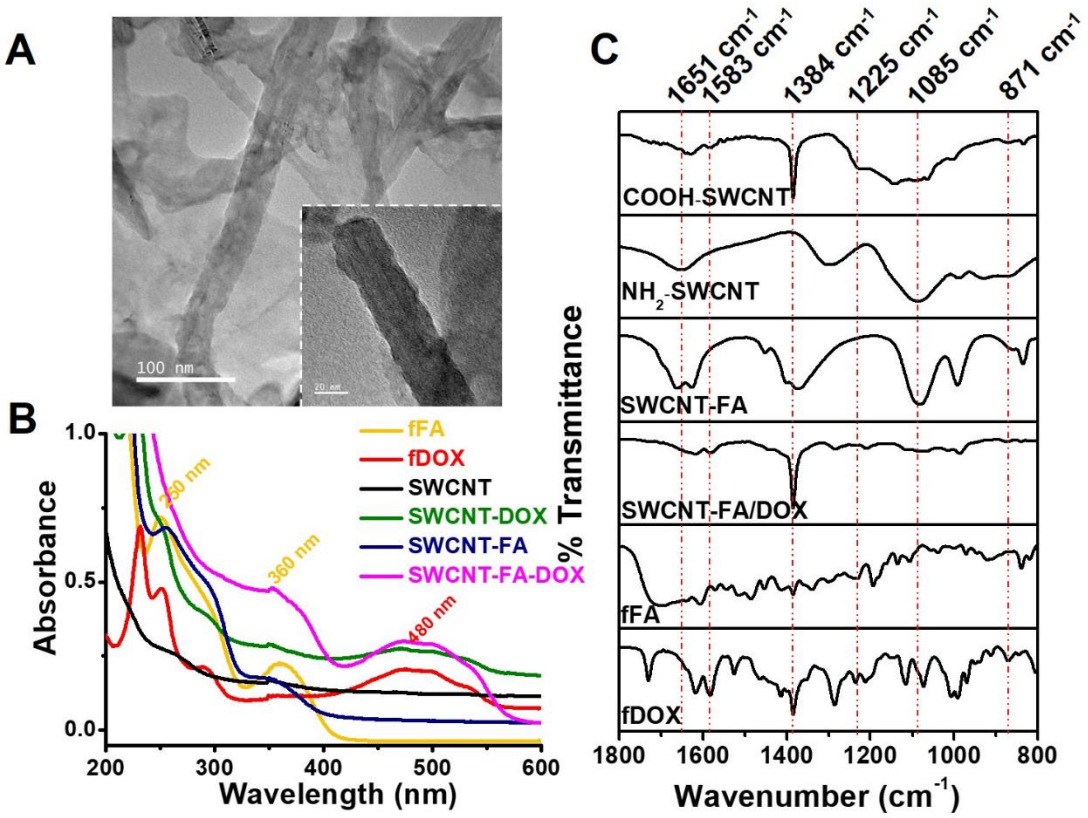

Figure 3.1. ***(A)*** *FETEM image of SWCNT and physical characterization of SWCNT-FA/DOX preparation through* ***(B)*** *UV-Visible spectroscopy and* ***(C)*** *FTIR.*

3.3.2. Preparation and characterization of injectable SWCNT loaded nanocomposite silk hydrogel

We have used two variants of the silk (BM and AA) for the preparation of injectable hydrogel. The hydrogel formation was observed soon after their blending. BM and AA were blended in different combinations to ultimately form 3% and 4% hydrogel. The hydrogel didn't show any significant swelling even after 72 h of incubation in PBS **(Supplementary Figure A3.5)**. All hydrogels combinations were further subjected to protease degradation. Hydrogels showed slow degradation profile **Figure 3.2A**. A significant difference was observed in the degradation rate of 3% and 4% hydrogel. However 1:2 hydrogel (1 weight percent BM blended with 2 weight percent AA) has shown higher degradation than other combination of the hydrogels. At higher percentage, the degree of crosslinking between two silk is higher making it more compact with small pore size and therefore less vulnerable to degradation due to lesser enzyme e penetration. The degradation of the hydrogel is considered as an essential phenomena for the release

of the embedded nanoparticle-loaded drug. On this basis, 1:2 ratio hydrogel has been selected for our further studies.

The gelation point study **Figure 3.2B** indicated BM and AA having higher loss modulus (G") than storage modulus (G') immediately after blending. However, at approximately 11.5 min the G' intersected G" and dominated. Hence, 11.5 min was considered as a gelation time point for 1:2 weight % ratio of BM:AA blended hydrogel. However, the addition of SWCNT further delayed the gelation time in a concentration-dependent manner. During the blending, SWCNT was embedded nicely into silk hydrogel **(Figure A3.6)**. Blending of 50, 100 and 200 ug SWCNT with BM and AA delayed the gelation by approximately 0.5, 2.5 and 3.5 min respectively. The storage modulus of non loaded hydrogel reached to approximately 1000 Pa which didn't change with fDOX incorporation, however, SWCNT-FA/DOX incorporation doubled its strength with a storage modulus of approximately 2000 Pa **Figure 3.2C**. This range of storage modulus indicates the viscoelastic nature of formed gel. The yield point obtained for non loaded, 100 µg fDOX and 100 µg SWCNT-FA/DOX-loaded hydrogel was 1.4 %, 1 % and 0.6 % respectively. SWCNT-FA/DOX may be interfering during the reassembly of SF to form a gel. This may be the cause of delay in gelation point as well as a reduction in yield stress point. However, due to the very firm interaction between SF and SWCNT, the strength of the gel increased. Further frequency sweep at these respective yield points confirmed the increased stability and solid network structure of SWCNT-FA/DOX-loaded hydrogel compared to non loaded hydrogel **Figure 3.2D**. **Figure A3.7** indicated that tan delta of non loaded hydrogel was decreasing further after applying frequency beyond 10 rad/s. However, it remained consistent for Silk@fDOX hydrogel and Silk@SWCNT-FA/DOX nanocomposite hydrogel. The tan delta is an indicator of gel behaviour during the frequency sweep. The non loaded hydrogel therefore at higher frequency experienced gel to sol transition however hybrid hydrogel maintained its gel-like property throughout.

The viscosity of gel decreased with increasing angular frequency which dictates its shear thinning property and allows its injectability in a minimally invasive way **Figure 3.2E**. The thixotropy test in **Figure 3.2F** indicated the recoverability of hydrogel after applying high shear stress. At low shear stress the G'>G" indicated the solid gel structure, however, a sudden increase in shear stress caused G">G' indicated its fluid-like behaviour. As the stress from hydrogel was released it regained its solid gel structure

with same G'>G" **Figure 3.2F**. This indicates that post-injection gel will maintain its structure and other properties. The representative image of 1:2 blended injectable silk hydrogel is presented in **Figure 3.2G**. The Silk@fDOX hydrogel and Silk@SWCNT-FA/DOX nanocomposite hydrogel representative images are also presented in **Figure 3.2H**.

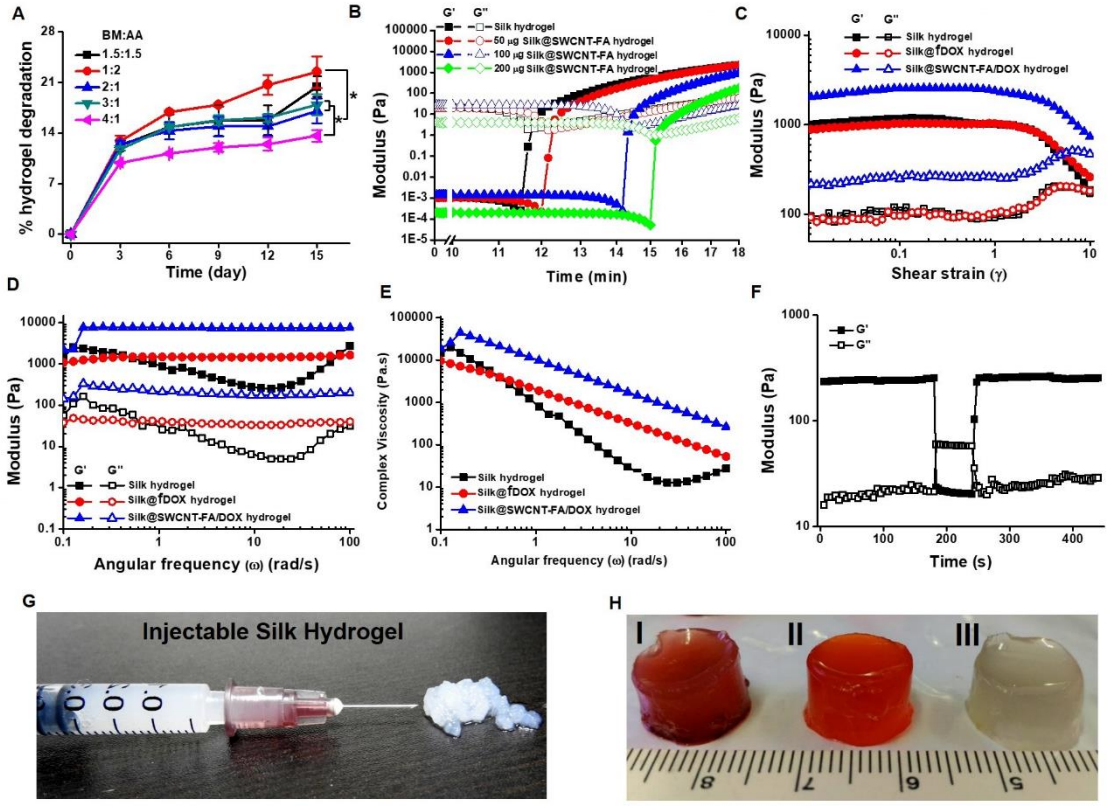

Figure 3.2. *Preparation and characterization of injectable silk hydrogel through* ***(A)*** *degradation profile,* ***(B)*** *gelation time point,* ***(C)*** *amplitude sweep,* ***(D)*** *frequency sweep,* ***(E)*** *shear thinning,* ***(F)*** *thixotropy,* ***(G)*** *Injectable hydrogel, and* ***(H)*** *representative images of (I) Silk@SWCNT-FA/DOX nanocomposite hydrogel, (II) Silk@fDOX hydrogel and (III) silk hydrogel.*

3.3.3. Release studies

The free SWCNT-FA/DOX showed pH and temperature-dependent release **Figure 3.3A**. At physiological pH 7.4 interaction between DOX and SWCNT-FA was very strong due to the π- π interaction and therefore, very little DOX was release at 37 °C. However, at 45 °C, significantly higher (approximately 15%) DOX release was observed after 100 h. Similarly, at acidic pH 4.5 and 37 °C, 20% DOX was released, which further increased to 40% at 45 °C **Figure 3.3A**. The temperature of SWCNT-FA increases due to SWCNTs heat conductive properties, and therefore it gets actuated to release the DOX in the

medium. Hence, the DOX release from SWCNT-FA is regulated by both pH and temperature **Figure 3.3A**.

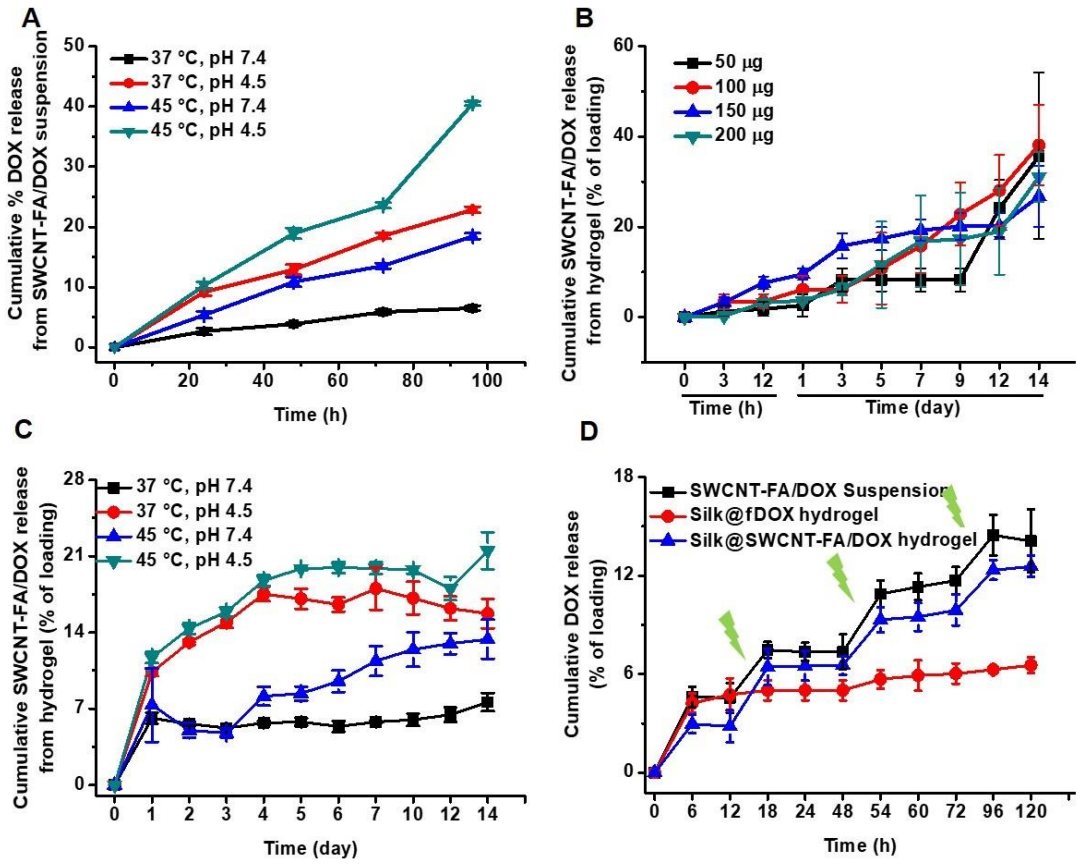

Figure 3.3. *DOX release from SWCNT-FA/DOX suspension and nanocomposite silk hydrogel.* ***(A)*** *The pH and temperature-dependent release of DOX from aqueously suspended SWCNT-FA/DOX,* ***(B)*** *degradation basis concentration-dependent release of SWCNT-FA/DOX from 1:2 blended silk hydrogel in the presence of 1 U/ml protease,* ***(C)*** *pH and temperature-dependent release of SWCNT-FA/DOX (100 µg/gel) from 1:2 blended nanocomposite silk hydrogel, and* ***(D)*** *NIR light-responsive DOX release from SWCNT-FA/DOX suspension and its nanocomposite silk hydrogel at pH 7.4.*

BM and AA blended in 1:2 ratio along with 50, 100, 150, and 200 µg of SWCNT-FA/DOX per gel and subjected to 2 U/ml protease for the degradation **Figure 3.3B**. In all the cases, the release was approximately 30-40% with respect to the amount of SWCNT-FA/DOX loading after 14 days. The amount of SWCNT-FA/DOX release was 17.5, 38, 42, and 62 µg for their respective loading (50 to 200 ug/gel) **Figure 3.3B**. The drug release was also constant till 14 days, which indicated that the rate of SWCNT-FA/DOX release was dependent on silk matrix degradation, and the desired release amount can be tuned by amount of loading **Figure 3.3B**. Further, we exposed 100 µg Silk@SWCNT-FA/DOX nanocomposite hydrogel to combinations of different pH and

temperature similar to **Figure 3.3A,** where, free SWCNT-FA/DOX was used. The initial burst release of approximately 7 and 10 % of SWCNT-FA/DOX was observed at both physiological pH 7.4 and acidic pH 4.5 incubated at physiological temperature 37 °C and high temperature 45 °C, respectively **Figure 3.3C**. The observed initial burst release was due to the diffusion of drug molecules present on the surface of the hydrogel. After the initial burst release, we did not see any significant release of SWCNT-FA/DOX at physiological temperature and pH (37 °C, pH 7.4). However, at physiological pH and higher temperature (pH 7.4, 45 °C) the release was sustained and reached to 14%. Similarly, Sustained-release (13%) of SWCNT-FA/DOX was also observed at low pH and physiological temperature (pH 4.5, 37 °C). These data indicated that individually both pH and temperature-induced the release of SWCNT-FA/DOX. However, the combination of both low pH and high temperature synergistically increased the release to 20% **Figure 3.3C**. The DOX release from hydrogel was higher in the presence of protease **Figure 3.3B** then low pH and high-temperature condition **Figure 3.3C**. Therefore degradation of hydrogel might be majorly responsible for DOX release, whereas pH and temperature could be a good stimulator for its faster release. SWCNT-FA/DOX, both in aqueous suspension and in nanocomposite form, showed the intermittent release pattern of DOX post-NIR laser illumination. As shown, the DOX release from SWCNT-FA/DOX **Figure 3.3A** and hybrid nanocomposite silk hydrogel **Figure 3.3C** was very poor at physiological pH and temperature (pH 7.4, 37 °C). Hence, a sudden DOX release observed post-NIR illumination in **Figure 3.3D** indicated the photothermal response of the formulation compared to control Silk@fDOX hydrogel.

3.3.4. *In vitro* cell cytotoxicity studies

Cell viability in the presence of SWCNT-FA, fDOX, and SWCNT-FA/DOX was assessed through MTT after 48 h treatment. Both KB and A549 cells were exposed to functionalized SWCNT-FA. At lower concentrations, SWCNT-FA was not cytotoxic for both the cells **Figure 3.4AI)**. It was observed that fDOX was equally cytotoxic to both KB and A549 cells, and experimentally obtained lethal dose LD50 was around 0.75 µg/ml **Figure 3.4AII**. However, DOX-loaded SWCNT-FA showed FR dependent toxicity **Figure 3.4AIII**. The cytotoxicity of SWCNT-FA/DOX at all the concentrations was significantly different for KB and A549 cells. LD50 values for KB cells remained the same, whereas it was increased to 10 times, that is 5 µg/ml for A549 cells. fDOX caused a significant increase in reactive oxygen species (ROS) formation, as revealed by

DCF fluorescence measured using a flow cytometer. DCFH-DA, a non-fluorescent dye becomes fluorescent in the presence of ROS. A very little change in the ROS level of A549 cells was detected in the presence of 0.5 µg/ml of both fDOX and SWCNT-FA/DOX after 48 h **Figure 3.4BI**. However, the Intracellular ROS level of KB cells was found to be increased in **Figure 3.4BII**.

LDH release is an indicator of cytotoxicity induction through necrosis or apoptosis. **Figure 3.4C** represents that fDOX stimulated the LDH release from both KB and A549 cells. However, SWCNT-FA/DOX caused significant LDH release only from KB cells. This may be due to less DOX availability to A549 cells and enhanced DOX availability to KB cells, respectively.

The Targeted delivery of DOX into FR positive cells was also confirmed by the induction of apoptosis. In **Figure 3.4D and 3.4E** lower left, lower right, upper left, and upper right panel of quadrant represent intact live, early apoptotic, late apoptotic and dead cells, respectively. The 93.9% and 62.6% of live intact cells in untreated group of A549 and KB cells were reduced to 21.9% and 39.1% due to fDOX treatment and 78.0% and 47.1% due to SWCNT-FA/DOX treatment respectively. This indicates that approximately 72% and 23.5% of A549 and KB cells have been moved into some phase of apoptosis due to fDOX treatment. However, due to SWCNT-FA/DOX treatment, the percentage A549 and KB cells moved into apoptosis was 15.9% and 15.5%, respectively. This data explains that the toxicity of DOX has reduced to 4.5 times for A549 (FR^{-ve}) cells; however, it remained the same for KB (FR^{+ve}) cells due to the following targeting strategy. **Figure 3.4EIII** also represented the even distribution of KB cells from early to late apoptosis to dead cells similar to fDOX treated cell **Figure 3.4EII,** which is not the case for A549 cells. In A549 cells **Figure 3.4DIII** very few cells were found in the early and late apoptotic phase, which may indicate the change in the pathway of DOX toxicity compared to fDOX treatment **Figure 3.4DII**.

The cell cycle assessment was performed to understand the state of both the cells post-free and targeted drug treatment. Both fDOX and SWCNT-FA/DOX arrested the cells in G2/M phase **Figure 3.4F and 3.4G**. fDOX treatment to A549 **Figure 3.4FI** and KB **Figure 3.4GI** cells caused S-phase arrest after 6 h, which subsequently over time moved to G2/M phase and sub G1 phase. Almost all the cells were arrested in G2/M phase after 48 h, and after that, the cells were moving into sub-G1 phase, and by 96 h all

the cells were either in G2/M phase or sub-G1 phase. The increment in the percentage of the sub-G1 cell population is an indicator of DNA damage caused by fDOX [221]. However, SWCNT-FA/DOX caused similar effects. Due to the slow and sustained release of DOX, ~95% of cells were arrested in G2/M phase without the appearance of the sub-G1 phase throughout.

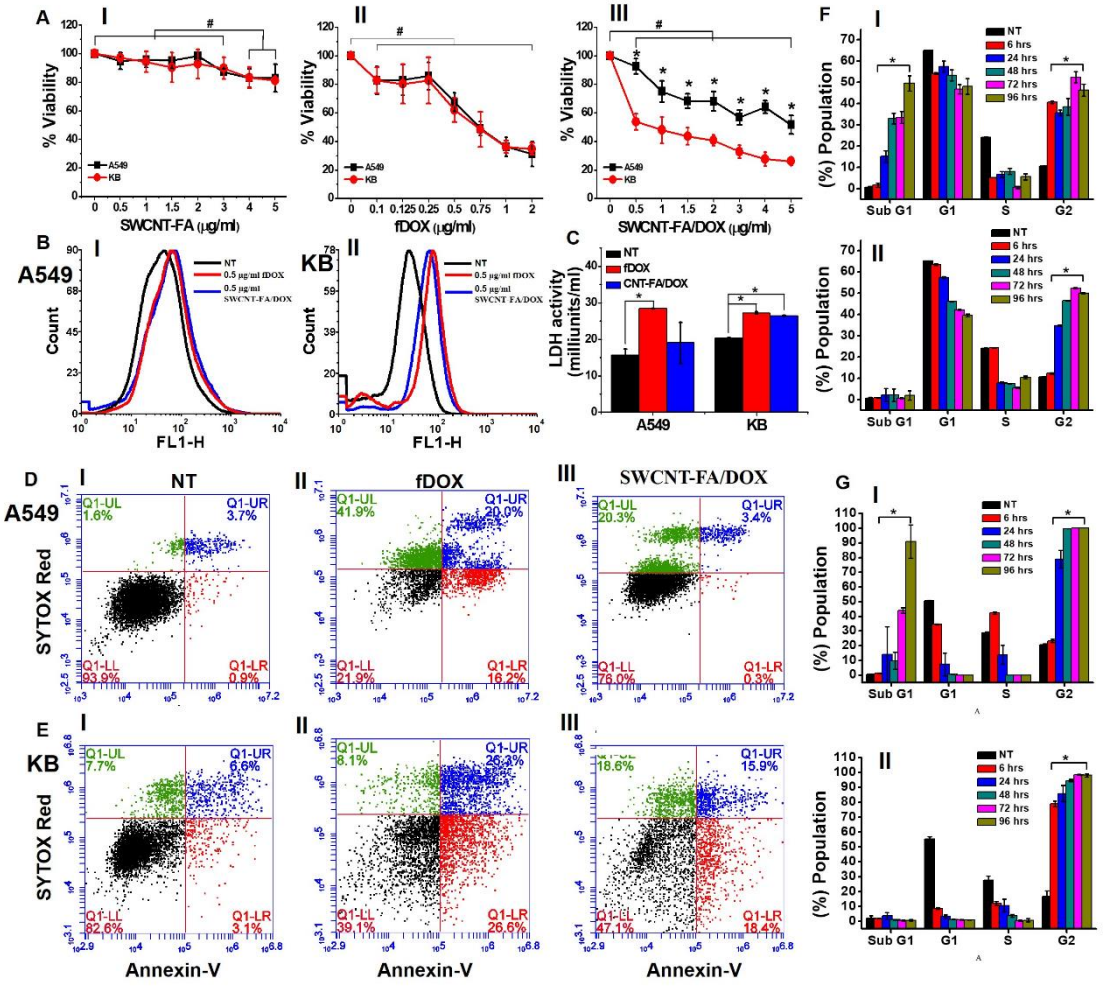

Figure 3.4. *A549 and KB cells were treated with (I) SWCNT-FA (II) fDOX and (III) SWCNT-FA/DOX at a given concentration for 48 h, and cell viability was assessed through MTT* ***(A)****. Both A549 and KB cells were further treated with 0.5 µg/ml of fDOX and SWCNT-FA/DOX for 48 h followed by ROS* ***(BI & BII)*** *and LDH release* ***(C).*** *The apoptosis was assessed using Annexin V–Sytox red for A549* ***(D)*** *and KB* ***(E)*** *for untreated (I), fDOX treated (II), and SWCNT-FA/DOX treated (III). A549* ***(F)*** *and KB* ***(G)*** *cells were treated with 0.5 µg/ml of fDOX (I) and SWCNT-FA/DOX (II) for predetermined time point, and Cell cycle was performed using PI. % of the cell population in sub-G1, G1, S, and G2 phases were represented as a respective bar plot. (Significance among the sample groups were represented as *p < 0.05, however, #p < 0.05 is represented as a significant difference between the sample and untreated group).*

3.3.5. Specific uptake and uptake mechanism of SWCNT-FA/DOX

fDOX was up taken equally by both KB and A549 cells; however, SWCNT-FA/DOX was up taken specifically by KB cells **Figure 3.5A** and not by A549 cells **Figure 3.5B**. Morphologically, the size of both cell types was found increased due to fDOX treatment **Figure 3.5A and 3.5B(e-h**), which may be an indicator of necrosis [221, 222]. However, change in morphology was not observed with the exposure of SWCNT-FA/DOX. Flow cytometry analysis further confirmed that 80% of fDOX was uptaken by KB cells within 4 h of treatment, and almost all the cells had fDOX after 8 h **Figure 3.5CI**. However, due to slow, sustained, and pH-dependent release of DOX from SWCNT-FA/DOX, only 10% of cells were loaded within 4 h, which slowly increased to 40% in 24 h and to 100% by 72 h. In contrast, the uptake of SWCNT-FA/DOX by A549 cells was negligible as compared to fDOX **Figure 3.5CII**.

The receptor-dependent endocytotic uptake of SWCNT-FA/DOX was determined by pre-treatment of KB cells **Figure 3.5D** with different endocytosis inhibitor. In untreated KB cells, SWCNT-FA labeled with FITC was internalized within 2 h of treatment. However, the 30 min pre-treatment of KB cells with NaN3, cytochalasin B, nystatin, and free folic acid (fFA) before SWCNT-FA/FITC treatment prevented its uptake. These inhibitors inhibit the various pathways of endocytosis. Such as clathrin or caveolin mediated uptake was inhibited by nystatin, the energy-dependent endocytotic pathway was inhibited by sodium azide, and macropinocytosis pathway was inhibited by cytochalasin B. Further fFA pre-treatment saturated all the freely available FR, which later prevent the uptake of SWCNT-FA/FITC.

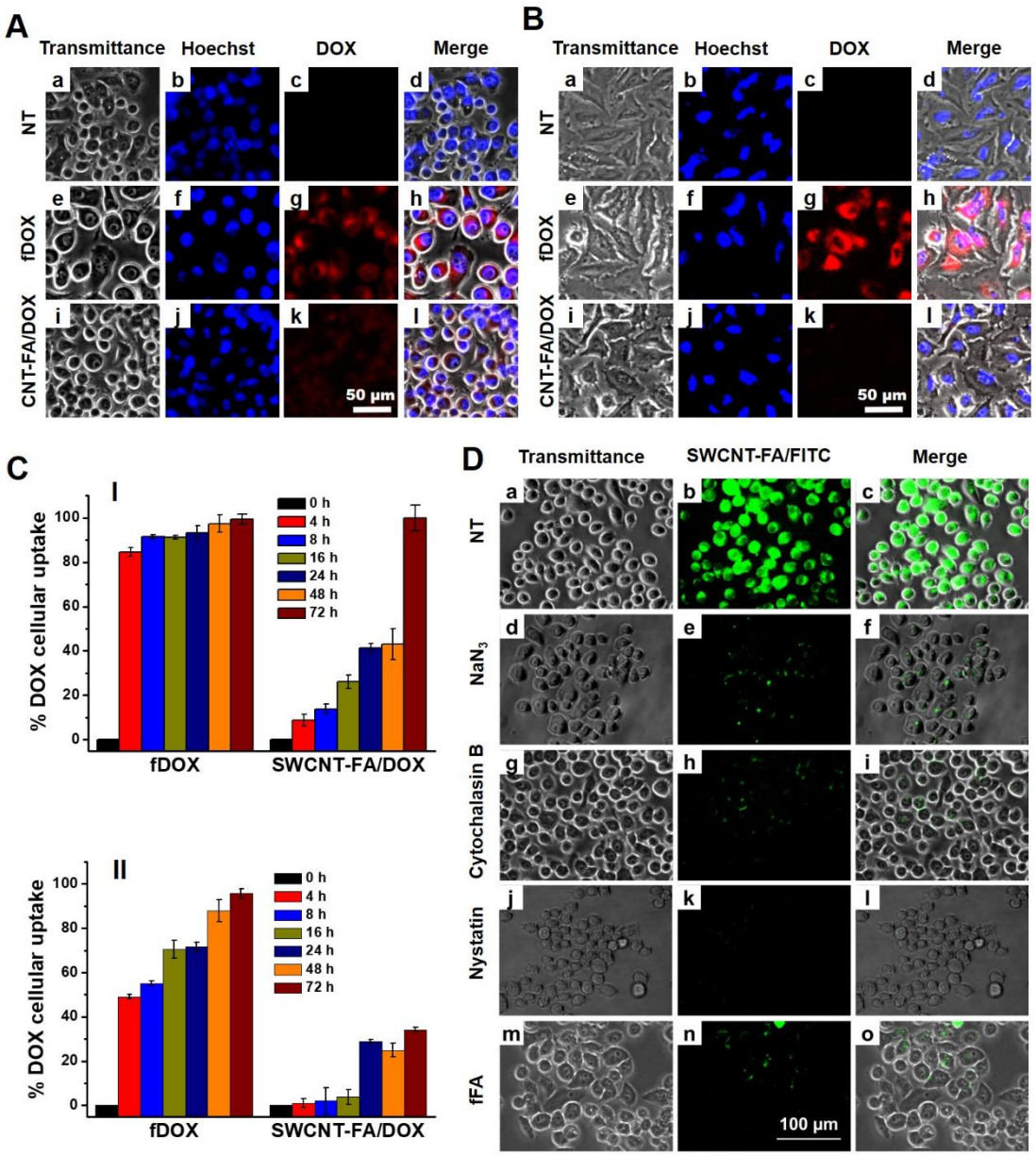

Figure 3.5. ***(A)*** *KB cells and* ***(B)*** *A549 cells were treated with fDOX (e, f, g, h) or SWCNT-FA/DOX (i, j, k, l) for 48 h and fluorescence images were taken in a fluorescence microscope. DOX fluorescence (a, e, i) was taken in RFP filter, Hoechst (b, f, j) was applied for 5 min to stain the nucleus. (c, g, k) are the transmittance images and (d, h, l) are the merged images.* ***(C)*** *Percentage DOX cellular uptake by (I) KB and (II) A549 cells were quantified using flow cytometer at indicated time point.* ***(D)*** *Pathway for the cellular uptake of SWCNT-FA was deciphered by tagging SWCNT-FA with FITC and different endocytosis inhibitor.*

3.3.6. Gene expression studies

Gene expression level of KB and A549 cells comprehensively assessed using real-time PCR. **Figure 3.6A** depicts the FR expression level only in KB cells and not in A549 cell. The treatment of fDOX and SWCNT-FA/DOX was given in DMEM without FA media, which further significantly enhance the FR expression level exclusively in KB cells. No significant changes in Bcl-2 expression levels were observed in A549 cells exposed to fDOX or SWCNT-FA/DOX. In contrast, a significant reduction in Bcl-2 expression was observed in KB cells exposed to SWCNT-FA/DOX **Figure 3.6B**. fDOX caused a significant increase in the expression level of Bax **Figure 3.6C** and Cyt-c **Figure 3.6D** in both KB and A549 cells. In contrast, the level of Bax and Cyt-c was significantly less in A549 cells while significantly higher in KB cells post-SWCNT-FA/DOX treatment. fDOX did not change the expression level of Apaf-1 either in KB or A549 cells **Figure 3.6E**; however, SWCNT-FA/DOX caused opposite effects in these two cells. The Apaf-1 expression level was significantly decreased in A549 cells while significantly increased in KB cells. The expression level of Caspase-8 **Figure 3.6F** and p53 **Figure 3.6H** was significantly enhanced due to exposure of fDOX in both KB and A549 cells. SWCNT-FA/DOX did not alter the expression of Caspase-8; however, a significant increase in p53 expression level was observed. fDOX also induced the Fas receptor expression in both KB and A549 cells. SWCNT-FA/DOX did not alter its expression in KB cells while enhanced its level in A549 cells **Figure 3.6G**. In general, our gene expression data suggested that SWCNT-FA/DOX specifically induced apoptosis in FR^{+ve} KB cells through different mechanisms then the apoptosis induced by fDOX in both KB and A549 cell. The cytotoxicity of DOX was attenuated for A549 cells and enhanced for KB cells while it was delivered through targeted vehicle SWCNT-FA.

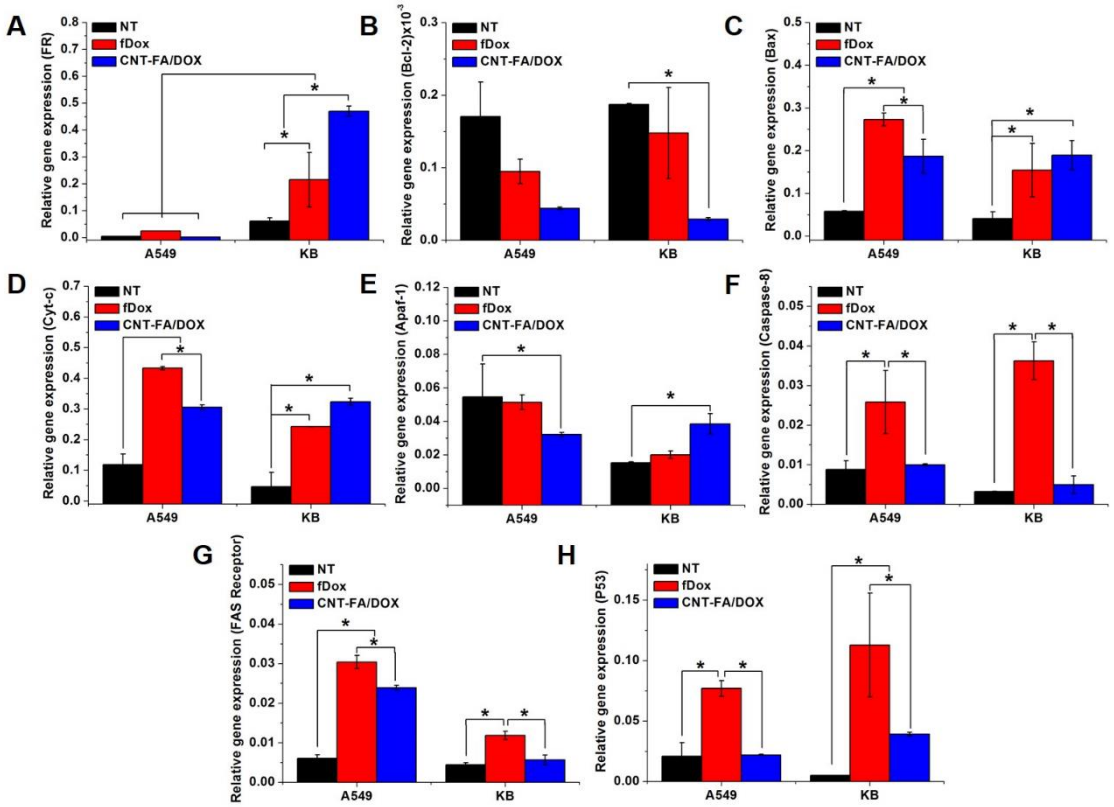

Figure 3.6. *Gene expression analysis using real-time PCR. Both KB and A549 cells were treated with 0.5 µg/ml of either fDOX or SWCNT-FA/DOX for 48 h followed by RNA isolation and cDNA synthesis. Real-time PCR was performed against (**A**) folic acid receptor (FR) gene, (**B**) Bcl-2, (**C**) Bax, (**D**) Cyt-c, (**E**) Apaf-1, (**F**) Caspase-8, and (**G**) FAS receptor and (**H**) P53 genes. GAPDH was used as a housekeeping gene to calculate relative gene expression of all the respective genes and plotted as a histogram. *p < 0.05.*

3.3.7. *In vitro* functional bioactivity assessment of nanocomposite silk hydrogel

Both A549 **Figure 3.7A** and KB **Figure 3.7B** cells were treated with SWCNT-FA suspension, SWCNT-FA/DOX suspension, fDOX suspension, and their silk hydrogel embedded form with and without NIR light stimulation. The Silk@SWCNT-FA hydrogel, without NIR light (**2**) and with NIR light exposure (**3**) was used as a biocompatibility control. We observed that in both the treatment (**2, 3**) 100% cell (A549 and KB) were normal until 120 h study. Both the cells were treated with 0.5 µg/ml of fDOX (**4**) and Silk@fDOX hydrogel leachate (**5**) for all the time points. We recorded 50% cell viability in both A549 and KB cells treated with fDOX; however, Silk@fDOX hydrogel leachate showed approximately 30%, 70%, 85%, and 90% cell viability for the 12 h, 36 h, 72 h, and 120 h leachate, respectively. Both the cells were also treated with 0.5 µg/ml SWCNT-FA/DOX (**6**) and its suspension exposed to NIR light (**7**).

Approximately, 80% A549 cell **Figure 3.7A** and 50% KB cells **Figure 3.7B** were viable after 48 h treatment of SWCNT-FA/DOX. However, 60% A549 cells and 40% KB cells were viable after 48 h treatment of NIR light exposed free SWCNT-FA/DOX. The A549 cell treated with the leachate of Silk@SWCNT-FA/DOX nanocomposite hydrogel without (**8**) and with (**9**) NIR light stimulation showed approximately 80% and 70% viability, respectively. The NIR light exposure caused DOX release due to which relatively higher toxicity was observed in (**9**) compared to (**8**). However, KB cells treatment with the leachate of Silk@SWCNT-FA/DOX nanocomposite hydrogel without NIR light stimulation (**8**) showed approximately 43%, 55%, 84% and 85% viability after 12 h, 36 h, 72 h and 120 h, respectively. This increase in cell viability with time might be due to the slow release of SWCNT-FA/DOX in the medium. However, NIR light exposure to Silk@SWCNT-FA/DOX nanocomposite hydrogel (**9**) showed approximately 20 to 30% cell viability at all the time points, which indicated NIR dependent SWCNT-FA/DOX release and its associated efficacy.

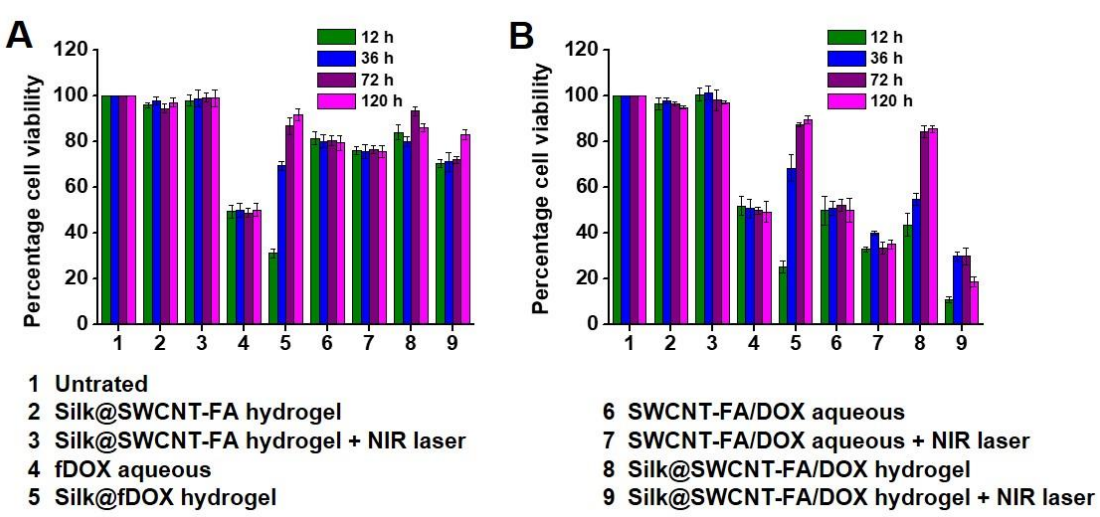

Figure 3.7. *In vitro bioactivity assessment of SWCNT-FA, SWCNT-FA/DOX, and DOX aqueous suspension and released leachate from silk hydrogel in cell culture medium with or without NIR light stimulation (indicated). The leachate was obtained after 12 h, 36 h, 72 h, and 120 h, and A549 (**A**) and KB (**B**) cells were treated for 48 h followed by MTT. The free form of FOX and SWCNT-FA/DOX was also used as a positive control for bioactivity assessment. All sample types are marked between **1** to **9** in the figure.*

.

3.4. Discussion

Several anticancer drugs have been discovered and approved by food and drug administration (FDA) to treat cancer. DOX is one of the potential cytotoxic antibiotics, which is frequently used for the treatment of a series of cancers. However, DOX, similar to other anticancer drugs, lack the ability to distinguish between normal and cancer cells; therefore, subsequent to the DOX therapy, cancer patients undergo several detrimental side effects. The continuous administration of DOX majorly causes a non-specific action, which includes thickening of the veins walls [223], cardiotoxicity, and depressed immune system, which makes the patient more susceptible to other microbial infection [223]. Nanotechnology has provided the platform for targeted delivery of these drugs with the enhanced anti-tumor activity and low side effects [198]. However, the systemic mode of delivery through the intravenous route distributes the drug carrier all over the body. In present work, we first fabricated FA functionalized SWCNT for DOX delivery to enhance its bioavailability for targeted cells in addition to attenuation of its side effects in the non-targeted cell. Later, we incorporated this SWCNT-FA/DOX to silk hydrogel for its localized intratumoral delivery to accumulate the drug at the desired site for a longer duration. During the process, we have also explored the SWCNT property to absorb the NIR light for on-demand drug delivery from Silk@SWCNT hybrid hydrogel.

The major challenge of using SWCNT for drug delivery applications is its even dispersion in an aqueous or organic solvent. SWCNT has a very high tendency to form aggregates. But pH of solvent, functionalization of SWCNT, and use of some detergent followed by physical treatment (sonication) are known to disperse the SWCNT [224]. Following this, we exposed the SWCNT to acid (H_2SO_4:HNO_3), which oxidized the SWCNT surface and form COOH-SWCNT. COOH functional group attachment then helps SWCNT to improve their biocompatibility [225, 226] and dispersion in aqueous buffer. PDI obtained through DLS presented in **Table 3.2** showed the stability of COOH-SWCNT in all the buffers. At higher pH (9.1) COOH-SWCNT lose their proton and carried a high negative surface charge. Due to the presence of higher negative surface charge SWCNT-COO^- tend to repel each other and therefore does not form the aggregation or precipitation. Size is one of the major factor responsible for cytotoxicity related to SWCNT. Few groups claim the greater toxicity of large CNT in contrary to that few reported small SWCNT are more toxic [226, 227]. However, large CNT were recommended for targeted drug delivery applications [212, 228]. COOH-SWCNT in

lower pH did not lose the proton and therefore carry less negative zeta potential and larger hydrodynamic radius. Further, due to mechanical treatment (sonication), SWCNT was broken, and therefore the hydrodynamic size of NH_2-SWCNT and SWCNT-FA reduced successively [229]. FETEM image **Figure 3.1A** again affirm the size and distribution of SWCNT into the buffer. The formation of SWCNT to SWCNT-FA/DOX was confirmed at each step using FTIR and UV-visible spectroscopy. Post-acid treatment recorded FTIR spectra have shown the characteristic COOH peaks in COOH-SWCNT. The COOH functional group is then used for the covalent attachment of other functional group as well as responsible for hydrophilicity of SWCNT. For covalent crosslinking, we have used one step EDC crosslinking. EDC Activates free COOH group and forms an unstable intermediate, which then replaces with a primary amine group to form covalent crosslinking [230]. Covalent attachment of primary amine functional group covered the COOH specific peak; however, NH_2 functional group characteristic peak was displayed in **Figure 3.1C**. Similarly, the free COOH group of FA was activated with EDC to crosslink with the free NH_2 group available on SWCNT surface. In UV-visible spectroscopy, we have seen FA characteristic peaks [219], which were not recorded in COOH-SWCNT but observed in SWCNT-FA **Figure 3.1B**. DOX λ_{max} observed in SWCNT-FA/DOX also confirmed the non-covalent adsorption of DOX onto SWCNT-FA/DOX.

The Advantage of using SWCNT is its high surface area and aspect ratio for the accommodation of a high amount of drug molecules. Zeta potential plays an important role in SWCNT to DOX interaction. The negative zeta potential of SWCNT-FA and positive zeta potential of cationic anticancer drug DOX along with molecular structure favors the electrostatic interaction and π-π interaction between DOX and SWCNT for the high loading efficiency [231]. SWCNT also has great potential to encapsulate DOX into its cavity [232]. Altogether high surface area, high aspect ratio, and favorable electrostatic interaction allowed us to obtain approximately three times the weight of DOX loading over SWCNT-FA in the ratio of 3:1 (w/w).

Silk is a protein-based natural biomaterial. SF protein isolated from BM and AA differs in their structure and function. SF reassembles itself from all aqueous alpha-helical structure to the hydrogel beta-sheet. However, due to structural variation, both the protein forms hydrogel with different strengths and takes a long time to gel. Various stresses such as sonication, vortex, temperature, pH, etc., accelerate the gelation of SF;

however, low mechanical strength and burst drug release limit their use. In present work, we have observed the quick gelation of SF by blending BM and AA in different ratios. Due to the differences in the hydrophobicity of both the proteins, blending caused the formation of hydrogel within 15 min **Figure 3.2**. The formation of hydrogel did not require any hazardous chemical or cross-linker, and the formed hydrogel is degradable **Figure 3.2A.** Both SF (BM and AA) individually did not form the hydrogel when exposed to the same strain and frequency parameter in the rheometer or visually **Figure A3.8)**. The degradability is dependent on the concentration and beta-sheet content of the hydrogel. The release of drug molecules entrapped into the gel is mostly degradation dependent. Therefore, the drug release from silk hydrogel can be tuned by varying concentrations of SF. We observed faster degradation of 1:2 hydrogel. This might be due to the presence of a high percentage of glutamic acid and aspartic acid in the protein sequence of AA silk compared to BM silk. AA silk contains 5.5% glutamic acid compared to 1% in BM silk [233]. The protease XIV enzyme used for degradation study specifically hydrolyzes the peptide bond on the carboxyl side of glutamic or aspartic acid and therefore cleave AA more than BM. The rheology data of formed hydrogel suggested its quick gelation, viscoelastic nature, and shear thinning property, which allows its easy injectability and structural recovery post-injection.

The silk hydrogel, however, presented inferior mechanical property and lack multiple functionalities. The addition of SWCNT to the silk hydrogel improved its mechanical strength as well as administered pH, thermal and photoresponsive properties to the gel. As it can be seen from **Figure 3.3A** the DOX release from SWCNT is pH and temperature-dependent [232]. In an acidic pH NH_2 group of DOX gets protonated, which increases the hydrophilicity of DOX and decreases the π-π interaction between DOX and SWCNT-FA, which favored its release. pH-dependent release of the anticancer drug is always desirable due to the slightly acidic environment of a tumor, which is a result of high metabolic activity and peripherally localized lysosome in a cancer cell [234]. In addition, FR -mediated uptake of SWCNT-FA/DOX fuses with the lysosome (pH 4 – 5.5), which further supports the DOX release into the cancer cell. Similarly, high temperature also weakens the hydrogen bonding and electrostatic interaction between SWCNT-FA and DOX to induce its release.

We have observed slow and sustained release of SWCNT-FA/DOX in hydrogel loaded system compared to a gel-free system. **Figure 3.3A** is a 100 h DOX release study

from free SWCNT-FA/DOX incubated in a combination of different pH buffer at various temperatures. However, **Figure 3.3C** is a 14 days study of DOX release from Silk@SWCNT-FA/DOX nanocomposite hydrogel. In the gel-free system **Figure 3.3A,** we observed 40% DOX release in 100 h in contrast to gel loaded system **Figure 3.3C**, where only 20% DOX got released after 14 days.

Furthermore, in **Figure 3.3D** we have compared DOX release from the gel-free SWCNT-FA/DOX, and gel loaded SWCNT-FA/DOX. We have conducted this experiment by exposing these systems to near-infrared (NIR) light at a predefined time interval. For this experiment, we have incubated both the formulation in pH 7.4 at 37 °C. These conditions have shown the least release of DOX, such as approximately 5% in gel-free system **Figure 3.3A** and approximately 7% in gel loaded system **Figure 3.3C**. However, due to NIR light stimulation, **Figure 3.3D** SWCNT get heated and released the drug intermittently to approximately 15% in 120 h. The gel loaded with fDOX in **Figure 3.3D** was also incubated under similar conditions and stimulated with NIR light at a similar time point; however, we did not observe the intermittent release here. In summary, we observed NIR light dependent on-demand release of DOX from Silk@SWCNT-FA/DOX nanocomposite hydrogel, which is due to the photo-thermal properties of SWCNT. Silk here provides biocompatibility and matrix to hold the same.

The degradation dependent drug (SWCNT-FA/DOX) release from silk hydrogel in the presence of a proteolytic enzyme is presented in **Figure 3.3B**. We observed 40% SWCNT-FA/DOX release **Figure 3.3B**, which is correlated to ~20% degradation of hydrogel **Figure 3.2A** in 14 days of study. This may be attributed to the high wt% loading of DOX to SWCNT-FA (3:1); hence, the amount of DOX release might also have an association with the degradation of hydrogel.

Cytotoxicity associated with exposure of SWCNTs to cells has always remained controversial [235]. The cytotoxic impact of SWCNT is independent of its cellular uptake [236]. Compared to pristine SWCNT, functionalized SWCNTs are non-cytotoxic even at high doses [225]. Due to the high loading efficiency of SWCNT (as discussed previously) and small LD50 of DOX we used SWCNT at a very low concentration (within the safe range) throughout our study. Our MTT data also indicated that SWCNT was not cytotoxic, and fDOX was highly toxic for both KB and A549 cells. The use of SWCNT-FA/DOX reduced the cytotoxic effects of DOX over A549 (FR^{-ve}) cells and

caused a targeted cytotoxic effect in KB (FR^{+ve}) cells. This result is in agreement with our DOX release data and specific uptake data. Due to high metabolic rate, cancer cells have slightly lower intracellular pH, therefore when SWCNT-FA/DOX is specifically up taken by KB cells, the DOX is released intracellularly for targeted cytotoxic effects. The bioavailability of the drug is also increased for targeted cells and decreased for non-targeted cells.

The cellular uptake of SWCNT by many cells has been shown previously [236]. In the present study, two cell lines KB and A549 [237] were chosen based on their presence and absence of FR, respectively. SWCNT-FA labeled with FITC were tracked only in FR^{+ve} KB cells. Blocking of FR through fFA also stopped SWCNT-FA uptake, which confirmed the entry of SWCNT-FA via receptors mediated endocytosis **Figure 3.5**. Studies revealed that the dimension of SWCNT determined the fate of its cellular uptake. The uptake of short CNT has been shown via energy independent diffusion mechanism, whereas large CNT was uptaken via energy-dependent endocytosis [228]. Our results support the previous findings for the specific uptake of FA-conjugated nanocarrier by the cells which overexpress FR. Silk fibroin [238], sericin [239] iron oxide [237], hollow silica [240], and several other nanoparticles have been conjugated to FA and exhibited specificity towards FR. DOX targeted delivery through SWCNT-FA into KB cells was further confirmed using fluorescence microscopy (**Figure 3.5**). In agreement with our MTT data, we found that both KB, and A549 cells were equally sensitive to fDOX. The quantitative estimation of fDOX uptake suggested that all the cells were loaded with fDOX within 72 h. However, due to the absence of FR, SWCNT-FA/DOX were not uptaken by these cells and only 30% of cells were loaded with DOX after 72 h of treatment.

Comprehensively, we have seen the gradual increase in the sub-G1 population of both A549 **Figure 3.4FI** and KB **Figure 3.4GI** cells post-treatment of fDOX, which shows that fDOX has identical cytotoxic effects on these two cells. The cell population of the sub-G1 phase is considered as apoptotic cell bodies [241]. DNA fragmentation is a prime characteristic feature of apoptosis. During the process of ethanol fixation, these fragments of DNA leaked out from the permeabilized cell membrane, and therefore population with reduced DNA content (sub-G1) appeared before the G1 phase [242]. However, the use of SWCNT-FA/DOX reduced the potential cytotoxic effects of DOX, especially for A549 cells (FR^{-ve}), and gradually caused the G2/M phase cell cycle arrest

in KB cells (FR^{+ve}) which subsequently lead these cells to death. In agreement to previously published reports, our data also support the DOX-induced increase in oxidative stress and ROS generation [243] to induce apoptosis [244].

The two major forms of cellular death are apoptosis and necrosis. DOX has been shown to induce both apoptosis [245] and necrosis [221] based on the cell type, amount of dose given, and the time of exposure. Real-time PCR analysis was used to assess the changes in the level of gene expression. Although, the expression level of FR on KB [246] and A549 [247] cell surface is well known. However, we have further checked for the FR expression level in both the cells using real-time PCR **Figure 3.6A**. Untreated (NT) KB cells had a significantly higher expression level of FR compared to untreated A549 cells. Cells were cultured prior to treatment with fDOX and SWCNT-FA/DOX into high glucose DMEM without FA, which further caused the enhance in the expression level of FR. Due to the absence of FA in the medium the requirement of FA by KB cells increased which resulted into FR over expression. SWCNT-FA/DOX treatment further significantly increased the FR expression in KB cells compared to fDOX treatment which may be due to the presence of FA in SWCNT-FA/DOX.

The decreased level of Bcl-2 and increased level of Bax is an indicator of apoptotic induction [248]. The expression level of anti-apoptotic gene Bcl-2 was decreased significantly in KB **Figure 3.6B** cells when exposed to SWCNT-FA/DOX; however, the expression level of pro-apoptotic gene Bax **Figure 3.6C** was significantly increased. SWCNT-FA/DOX is targeted to KB cells; therefore, DOX is available enough to induce an increase in Bax expression level. In contrast, due to less and discontinuous supply of DOX to A549 cells treated with SWCNT-FA/DOX Bax expression level lowered. Similar to previously published reports, we also found the fDOX induced increase in the expression level of Bax [244]. However, we did not see the change in the Bcl-2 expression level in either KB or A549 cells.

The pro-apoptotic Bax forms the channel in the mitochondrial membrane for cytochrome c (Cyt-c) release from mitochondria to cytosol; however, Bcl-2 inhibits the formation of these channels. The low expression level of Bcl-2 and high level of Bax, therefore, favour the Cyt-c release, which is an indicator of apoptosis. Similar to Bax expression level, Cyt-c expression level was also high for both A549 and KB cells, but

this expression level was reduced for A549 cells in the presence of SWCNT-FA/DOX due to less availability of DOX **Figure 3.6D**.

Apoptotic protease activating factor 1(Apaf-1) is a pro-apoptotic protein like a Bax. Apaf-1 binds to Cyt-c and procaspase-9 to form the apoptosome complex, which then activates and recruits other cell killing caspases [249]. DOX treatment to KB cells causes an increase in Apaf-1 transcript level [250]. However, the opposite effect was observed for A549 cells **Figure 3.6E**, but similar to Bax transcript level downregulation indicated the anti-apoptotic activity, i.e., A549 cells were recovering and not going into apoptosis [251]. This may be due to the discontinuous supply of DOX into A549 cells in contrast to KB cells, which receive a continuous supply of intracellular pH-responsive slow and sustained release of DOX from SWCNT-FA/DOX.

The two apoptotic pathway intrinsic and extrinsic is known for the induction of apoptosis [252]. Caspases belong to cysteine protease family and divided into initiator (caspase-8 and caspase-9) and effector (caspase-3 and caspase-7) caspases. Caspase-8 and caspase-9 are activated via the extrinsic and intrinsic pathways, respectively [248]. We have seen in our results that caspase-8 was activated in both KB and A549 cells after fDOX treatment. However, its expression level remained normal with the treatment of SWCNT-FA/DOX **Figure 3.6F**. This confirmed that fDOX also follow the extrinsic pathway to induce apoptosis which was not the same for SWCNT-FA/DOX. The reason behind this may be the reduced potential cytotoxic effects of DOX in conjugated form. Because fDOX specifically induced extrinsic apoptotic pathway in both KB and A549 cells, due to conjugated form, SWCNT-FA/DOX did not show the same response.

The extrinsic pathway initiate when the death ligand bind to the death receptor (Fas Receptor). Fas receptor then recruit initiator caspase-8 mediated pathway as discussed above [253]. The fDOX induced Fas receptor expression is regulated by p53 and leads to apoptosis. Evidence suggested that Fas receptor gene promoter activates by p53, which accumulated due to DOX treatment [254]. In our observation, we have seen the increased expression level of Fas receptor in both KB, and A549 cells post fDOX treatment, which indicates the fDOX mediated extrinsic pathway (**Figure 3.6G**). In contrast, SWCNT-FA/DOX did not change Fas receptor expression level in KB cell and did not follow the extrinsic apoptotic pathway.

p53 is a tumor suppressor protein. Several reports suggested that DOX-induced apoptosis is mediated through p53 dependent pathway [254-256]. Similarly, we have observed the increased expression level of p53 in both KB and A549 cells treated with fDOX **Figure 3.6H**. However, Only in KB cells and not in A549 cells, SWCNT-FA/DOX caused the increase in the expression level of p53, which again confirmed the targeted delivery of DOX into FR^{+ve} KB cells.

Free SWCNT-FA also showed the biocompatibility in Figure 4(IA) similar to its leachate form in **Figure 3.7A & B**. The biocompatibility of SWCNT was always questionable; however, its amalgamation with silk made it a more biocompatible nanocomposite material. Cell viability data **(Figure 3.7)** correlated with release data **(Figure 3.3)**, indicated initial high cytotoxicity in 12 h leachate due to burst release of DOX (**5**) followed by slow DOX release and increase in cell viability. We further found that both A549 and KB cells were equally sensitive to fDOX and its leachate form. Due to NIR light exposure to Silk@SWCNT-FA/DOX nanocomposite hydrogel (**9**), some DOX also released into the medium, which caused 20% higher toxicity into both A549 and KB cells than non-NIR, stimulated (**8**). This also indicated that KB cells (FR^{+ve}) showed more cytotoxicity compared to A549 cells (FR-ve) towards SWCNT-FA/DOX released from hydrogel and also confirmed its similar functional bioactivity.

The goal of localized anticancer drug delivery is to accumulate the drug at the tumor site and enable its targeted delivery to reduce the unwanted toxic side effects. **Figure 3.8** represents an overall approach for the same. Injectable nanocomposite silk hydrogel was prepared by blending SWCNT-FA/DOX with BM and AA silk fibroin protein. The silk hydrogel act here as a depot for an anticancer drug. SWCNT-FA/DOX makes the gel responsive to external stimuli such as NIR light. Low pH of tumor environment and NIR light stimulation induce the release of SWCNT-FA/DOX, which is endocytosed by FR^{+ve} cancer cells to induce the apoptosis pathway.

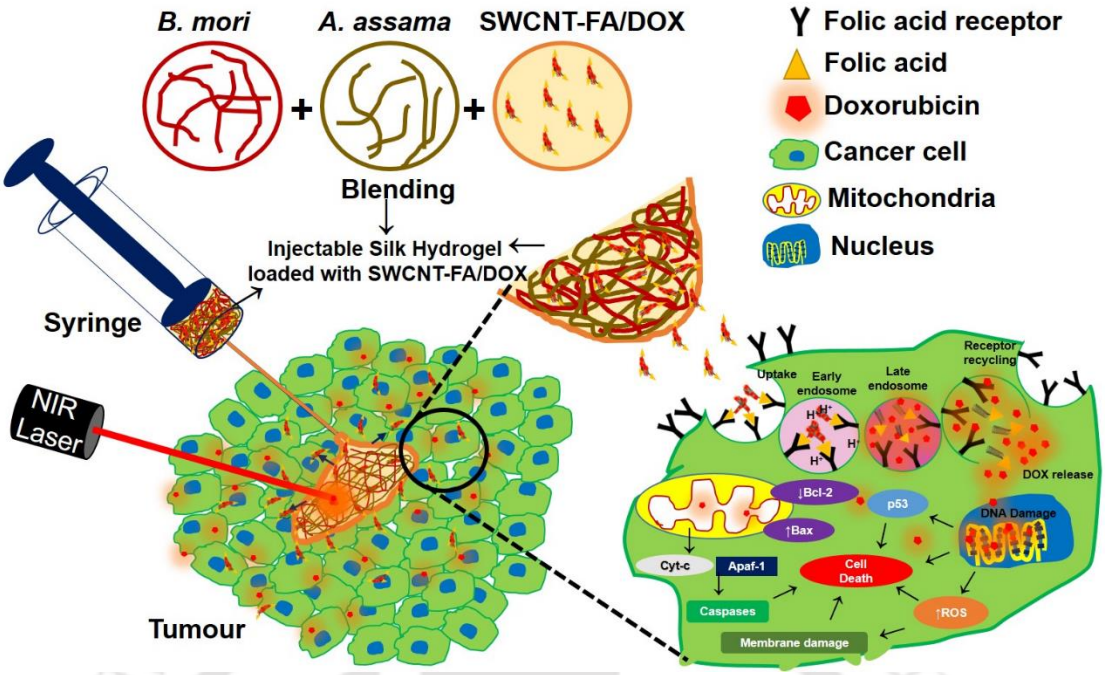

Figure 3.8. *Illustration of an overall approach for anticancer drug delivery.*

3.5. Significant findings

The salient findings of this chapter are as follow –

1. The SWCNT was successfully modified with FA and loaded with a high dose of anticancer drug DOX to form SWCNT-FA/DOX. Further, this nano-drug carrier was embedded in silk hydrogel to develop Silk@SWCNT-FA/DOX nanocomposite hydrogel.
2. The folic acid receptor target cell-specific cytotoxicity was conferred due to SWCNT-FA modification.
3. The combination of low pH and high-temperature favors the triggering of DOX release from the nanocomposite hydrogel.
4. Innately, silk hydrogel is non-responsive to temperature and NIR laser. However, due to the SWCNT incorporation, multifunctional properties were achieved in the nanocomposite silk hydrogel.
5. The intermittent exposure to NIR light has enabled the on-demand release of functionally bioactive DOX molecules.

Overall, the present approach demonstrated the silk-based on-demand external stimuli dependent drug delivery platform for cancer treatment.

Chapter 4

Assessment of Photo Electro-Active Minimally Invasive Injectable Silk Hydrogel in *In Vivo* Breast Tumor Mice Model for Spatiotemporal Controlled Release and Tumor Therapy

This chapter is a follow up *in vivo* functional study of our formulation that is developed in ***Chapter 3***. *The hydrogel was injected locally near to the mice breast tumor and the drug release was triggered on-demand from externally applied NIR laser and electric field.*

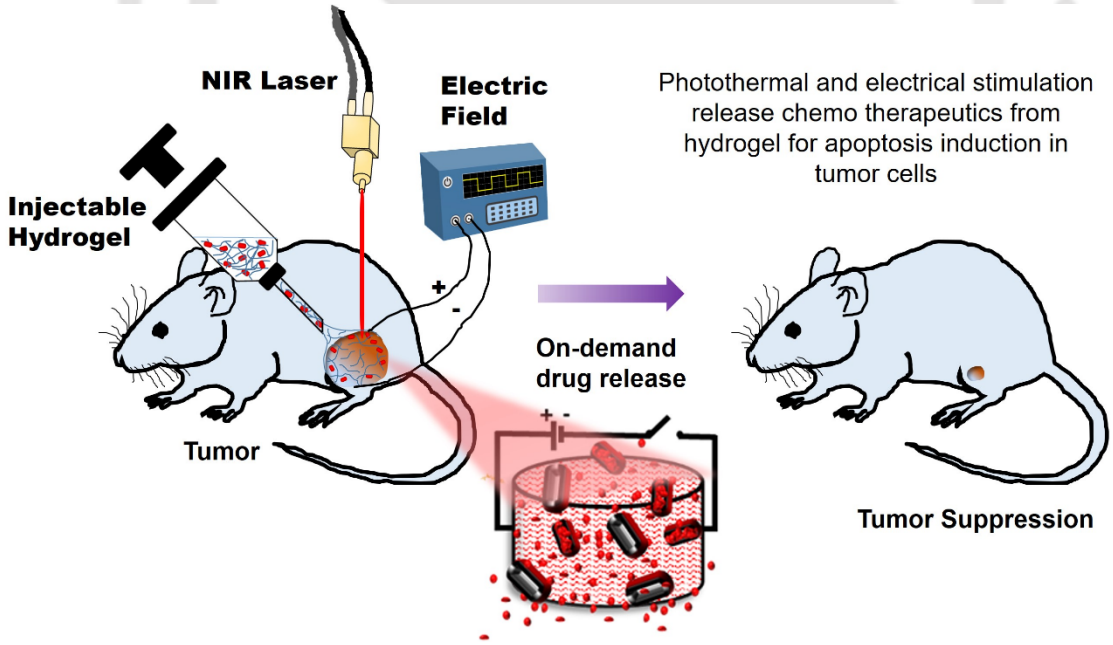

The work embodied in this chapter is published in a peer-reviewed journal as follow: **Ankit Gangrade**, Basveshwar Gawali, Jadi Praveen Kumar, VGM Naidu and Biman B. Mandal. "Photo-Electro Active Nanocomposite Silk Hydrogel for Spatiotemporal Controlled Release of Chemotherapeutics: An *In Vivo* Approach toward Suppressing Solid Tumor Growth." ***ACS Applied Materials & Interfaces*** 12, 2020, 27905-27916.

ABSTRACT

Conventional systemic chemotherapeutic regimens suffer from challenges such as non-specificity, shorter half-life, clearance of drugs and dose-limiting toxicity. Localized delivery of chemotherapeutic drugs through non-invasive spatiotemporally controllable stimuli-responsive drug delivery systems could overcome these drawbacks while utilizing drugs approved for cancer treatment. In this regard, we developed photo-electro active nanocomposite silk-based drug delivery systems (DDS) exhibiting, on-demand drug release *in vivo*. A functionally modified single-walled carbon nanotube loaded with doxorubicin was embedded within cross-linker free silk hydrogel. The resultant nanocomposite silk hydrogel showed electrical field responsiveness and near-infrared (NIR) laser-induced hyperthermal effect. The remote application of these stimuli in tandem or independent manner led to the increased thermal and electrical conductivity of nanocomposite hydrogel, which effectively triggered the intermittent on-demand drug release. In a proof-of-concept *in vivo* tumor regression study, the nanocomposite hydrogel was administered in a minimally invasive way at the periphery of the tumor by covering most of it. During the 21-day study, drastic tumor regression was recorded upon regular stimulation of nanocomposite hydrogel with simultaneous or individual external application of an electric field and NIR laser. Tumor cell death marker expression analysis uncovered the induction of apoptosis in tumor cells leading to its shrinkage. Heart ultrasound and histology revealed no cardiotoxicity associated with localized DOX treatment. To our knowledge, this is also the first report to show the simultaneous application of electric field and NIR laser *in vivo* for localized tumor therapy, and our results suggested that such strategy might have high clinical translational potential.

4.1. Introduction

Cancer is a group of diseases that have been recognized as the major *causes* of deaths all around the globe, of which solid tumors contribute significantly.[5] Chemotherapy is the first line of cancer treatment in which conventionally anticancer drugs are infused in the veins with the aim to reach and accumulate into the tumor for its growth inhibition and regression. However, the hypoxic presence, limited diffusion constraints and complex microenvironment of solid tumor obstruct drug penetration at its cytotoxic concentration that results into quiescence drug resistance development rather than just treatment failure.[257] Additionally, the systemic distribution of toxic drug molecules is also associated with healthy tissue toxicity and off-target accumulation, contributing to poor therapeutic efficacy.[258] This has prompted researchers to develop new delivery materials and alternative administration routes for the advancement of the current chemotherapeutic strategy.[153, 259-261] The concept of 'localized drug delivery' has gained momentum recently, for the treatment of chronic diseases such as cancer, which requires long term interaction with therapeutic molecules for its desired action and effects.[262, 263] Local drug administration through some kind of depot is therefore expected to keep its effects in the vicinity of diseased areas. 'Hydrogels' due to their soft injectable nature are preferred to be used as a depot for local drug delivery, which allows their implantation directly at the solid tumor site without a major surgery.[48, 264] The precise delivery of therapeutic molecules to the solid tumor site improves its therapeutic effect and reduces its biodistribution to the healthy tissues, thereby minimizing its toxic side effects.[48] However, it still remains a challenging task to control the release kinetics of biomolecules from the hydrogel. The large pore size and high water content of hydrogels often promote the release of the entrapped biomolecules rapidly. Due to such burst release behavior, the bioavailability of drug molecules at the local site remains for a short duration, which is usually not enough to suppress the cancer. Therefore, to enhance the efficacy of chemotherapy, we need a drug delivery system (DDS) which can release its content in a sustained way for a longer duration. However, conventional hydrogels lack multifunctionality in terms of responsiveness towards the surrounding environment, which further eliminates any control over the therapeutics release kinetics limiting their practical application.

Stimuli-responsive "smart biomaterials" are capable of overcoming the hurdles of conventional biomaterials described above, and therefore they are evolving as the most

promising materials for different biomedical applications, including drug delivery.[53, 260, 264, 265] The hydrogel system designed by stimuli-responsive biomaterials could sense the specific cues in their surrounding environment and trigger the changes in their internal equilibrium, which further drive the drug release and yield on-demand therapeutic effects. Stimuli to which the system reacts could be intrinsic, extrinsic, or the combination of both. The materials that respond precisely to the endogenous stimulus such as pH,[55, 104, 194] temperature,[55] enzyme,[55, 266] redox conditions,[267] hypoxia,[268] providing the intrinsic cues to trigger the drug release. These intrinsic cues are generally the characteristics of a specific tissue, for example, an acidic condition in the stomach, or a particular disease such as low pH, and reductive microenvironment of the tumor. In contrast, materials which respond to the exogenous stimulus that are typically absent in the living system include magnetic field,[269] electric field,[260] sound,[270] and light[55] providing the extrinsic cues to drive the drug release. Such extrinsic cues can, therefore, be used to remotely stimulate the material from outside in four dimensions with spatial and temporal control. The combined effects of these external cues could further fine-tune the drug release, however, in this regard, very few attempts have been made by researchers with *in vivo* applications. For example, Deng, Lin, et al. (2016), has showed synergic effects of magnetic field and NIR laser for tumor regression [271]. Taking cues from these early iterations of stimuli-responsive DDS, we take forward this notion to design a composite material that is responsive to multiple stimuli.

The present work is a follow-up *in vivo* study of our previously published work,[55] wherein we have prepared and characterized a multi-stimuli-responsive nanocomposite silk hydrogel system. The single-walled carbon nanotube (SWCNT) decorated with folic acid (FA) and loaded with anticancer drug doxorubicin (DOX) abbreviated as SWCNT-FA/DOX, served as a drug reservoir for pH, temperature, and near-infrared (NIR) laser triggered release. In contrast to biological tissue, the SWCNTs have been reported for their strong absorption in NIR region.[55, 272] Additionally, NIR laser penetrates deep into the tissue and provides non-invasive high spatiotemporal regulation.[153, 259, 264] Therefore SWCNTs have been widely studied alone or in combinations with various polymers for NIR laser-induced photothermal, photodynamic cancer chemotherapy as well as in photoimaging applications.[113, 144, 273, 274] The application of electric field responsive DDS *in vivo* was first demonstrated by Ge, Jun,

et al. (2011), wherein, they have suspended polypyrrole derived electrically conductive nanoparticles into a thermosensitive hydrogel for electric field triggered drug release.[260] Nevertheless, CNTs are also a good conductor of electric current and have been reported as an electro responsive polymeric (not silk) implants for pulsatile drug delivery *in vivo* by Servant, Ania, *et al.* (2013), but not for tumor therapy.[215]

We incorporated these SWCNT-FA/DOX into the blend of two different varieties (mulberry and non-mulberry) of silk fibroin protein to form crosslinker free nanocomposite silk hydrogel abbreviated as Silk@SWCNT-FA/DOX hydrogel. With our pilot in vitro study,[55], we showed that silk fibroin polymer, which is nonresponsive to extrinsic cues, exhibited NIR laser-responsive on-demand therapeutic releasing behavior post addition of SWCNT cargo. These results motivated us to further assess the photothermal and electroconductive activity of Silk@SWCNT-FA/DOX nanocomposite hydrogel *in vivo* to suppress tumor growth. Due to viscoelastic property, this hydrogel could be implanted through a syringe in a minimally invasive way directly at the tumor site. The application of 808 nm NIR laser or a small electric field or both in combination induce the release of the drug from the SWCNT-FA reservoir and diffuse to the local tumor. To our knowledge, this is also the first *in vivo* report to show the combined effect of the NIR laser and electric field for cancer chemotherapy in DDS application.

4.2. Materials and methods

4.2.1. Silk@SWCNT-FA/DOX nanocomposite hydrogel preparation

The preparation and detailed characterization of Silk@SWCNT-FA/DOX nanocomposite hydrogel were done as described in our previous study.[55] In brief, the SWCNT was EDC crosslinked with folic acid to form SWCNT-FA. Later three-part DOX was loaded on 1 part SWCNT-FA (3:1; w/w) to form SWCNT-FA/DOX. The DOX was mixed with SWCNT-FA in a pH 9.1 buffer at room temperature on rotospin overnight. The DOX adsorption on the SWCNT-FA surface/cavity was majorly due to π- π stacking and electrostatic interactions. The physical characterization was done using fourier transform infrared spectroscopy (FTIR), field emission transmission electron microscopy (FETEM), field emission scanning electron microscopy (FESEM), and UV-visible spectroscopy at each step of preparation. Silk hydrogel was prepared by blending two different varieties of silk fibroin protein, which was isolated from different sources, *i.e.* mulberry *Bombyx mori* silkworm cocoon and non-mulberry *Antheraea assama* silkworm gland. 1 mg/ml SWCNT-FA/DOX was mixed into these two silk fibroin proteins, which were blended at 1:1 wt% ratio. The blend was initially a solution which at 37 ^{o}C undergoes sol-gel transition resulting into Silk@SWCNT-FA/DOX nanocomposite hydrogel. The nanocomposite hydrogel was rheologically characterized well, and these data have been reported previously [55].

4.2.2. Electrical conductivity test of Silk@SWCNT-FA/DOX nanocomposite hydrogel

The current-voltage (I-V) characteristics of the silk hydrogel and Silk@SWCNT-FA were recorded using a two probe *I-V* measurement set up using Keithley 2450 source meter. *I-V* measurements were performed by applying a DC voltage sweep from 0 to ±10 V, and measuring the resulting current (n=3). All the *I-V* measurements were carried out at room temperature (~300K). The surface resistance R is determined from the inverse of the slope of the I-V characteristics.[275]

4.2.3. Recording of electric field triggered DOX release

A 100 µl Silk@SWCNT-FA/DOX nanocomposite hydrogel and silk hydrogel, both containing 100 µg DOX, were placed in PBS (pH 7.4) flanked by two platinum wires.

For the release study, a pulse voltage of 1 V at 1 MHz frequency was applied over these hydrogels through a functional generator (Tektronix AFG1022). The hydrogels were stimulated for five times at predecided time points in a 21 days release study. The PBS was collected and replaced with fresh PBS every time to determine the DOX concentration using a fluorescence standard plot as done previously.[55]

4.2.4. Recording of NIR laser-induced hyperthermia effect

The Silk@SWCNT-FA nanocomposite hydrogel or silk hydrogel was exposed to 0.5 W output power, focusable 808 nm NIR laser for long 20 min and short 5 min ON/OFF cycle. A digital thermal probe was placed in these hydrogels to record the temperature. The change in temperature (δT) was calculated by subtracting the final temperature from the initial temperature. The FTIR spectra at the frequency range from 400 to 4000 cm^{-1} were recorded for the hydrogels before and after NIR laser exposure. The amide I peak from 1600 to 1700 cm^{-1} was then deconvoluted to determine any significant change in secondary structure. The NIR laser-induced drug release from the nanocomposite hydrogel has also been reported previously.[55]

4.2.5. *In vivo* tumor studies

The animal studies were conducted through the standard procedure with the approval of the Institutional Animal Ethics Committee of NIPER Guwahati (NIPS/NIPER/PC/2018-03-09). 6-8 weeks old female BALB/c mice with an average of 20-25 g body weight were acquired from Palamour biosciences, Hyderabad, India. Temperature (24 ± 1°C), humidity (55 ± 5%) and light/dark cycle (12-hour) of the animal house were maintained throughout the study. Free access to food and water was allowed. The animals were acclimatized for at least 14 days before the initiation of the experiment and were observed for any sign of disease.

Mice breast cancer (4T1) cell line was cultured in RPMI media containing 10% FBS and 1% antibiotic. To develop a tumor, female BALB/c mice were subcutaneously injected with a specific number of 4T1 cells directly into the 4^{th} mammary fat pad. Tumor growth was measured using the Small Animal Imaging system, Fujifilm Visual Sonics, Singapore Model: Vevo LAZR X 3100. The isoflurane at 4% was used to induce the anesthesia in the animals and was maintained at 2% during the procedure. Postanesthesia, the animal, was placed over the animal platform. Essential parameters like

electrocardiogram (ECG), respiration rate, body temperature, and heart rate were recorded throughout the imaging. *The MX400 ultrasound transducer used was with abdominal kidney as preset.* The data was recorded *for each animal in B-mode (Brightness) and 3D mode on day 0, day 7, day 14, and day 21*. The ultrasound 3D video *data from the imaging system* (Vevo LAZR X 3100) was then imported in the dedicated Vevo lab 3.1.1 software for analysis. The software created the digital slices of 0.1 mm step size from the 3D video of the tumor. On each slice, the tumor area was marked manually, and the software then calculated the final 3D tumor volume (mm^3) on finishing the task. Further, the relative change in tumor volume from day 0 was then calculated by subtracting the final day (0, 7, 14, 21 day) tumor volume to initial day 0 tumor volume and divided by initial day 0 tumor volume. Further, the relative change in tumor volume was plotted against time.

The treatment was started when the tumor size reached 100 mm^3. The tumor-bearing mice were segregated into seven groups with n=4 in each group. Animals of the group (1) were untreated, (2) were treated with free DOX (fDOX), (3) were treated with Silk@DOX hydrogel, and (4) to (7) were treated with Silk@SWCNT-FA/DOX. On the treatment day, animals of the group (2) were administered intraperitoneally with fDOX, whereas animals of the group (3) to (7) were locally (near tumor) administered with above-said hydrogels. For the treatment, three injections of 50 µl hydrogel, each containing 50 µg DOX (from group 3 to 7), were introduced at all around the periphery of the tumor. Group (2) was treated with equivalent 150 µg fDOX (~6 mg/kg body weight) intraperitoneally. Group (3) and (4) did not receive any external stimulation; however, group (5), (6), and (7) were externally stimulated every alternate day from the second day of treatment. For external stimulation the animals were anesthetized with isoflurane as mentioned previously. The locally implanted hydrogels of animals of the group (5) were irradiated with NIR laser at 808 nm (0.2 W/cm^2) for 5 min. Similarly, an electric field of 1 V, 1 MHz was applied onto the tumor area of group (6) animals for 5 min. For electric field stimulation the tumor area, where the nanocomposite hydrogel implanted, was completely covered with generous amount of conductive gel. Both electrode tips were placed at certain distance in direct contact with conductive gel and electric pulse was applied through DC power source (Tektronix AFG1022). Group (7) animals, however, have received both NIR laser and electric field stimulation together for 5 min. Every seventh day the tumor volume and body weight was recorded. Animals

were euthanized on 21st day, and tumor, heart, liver, kidney, and spleen were collected and immediately frozen in liquid N_2 until further analysis. Tumors of all the animals were weighed and plotted accordingly. The scheme of the study and external NIR laser and electric field adjustment is presented in **Figure A4.1**.

4.2.6. Histology

For histology, 10 µm thick slices of tumor, heart, liver, kidney, and spleen were sectioned using cryo microtome (Leica CM 1860 UV). Sections were fixed with chilled acetone for 10 min and air-dried overnight. Hematoxylin and eosin (H & E) staining was performed as previously described.[95] The images were captured using a bright-field microscope (Evos life technology, USA) and compared in each group.

4.2.7. TUNEL assay

Terminal deoxynucleotidyl transferase-mediated dUTP nick-end labeling (TUNEL) HRP-DAB assay kit (ab206386) was procured from Abcam, USA. The test was performed on the cryosectioned slides as per the manufacturer protocol, and images were captured using a bright-field microscope (Evos life technology, USA).

4.2.8. Western blot assay

Tumor tissue was chopped in small pieces and lysed with RIPA lysis buffer as previously done.[276] In brief, lysed tumor tissue was centrifuged, and protein was collected in a fresh eppendorf tube. Protein concentration was determined using Bradford assay (Sigma USA). Approximately 30 µg protein was loaded in sodium dodecyl sulfate polyacrylamide gel electrophoresis (SDS PAGE). The protein was transferred to Immobilon-P PVDF membrane (Merck Millipore, USA) using western blot apparatus (Biorad). Blots were blocked with 5% bovine serum albumin (BSA) followed by primary test/housekeeping antibody incubation. β-Actin was used as a housekeeping antibody against anti-Bax, anti-Bcl 2, anti-Caspase 3, anti-Caspase 8, anti-Caspase 12, anti-Caspase 9, and anti-PARP test antibodies. The blots were developed by the ECL kit (Biorad, USA), and images were captured using Biorad ChemiDoc digital imager. The band intensity was calculated using ImageJ software. First, the band intensity of the test protein was normalized to the band intensity of the housekeeping protein. Subsequently,

the normalized values of treated groups were further normalized with the untreated group to determine the relative up/down-regulation of the test protein.

4.2.9. Echocardiography of heart

To assess the cardiac function, Visual Sonics Vevo Laser X 3100 system was used. Mice were anesthetized as for the ECG measurements and positioned supine on a heated surface (37 °C) to maintain stable body temperature during the experiment. Echocardiography was performed with a 1-cm gel standoff in a left lateral position. A linear transducer in 13-MHz mode was used to obtain high-resolution B mode and M-mode measurements. The echo images were digitized from videotape and measurements performed using a digital image analysis package (VevoLab). Cardiac output, fractional shortening, ejection fraction were calculated from B mode whereas LV mass, systolic volume, diastolic volume, LV wall thickness, LV mass corrected, left ventricular posterior wall thickness systoli (LVAW;s), LVAW;d (diastolic), left ventricular posterior wall thickness systolic (LVPW:s), LVPW:d (diastolic) were measured for each animal from the M-mode image.

4.2.10. Statistical Analysis

All the statistics were performed using OriginPro 8.5 software. The raw data of experimental replicates were used to perform the one-way analysis of variance (ANOVA) test by selecting the Turkeys method at a different significance level. In the figure legend where the test was performed, the level of significance was indicated as *P < X, where X is the value of significance level at which data showed a significant difference.

4.3. Results

4.3.1. Electric field conductivity of Silk@SWCNT-FA/DOX hydrogel triggers the drug release

The room temperature current-voltage (I-V) characteristics of the silk hydrogel and Silk@SWCNT-FA are shown in **Figure 4.1A**. The data recorded for Silk@SWCNT-FA (solid line) in the voltage range -10 V to +10 V depicts non-linear behavior showing quite symmetric upon reversal of the voltage direction indicating possible Ohmic conduction and space charge limited conduction (SPLC). The pure silk hydrogel did not show any current with the change in voltage, indicating its electrically non-conducting behavior due to the absence of SWCNT. The surface resistance of Silk@SWCNT-FA was determined to be 18.1 ± 8 KΩ. The results demonstrated the electroactivity of Silk@SWCNT-FA, which makes it a suitable candidate/carrier for electrically stimulated drug release application.

The electric field triggered drug release capabilities of the Silk@SWCNT-FA/DOX, and Silk@fDOX hydrogel was investigated for 24 days. These hydrogels were placed in PBS pH 7.4, and a voltage of 1 V was applied through the platinum wire for 5 min immediately at 30th min of incubation **(Figure 4.1B)**. This first (1) stimulation triggered approximately 3% and 0.5% of initially loaded DOX release into PBS from Silk@SWCNT-FA/DOX and Silk@fDOX hydrogels, respectively. The PBS was replaced with fresh solution every time. The cumulative DOX release was continuously recorded in stimulation off cycle until the drug release saturated/slowed. The saturation reached in 5 h with a 16% release recorded from Silk@SWCNT-FA/DOX as compared to only 3.4% from Silk@fDOX. The second (2) stimulation was applied in the fifth hour, and the DOX release concentration until the saturation, which was recorded at 10th h. In this five hour interval time, the cumulative release reached 32% and 7% for their respective hydrogels, which is specifically double in a given interval of time, as described above. The third (3) stimulation was given at 10th h, and the DOX release was measured until 30th h. In this 20 h interval, only 11% and 3% DOX was released with a cumulative of 43% and 10%, respectively. The release rate at third stimulation was low as compared to the first and second stimulation that may be due to the initial high payload of our nanocarrier. At third (3) stimulation the Silk@SWCNT-FA/DOX depot was already emptied 32%, containing only 68% of initially loaded drug to release further. The release

study was continued for 21 days, with a total five times voltage application, which induced approximately 75% and 22% DOX release from Silk@SWCNT-FA/DOX and Silk@fDOX hydrogels, respectively **(Figure 4.1C).** This significant difference in the amount of drug release indicated that the electrically conductive Silk@SWCNT-FA/DOX hydrogel has superior properties over Silk@fDOX hydrogels. This also represents that the on command drug release from Silk@SWCNT-FA/DOX hydrogel could be roughly controlled by the strength/duration of the electric field and initial drug payload of hydrogels.

To explain the electric field triggered drug release from conductive Silk@SWCNT-FA/DOX nanocomposite hydrogel, we proposed a theory as represented in **Figure 4.1D** based on our results. A single 5 min electric field stimulation is found to be capable of releasing drugs for more than 5 h. The hydrogels were placed in a PBS solution, which is composed of ions. Also, the cationic drug DOX and anionic nanocarrier SWCNT-FA are bounded by electrostatic interaction.[55] On the application of the electric field, The charged ions in the environment move forcibly in and against the direction of the current. The electrically conductive SWCNT might also try to align itself in the course of flow by actuation process. Together SWCNT actuation and ions movement in the hydrogel matrix are enough to create the pores in it, which further permits the incubation buffer solvent to access the DOX for its consistent release even after the removal of the electric field.

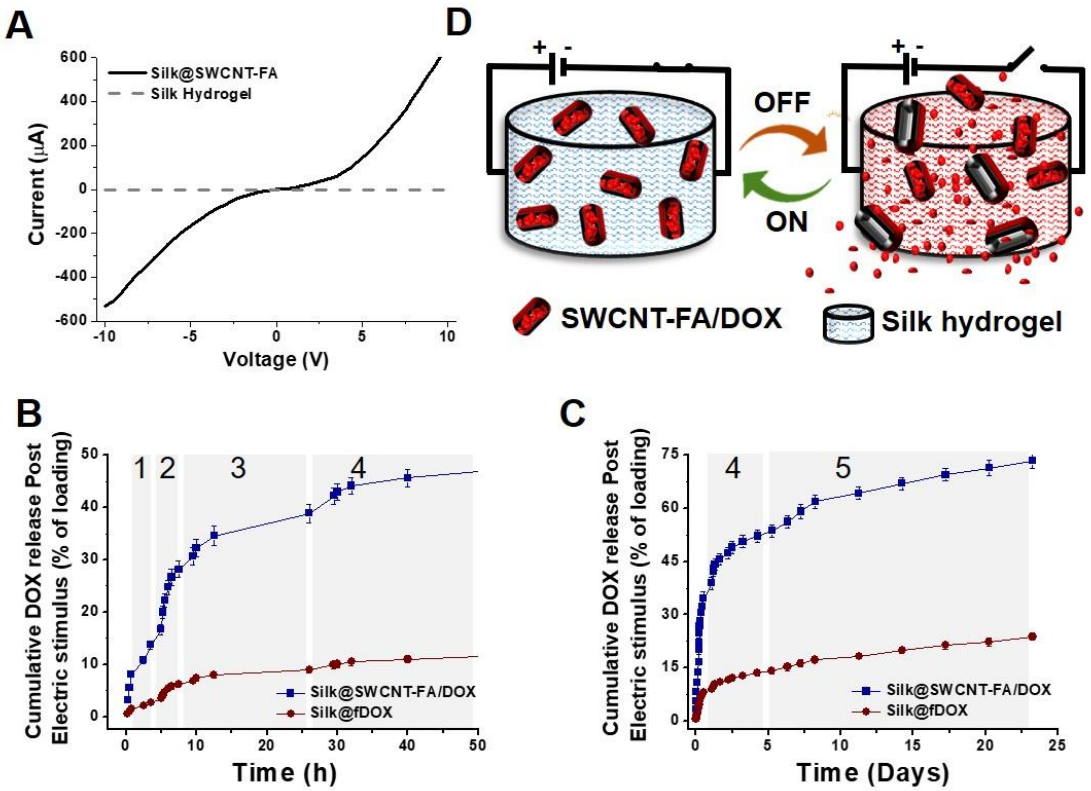

Figure 4.1. ***(A)*** *Current-voltage characteristic plot of Silk@SWCNT-FA and silk hydrogels.* ***(B, C)*** *Short term (50 h) and long term (24 days) on command drug release data from Silk@SWCNT-FA/DOX and Silk@fDOX with a total of five electric field stimulation, where 1,2, 3, 4 and 5 indicate the stimulation intervals (as mentioned in the results section).* ***(D)*** *A graphical representation is indicating 5 min turn ON cycle as a stimulator of drug release for long term off cycle.*

4.3.2. *NIR laser induces hyperthermia in* Silk*@SWCNT-FA hydrogel and triggers the drug release*

The photothermal performance of Silk@SWCNT-FA hydrogel was investigated by exposing it to NIR laser of 0.5 W output power and 808 nm wavelength as previously done.[55] On exposure, the hydrogel gets heated rapidly, and approximately 7 ^{o}C temperature rise was recorded in the first 5 min. However, we continued to expose the hydrogel with the NIR laser for 20 min to record the saturation point and maximum temperature (T_{max}). We found that in the rest 15 min of exposure, only 4 ^{o}C temperature was increased, showing an overall increase of approximately 10 ^{o}C upon irradiation for 20 min. A rapid drop in hydrogel temperature was observed immediately after turning off the NIR laser, and in 20 min, it had cooled down to its original initial temperature **(Figure 4.2A)**. From here, we concluded that Silk@SWCNT-FA hydrogel responds very

quickly to NIR laser, and no further significant rise in temperature was observed after 5 min exposure. Based on this, NIR laser was turned on and off every 5 min in a series of 5 cycles and the change in temperature was recorded **(Figure 4.2B)**. In each cycle, we recorded 6 to 7 ^{o}C rise in temperature from its initial temperature. The 5 min cooling phase of each cycle from 1st to 3rd cycle added 1 ^{o}C as the initial base temperature for the next cycle. However, this rise got saturated after 3rd cycle. Therefore, we observed a maximum of 10 ^{o}C rise in temperature after the 5th cycle, similar to a single 20 min cycle.

Here, we show the effect of NIR irradiation on silk hydrogels. 300 µl of Silk@SWCNT-FA and silk hydrogels without SWCNT-FA were exposed to NIR laser from the top, set up at a distance of ~10 cm. The representative images of these respective hydrogels are presented in **Figure 4.2C** and **Figure 4.2D**. The Silk@SWCNT-FA hydrogel drastically shrunk in 40 min. However, silk hydrogel without SWCNT-FA did not respond to NIR laser after getting exposed for the same period. The FTIR spectra were recorded for both the hydrogels before and after 40 min exposure of NIR laser **(Figure A4.2 A)**. A broad peak of water at 3200-3300 cm^{-1} was observed in both silk and Silk@SWCNT-FA hydrogels before the NIR laser exposure. The water characteristic peak was still present in silk hydrogel; however, it was absent in Silk@SWCNT-FA hydrogel after the NIR laser exposure. The water content of this hydrogel was 98%, and it all dried up in 40 min NIR laser exposure. This indicates that Silk@SWCNT-FA hydrogel could produce enough heat, which may evaporate the water from hydrogel and cause its shrinkage. Also, the generated heat is sufficiently high to ablate the local deadly cancer cells through the photothermal effect. The NIR laser has also induced changes in the secondary structure of silk, which is calculated by the deconvolution of amide I peak from 1600 to 1700 cm^{-1}, as represented in **Figure 4.2E** and **Figure A4.2 B**. The silk hydrogel, which has more of alpha-helical secondary structure upconverts into the loop after NIR laser exposure. However, in Silk@SWCNT-FA hydrogels, the NIR laser exposure induces more beta-sheet structure.

In our previous endeavors, we have shown the release of DOX from Silk@SWCNT-FA/DOX hydrogel post-NIR laser exposure.[55] A representative graphics presented in **Figure 4.2F** to explain it based on our observation. The incidence of NIR laser on hydrogel placed in PBS generates the heat that shrinks it by inducing the changes in internal structure. Due to this shrinkage, the drug squeezed out from the

hydrogel and supported its release. It is concluded that the drug release from Silk@SWCNT-FA/DOX hydrogel could be controlled by drug loading amount and time of NIR laser exposure.

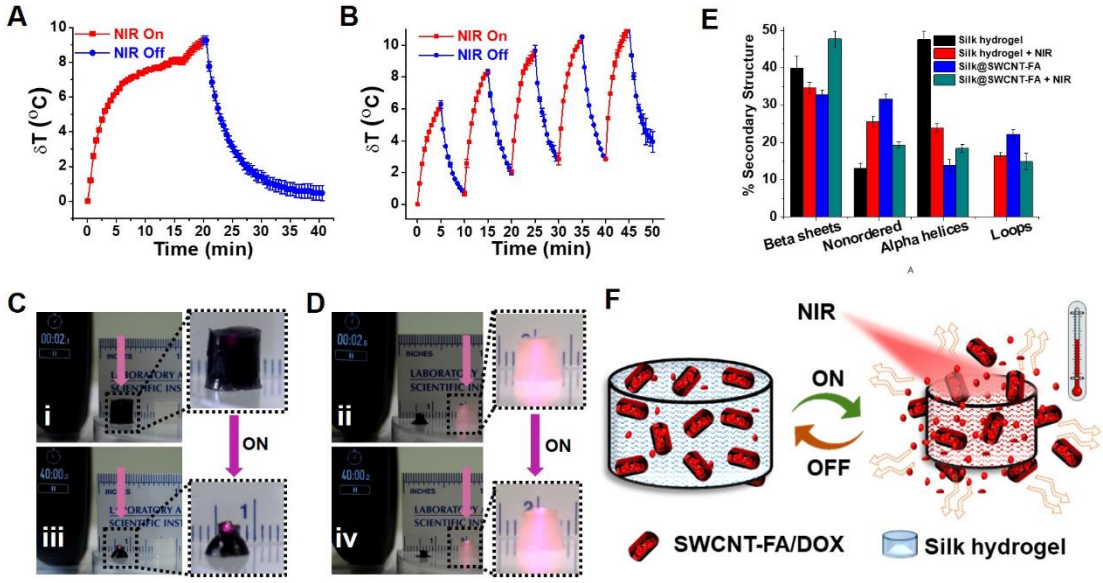

Figure 4.2. *The time-temperature plot of Silk@SWCNT-FA hydrogels exposed to NIR laser for* ***(A)*** *single 20 min ON/OFF cycle and* ***(B)*** *series of five cycles with 5 min turn on and off (n=3, Mean ± SD). Representative screenshot of supplementary video-1 showing* ***(C)*** *Silk@SWCNT-FA hydrogels shrinkage on NIR laser exposure and compared with* ***(D)*** *silk hydrogel with similar exposure.* ***(E)*** *Secondary structure change was calculated by deconvolution of amide I peak from three independent FTIR spectra (n=3, Mean ± SD) for silk hydrogel and Silk@SWCNT-FA hydrogels before and after NIR laser exposure.* ***(F)*** *A graphical representation of exposing Silk@SWCNT-FA hydrogels with NIR laser to stimulate the drug release.*

4.3.3. *In vivo* tumor regression study

The anti-cancer efficacy of Silk@SWCNT-FA/DOX was evaluated in 4T1 tumor-bearing female Balb/c mice. The animals were segregated randomly into seven groups: (1) untreated, (2) fDOX treated, (3) Silk@fDOX hydrogel treated, and (4) to (7) Silk@SWCNT-FA/DOX nanocomposite hydrogel treated. Group (4) was without external stimulation, (5) was stimulated with NIR laser, (6) was stimulated with an electric field, and (7) was stimulated with both NIR laser and electric field. Groups (5) to (7) were exposed to their respective stimulations every alternate day. The animals were treated twice during the 21-day study; the first treatment was given on day 0 followed by the second dose on day 10. **Figure 4.3A** representing ultrasound images of tumor

recorded every 7th day from treatment day (day 0) to sacrifice day (day 21), and tumor volume was calculated using dedicated software. The normal respiration rate and electrocardiogram (ECG) peaks recorded during the tumor imaging. Also, 37 ^{o}C body temperature was recorded throughout the study, indicating consistent supervision of healthy animals habitat. The noticeable change in tumor size from day 0 to day 21 of all the treatment group animals is represented in **Figure A4.3**. Further, actual tumor volume change was calculated by normalizing the tumor volume of 7, 14 and 21 days to tumor volume of 0 day **(Figure 4.3B)**. The tumor growth of untreated group (1), intravenously fDOX treated group (2), and localized Silk@SWCNT-FA/DOX treated group (4) was exponentially increased. However, the tumor growth of localized Silk@fDOX treated group (2) was inhibited effectively. Interestingly, we observed significant tumor regression in localized Silk@SWCNT-FA/DOX treated group (5), (6), and (7), which received external stimulation of NIR laser, electric field, and both together, respectively. The tumors from all the animals were collected and arranged in a group-wise, depicting shrinkage in tumors of the group (5), (6) and (7) **(Figure 4.3C)**. An apparent difference in tumor weight was recorded which is corroborated with tumor volume data **(Figure 4.3D)**. Tumors of the group (5), (6), and (7) were less than 0.5 g in weight as compared to ~3 g of untreated group (1), which is ~6 times more than that of the treated groups. However, no considerable change in the animal's body weight was recorded during the study, which rules out any systemic toxicity or the possibility of other infectious diseases that might happen during the study **(Figure 4.3E)**.

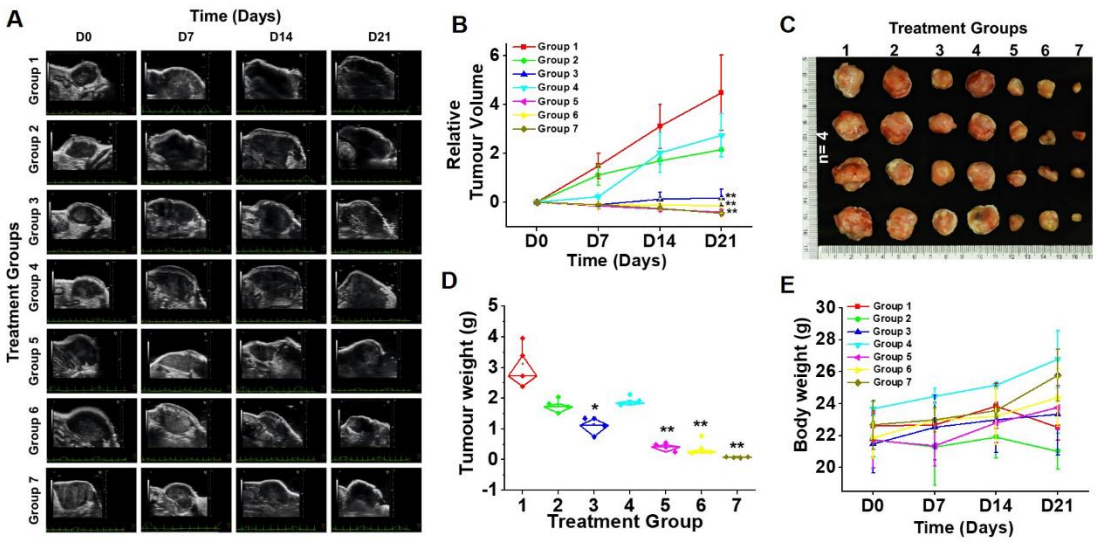

Figure 4.3. (A) *Representative ultrasound images of tumors of all groups were recorded every 7th day until 21 days.* ***(B)*** *The tumor volume was normalized from day 0 and*

relative tumor growth or regression was plotted till day 21. Animals were sacrificed on day 21, and ***(C)*** *excised tumors were arranged group-wise for visual comparison.* ***(D)*** *Representing harvested tumors weight and* ***(E)*** *body weight of tumor-bearing mice during the study. The representative treatment group are (1) untreated, (2) fDOX treated, (3) Silk@fDOX hydrogel treated, and (4) Silk@SWCNT-FA/DOX without stimulation (5) Silk@SWCNT-FA/DOX with NIR laser (6) Silk@SWCNT-FA/DOX with electric field and (7) Silk@SWCNT-FA/DOX with both NIR and electric field stimulation. The significant difference between the relative tumor volumes/weight of the treatment groups data acquired at day 21 was compared to the respective untreated control group (1) at a significance level of 0.01 and 0.005, which represented as *p ≤ 0.01 & **p ≤ 0.005 (n=4), respectively.*

The western blotting was performed over tumor samples, and the expression level of different apoptosis-related protein markers was evaluated. Bax to Bcl-2 ratio in cells is one of the major indicators of cell survival/apoptosis.[277, 278] Their bands on western blot **(Figure 4.4A)** depicts the change in their expression level due to the treatment. In the untreated tumor sample, Bax protein expression is low as compared to Bcl-2, which is opposite in the case of group (3), (6), and (7). Therefore their ratio, as plotted in F**igure 4.4B,** represents the survival state. The Bax to Bcl-2 ratio of group (1), (4) and (5) was less than one, as compared to group (2), (3), (6) and (7). The remarkably high expression of Bax and downregulation of Bcl-2 is associated with mitochondria-mediated apoptosis.[277, 278] Caspase-3 is a member of the cysteine-aspartic protease family, which plays a central role in initiating a cascade of apoptosis. The active form of this protease contains two subunits, one large and one small.[277] We observed high expression of the large subunit in untreated group (1) as compared to any other group; however, the small cleaved subunit expression level was increased in group (4), (6), and (7) (**Figure 4.4A & 4.4C)**. The enhanced expression of cleaved subunit attested to the activation of caspase 3 dimers for the initiation of apoptosis. The activated caspase 3 is known to induce the cleavage of PARP.[279] The enhanced cleaved PARP fragment was also detected in the group (6) and (7). PARP in its active form, functions as a nick sensor towards the DNA damage repair. Its cleavage by caspase 3 inactivates its function, which leads cells into apoptosis.[279] The caspase 8 expression level was more or less constant in all the groups **(Figure 4.4A & 4.4C)**. Caspase 12 expression was increased in group (4), (5), (6) and (7). Cleaved caspase 12 is a key protein of endoplasmic reticulum stress-mediated apoptosis.[280] Cleaved caspase 12 bands were explicitly observed in the group (7), which is the precursor for the cleavage and activation of other caspases such

as caspase 9 for the induction of the apoptosis. Further, cleaved caspase 9 expression was also enhanced in group (4), (6) and (7) **(Figure 4.4A & 4.4D)**. Caspase 9 induced the cleavage of caspase 3 for apoptosis induction.[280]

TUNEL assay was conducted to recognize the apoptotic nuclei in the cryosectioned slices of the tumor. At the end of the assay, the insoluble brown color substrate is formed at the site of DNA fragmentation, which is a characteristic of apoptosis. The counterstain with methyl green assists in the evaluation of the morphology of healthy/apoptotic cells. **Figure 4.4E** depicts no apoptotic nuclei in group (1) and group (4). However, very few cells of the group (2) and (3) showed apoptotic cells. In group (5), (6), and (7), almost all the cells are showing brown color complex, wherein the apoptotic nuclei of group (7) were very distinct as compared to group (5) and (6) which are looking disintegrated. This indicates that group (7) tumors are undergoing apoptosis and group (5) and (6) are going through both necrosis and apoptosis.

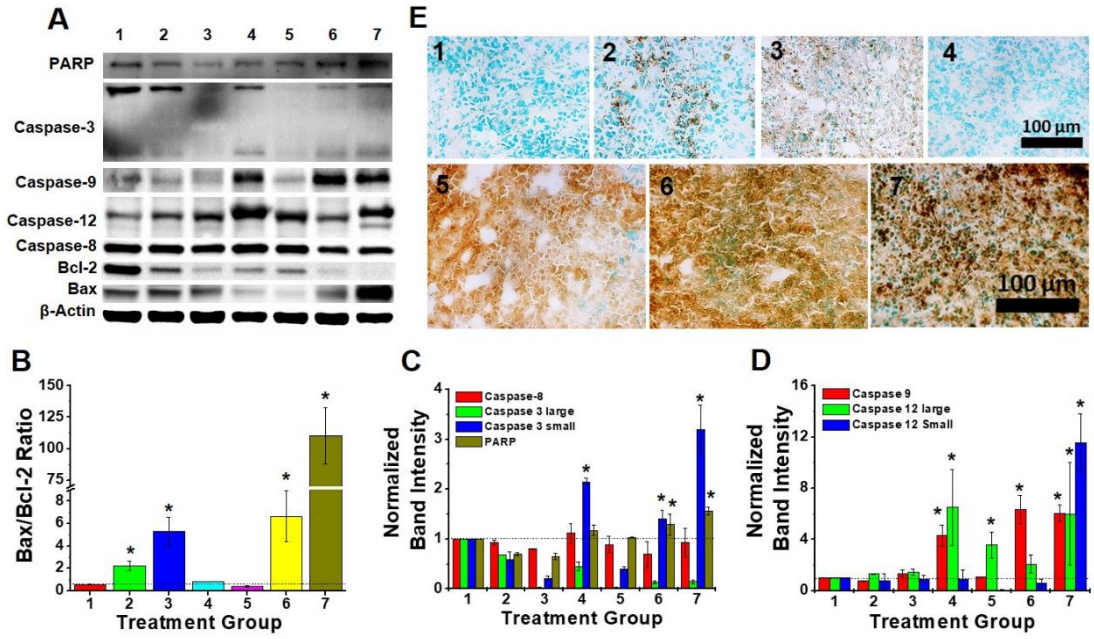

Figure 4.4. (A) *Representative western blots are depicting bands of specified apoptosis protein markers in all the seven groups of study. The band intensity ratio of Bax and Bcl 2* ***(B)*** *and normalized band intensity of* ***(C)*** *caspase 8, caspase 3, PARP, and* ***(D)*** *caspase 9 and caspase 12 were plotted as a histogram. (E) TUNEL-assay images of the tumor to investigate apoptosis. The representative treatment groups are (1) untreated, (2) fDOX treated, (3) Silk@fDOX hydrogel treated, and (4) Silk@SWCNT-FA/DOX without stimulation (5) Silk@SWCNT-FA/DOX with NIR laser (6) Silk@SWCNT-FA/DOX with electric field and (7) Silk@SWCNT-FA/DOX with both NIR and electric field stimulation.*

*The significant difference between the band intensities of treatment groups was compared to the untreated control group (1) at a significance level of 0.001 and represented as *p ≤ 0.001 (n=3).*

The histological sections of the tumor, heart, liver, kidney, and spleen stained with H&E are shown in the figure. The tumor H&E images are supporting TUNEL assay data. The cell and nucleus morphology looks intact in the group (1) and (4). Disintegrated nucleus and enlarge cell morphology indicated necrosis in the group (2), (3), (5) and (6). However, cell shrinkage and nucleus blebbing of group (7) indicated apoptosis **(Figure 4.5)**. The histology of heart, liver, kidney, and spleen looks healthy, and no considerable changes/toxicities among the various treatment groups are observed.

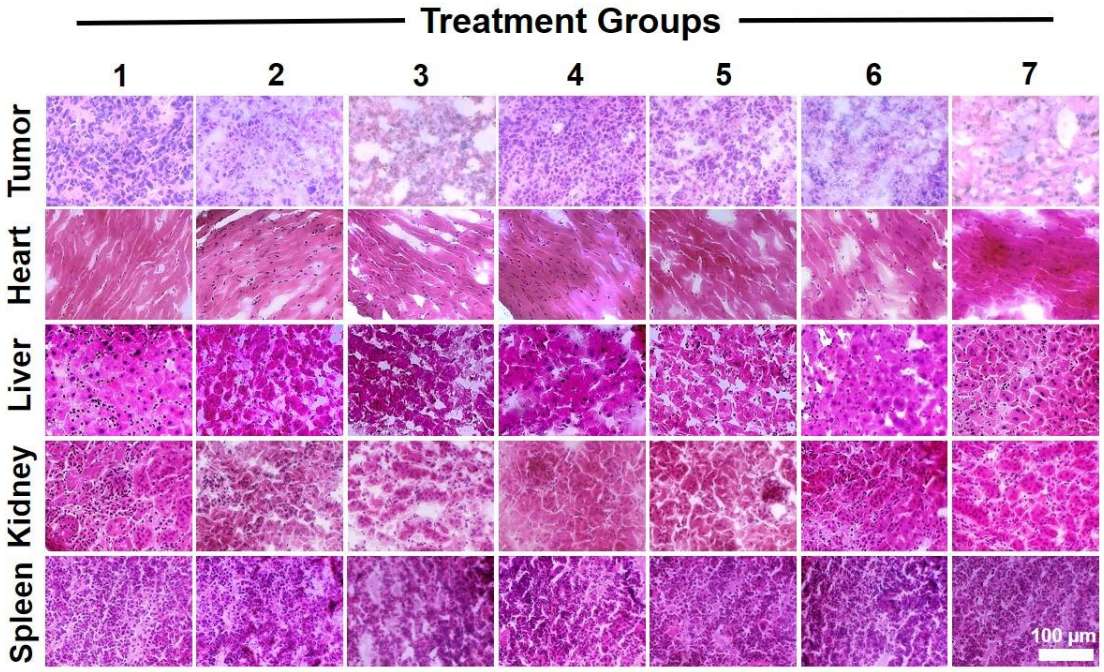

Figure 4.5. *H&E images of the tumor and healthy tissue as labeled. The representative treatment group are (1) untreated, (2) fDOX treated, (3) Silk@fDOX hydrogel treated, and (4) Silk@SWCNT-FA/DOX without stimulation (5) Silk@SWCNT-FA/DOX with NIR laser (6) Silk@SWCNT-FA/DOX with electric field and (7) Silk@SWCNT-FA/DOX with both NIR and electric field stimulation.*

The cancer chemotherapy with DOX has been well reported to be associated with cardiotoxicities.[281] The cardiac function was analyzed non invasively using echocardiography was performed at the beginning (day 0) and the last day (day 21) of the treatment to determine any sign of cardiotoxicity. We observed no significant difference in the cardiac parameters from day 0 to day 21 as shown in F**igure 4.6**. The parameters like heart rate (310-840 beats per minutes), cardiac output (20-35 mL/min),

stroke volume (40-70 µL), ejection fraction (55-85 %), fractional shortening (30-50 %), LVPW;d, LVPW;s, LVAW;d, and LVAW;s (0.5 to 1.5 mm) were found to be within the normal range as reported for healthy mice in MKT02620 imaging guides, FUJIFILM VisualSonics Inc, Netherland.[282] Our echocardiographic data is also corroborated with the heart histology H&E image **(Figure 4.5)** showing no cardiotoxicity among the treatment groups. This might be due to little dose (total 300 µg) of DOX injected at the systemic (group 2) or localized (group 3 to 7) site for the therapy.

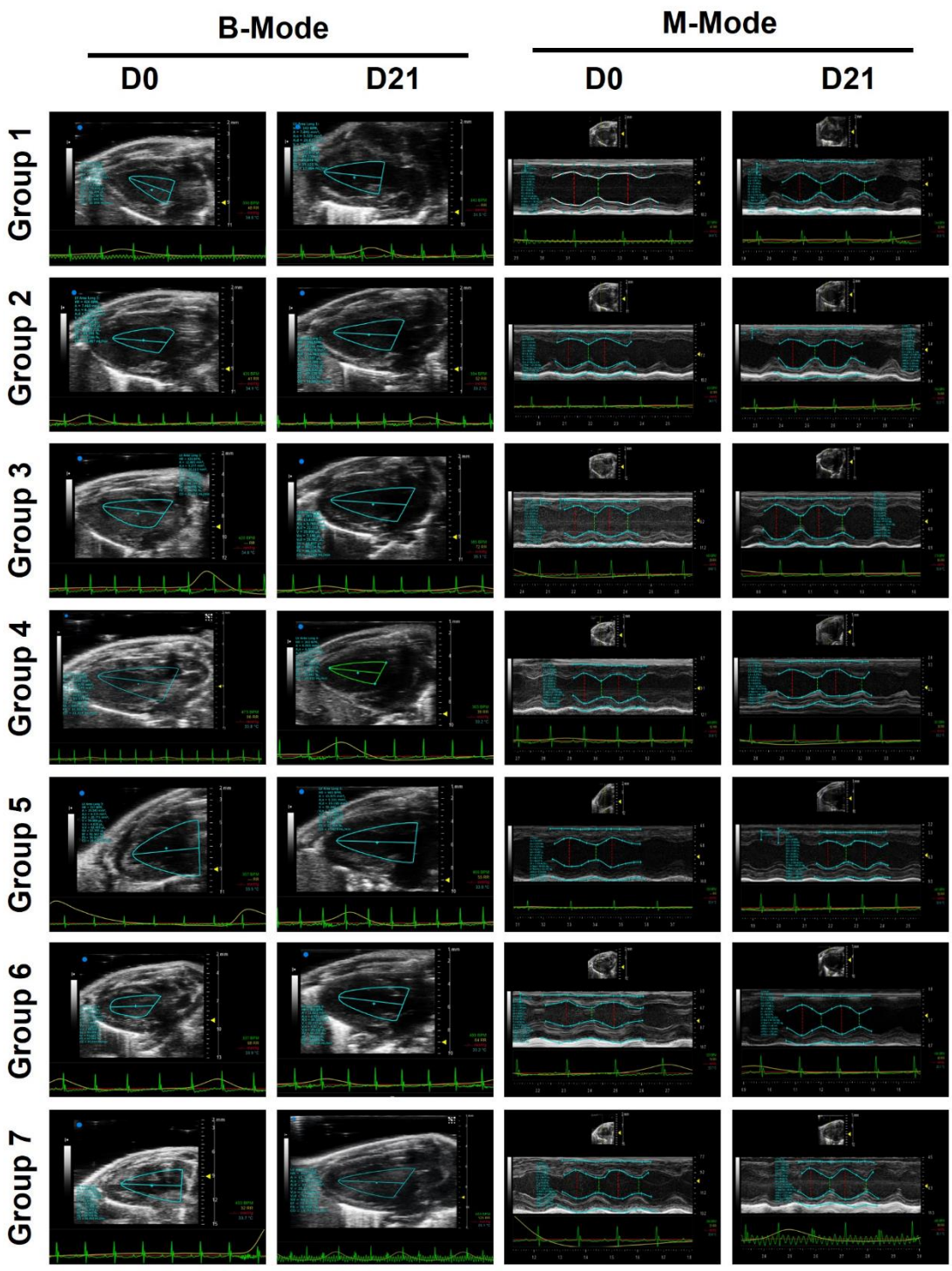

Figure 4.6. *The B-mode and M-mode images of echocardiographic measurements in mice. The representative treatment group are (1) untreated, (2) fDOX treated, (3) Silk@fDOX hydrogel treated, and (4) Silk@SWCNT-FA/DOX without stimulation (5) Silk@SWCNT-FA/DOX with NIR laser (6) Silk@SWCNT-FA/DOX with electric field and (7) Silk@SWCNT-FA/DOX with both NIR and electric field stimulation.*

4.4. Discussion

Silk is a resorbable, natural protein-polymer that responds to pH change and are susceptible to proteases for sustained drug release. Its biocompatibility and flexibility to mold into various formats aids in to make silk a preferred choice of biomaterial for various biomedical applications. The localized site-specific delivery of bioactive molecules through various formats, including hydrogel, nanoparticles, films, or scaffolds are documented by researchers extensively.[56, 103, 104, 194, 197, 262, 263, 283] Tumor regression studies using silk hydrogel loaded with anticancer drug DOX conducted by Kaplan group showed promising results.[104, 194] However, silk in its native form is electrically non-conductivity material, which also does not respond to NIR laser. Taken this into account, we employed the concept of nanotechnology and polymer sciences and came up with a nanocomposite hydrogel system that has the properties of both the polymer (silk) and nanocarrier. In this regard, the addition of CNTs into various other polymers such as gelatin, chitosan, polyethylene glycol, etc. has been shown previously for either electrical or NIR light-responsive drug release and tissue engineering applications.[113, 261, 284] However, difficulty in processing flexibility/ feasibility, the use of toxic chemical crosslinker, low mechanical strength, and high cost are few limitations of these polymers. Silk, on the other hand, has all these properties and is easily sourced. They are biodegradable, immunocompatible and produce nontoxic resorbable amino acids as degradation products. In our previous work,[55] we have introduced SWCNT in crosslinker free silk hydrogel and presented its NIR laser responsive behavior *in vitro* for targeted cell cytotoxicity. In continuation from here, the Silk@SWCNT-FA hydrogel was explored further for its electric field triggered drug-releasing behavior. Followed by this *in vivo* tumor regression, “proof of concept” study was conducted by individual and simultaneous application of NIR laser and electric field. To our knowledge, this is the first report to show such *in vivo* study where two external stimuli were applied together for efficient tumor therapy.

In our previous endeavors,[55] we have shown the specific targeting and internalization of SWCNT-FA into folic acid receptor-positive cancer cells. 4T1 breast solid tumor has been reported to overexpress the folic acid receptors,[285], which makes it a suitable animal tumor model to test our Silk@SWCNT-FA/DOX hydrogel system for proof of concept study. The systemically delivered fDOX (group 2) could not reach and maintain the anticancer drug dose at tumor site due to the complex

microenvironment; therefore, it could not resist tumor growth. In such a scenario, the localized therapy could be advantageous.[262] The solid tumor prolonged exposure to adjacently available hydrogel encapsulating anti-cancer drugs weakens it and provides a high chance to cure this chronic disease. In this regard, Silk@SWCNT-FA/DOX hydrogel was administered near to the tumor (group 4 to 7) and exposed to the external stimulus (group 5 to 7). We observed significant tumor shrinkage on the application of 808 nm NIR laser (group 5), 1.0 V electric field (group 6), and both together (group 7). The 1.0 V of DC voltage is very mild to be applied and electrodes should not get heated in 5 min treatment, which may also rule out any damage caused to the nearby tissue where electrodes were placed. Previously, researchers have also tried 1.0 to 10 V of voltage on subcutaneously implanted electro responsive hydrogels and ensure the safety of the procedure.[215, 260] Similarly, NIR laser irradiation at a power of 0.2 W/cm^2, 808 nm wavelength is under the range (0.1 to 0.3 W/cm^2), which has been tried *in vivo* previously for stimulating various subcutaneously or near/intratumorally injected photo thermoresponsive hydrogels.[55, 144, 264, 274]

The Silk@SWCNT-FA/DOX implanted locally near to the tumor and exposed individually by NIR laser (group 5, n=4) or electric field (group 6, n=4) endorses its anticancer effect *in situ* and induces both necrosis and apoptosis in deadly solid tumor cells. However, their simultaneous application (group 7) synergistically induced apoptosis. The NIR laser penetrated deep into the tissue to be reached and absorbed by the locally implanted Silk@SWCNT-FA/DOX hydrogel for the production of a significantly high amount of heat. This photothermal effect would rearrange the silk matrix in situ for triggering the release of SWCNT-FA/DOX as shown in our in vitro data **(Figure 4.2).** The released SWCNT-FA/DOX was internalized by folic acid receptor-positive 4T1 breast tumor cells as we have explained in our previously published *in vitro* data to induce cell death by apoptosis.[55] Due to the localized hyperthermia, tumor cells also get too feeble to stand against the chemotherapy, and this might also inhibit the drug resistance development by the tumor. The application of the electric field (group 6) encourages the interaction between cationic drug DOX and anionic nanocarrier SWCNT-FA due to electrically induced charge polarization effect. The removal of the electric field, however, reduces those electrostatic interactions and drug percolates into the tumor to show its anticancer activity. The electric field application has also been demonstrated to enhance the permeability of cell membranes

to ions and macromolecules; the phenomena is well known as electrochemotherapy.[286] We hypothesized that on the application of electric field the tumor cell permeability also increases, which supports the internalization of released drug molecules and nanocarrier for their cytotoxic effects. Further, the simultaneous application of NIR laser and the electric field (group 7), was more effective as it permeabilizes the tumor for infiltration of SWCNT-FA/DOX deep into it. Once inside, the NIR laser illumination produces heat and induce DOX release for a higher therapeutic index. Therefore, the simultaneous application of the NIR laser and electric field has a synergistic effect of inhibiting tumor growth.

The external stimulation played a key role here for the therapy because the control group (4), which also received Silk@SWCNT-FA/DOX hydrogel treatment at its tumor site, showed exponential growth similar to the untreated group (1), as the drug molecule loaded on nano vehicle entrapped inside the silk matrix and could not be released for the therapeutic effect. Usually, the nanocarrier embedding is suggested to inhibit the burst release of drug molecules from various polymeric hydrogels. However, sustained DOX release for tumor growth inhibition from the silk hydrogel is reported.[104, 194] We also observed tumor growth inhibition in Silk@fDOX treated group (3); however, the insertion of SWCNT allowed us to control the rate of drug release on demand which drastically enhanced its therapeutic effects compared to the former as well as caused the significant tumor regression.

SWCNTs also acts as photosensitizer agent which on the exposure of NIR laser produce the reactive oxygen species (ROS) along with hyperthermia for photodynamic (PDT) and photothermal (PTT) tumor therapy.[272, 287] The locally generated ROS potentially induce necrosis or apoptosis in tumor tissue for its destruction. Therefore, theoretically, ROS might also play some specific roles in the shrinkage of tumors observed during externally regulated treatment.

The biosafety associated with CNT applications in vivo has always been a topic of debate. De Menezes et al., in a recent review, has compiled literature in the field and showed that CNT biocompatibility could be enhanced by chemical modification, target specific delivery to reduce non-specific localization and nanocomposite formation.[288] In our present approach, we have followed all these three strategies. The SWCNT was oxidized and chemically modified with folic acid. Due to the folic acid, the SWCNT-FA

was explicitly targeted to folic acid receptor overexpressing cancer cells, which reduced its non-specific localization. Further, the SWCNT-FA/DOX embedding in the silk fibroin hydrogel matrix formed its nanocomposites. We have shown the biocompatibility of SWCNT-FA previously in vitro for oral cancer cell line (KB) and lung cancer cell line (A549).[55] Many research groups have also demonstrated the mechanism of CNT enzymatic degradation by neutrophil and macrophages cells.[289-291] Furthermore, in the present manuscript, evidence from H&E images of tissues like heart, liver, kidney, and spleen in **Figure 4.5** did not show any signs of CNT mediated cytotoxicity in vivo.

fDOX is a clinically approved anticancer drug having strong antitumor effects; however, at either higher dose or with multiple injections. In our study, all the animals were treated twice during the 21-day study, with an equivalent dose of 6 mg per kg body weight (~150 µg) DOX either intraperitoneally (group 2) or locally (group 3 to 7) near to the tumor. The exponential tumor growth of group (2) animals was due to the intraperitoneal low-dose injection that delivered the drug systemically. However, the same amount of locally administered drugs significantly inhibited the tumor growth in groups 3, 5, 6, and 7. Our investigations, therefore, suggest that the local drug delivery vehicles are the advanced cancer therapeutic options that can reduce drug doses with fewer injections cycle, which further ensures the pain-free and patient-friendly treatment procedure.

4.5. Significant findings

The salient findings from this chapter are as follow –

1. The Silk@SWCNT-FA/DOX nanocomposite hydrogel system was successfully implanted near to the mice breast tumor through a syringe in a minimally invasive way.

2. The nanocomposite silk hydrogel showed electrical conductivity and NIR laser-induced hyperthermia properties. Also, the heat generation from nanocomposite hydrogel is high enough to destroy the tumor, suggesting the localized photothermal effect coupled with chemotherapy.

3. The drug release from the implanted nanocomposite hydrogel was controlled from the outside by noninvasive electric field and NIR laser application.

4. The simultaneous application of NIR laser and electric voltage pulse showed improved tumor suppression effect.

5. The Dose and Frequency of injections required for the treatment were reduced due to local therapy. The low frequency of injections makes it a pain-free patient-friendly procedure.

6. The localized treatment accumulates the chemo drug molecules to the tumor site and reduces the side effects to nearby healthy tissues, as revealed by electrocardiogram and H&E images. Therefore, we did not observe any DOX related cardiac/systemic toxicity during the procedure.

SUMMARY AND FUTURE PERSPECTIVES

SUMMARY AND FUTURE PERSPECTIVES

As shown in **Figure S1** below, the current thesis dealt with the fabrication of two types of injectable nanocomposite silk hydrogel system (I & II). Both the systems were developed by blending mulberry (*B. mori*) and nonmulberry (*A. assama*) aqueous silk fibroin protein along with either BMNP for an injectable system I, as described in ***Chapter 2*** or SWCNT for injectable system II as described in ***Chapter 3 & 4***. The type of embedded nanocarrier dictated the unique properties of these systems. The injectable system I was assessed for its long term functionality *in vitro* by culturing stomach cancer cells in specially designed scaffolds. However, the injectable system II was developed to target and precisely deliver the anticancer drug in folic acid receptors overexpressing cancer cells. The target-specific drug delivery 'proof of concept' study was first conducted *in vitro* in an oral cancer cell line ***(Chapter 3),*** which further extended and validated into *in vivo* breast tumor regression study ***(Chapter 4)***.

From the thesis, it is concluded that the developed injectable system is highly flexible and can be used to deliver a range of anticancer drugs. The proposed system has shown higher efficacy in treating cancer with lower systemic toxicity. Also, if translated, this technology may reduce the repeated cycles of chemotherapy and the need for patient hospitalization.

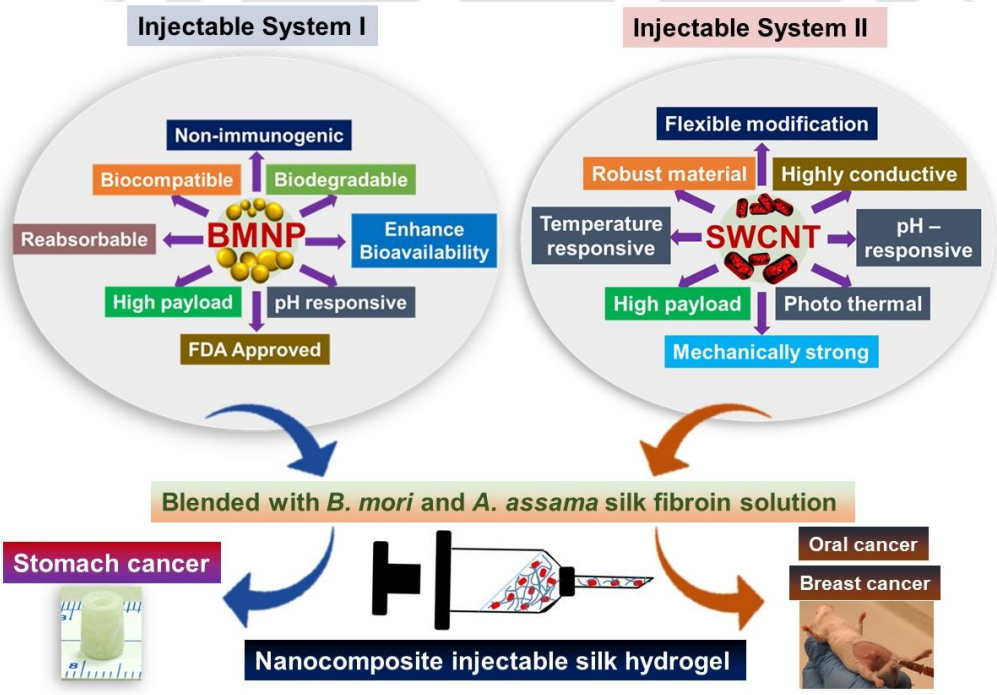

Figure S1. Illustration showing the graphical summary and conclusion of the thesis.

The injectable system developed here is a flexible system that can be modified according to the requirement. Many nanoparticles and anticancer drugs could be integrated into the matrix to explore its efficacy in the future. **Figure S2** below is showing a prospective future application of the injectable silk hydrogel. The hydrogel could find its applications in soft tissue engineering like cartilage, liver, and heart tissue regeneration, where various growth factors delivery is needed. Additionally, various other chronic diseases such as diabetes, arthritis, and Parkinson's, which require sustained interaction with the drug, can be treated with bioactive molecule delivery. The small animal study indicated the superior antitumor potential of our developed injectable nanocomposite hydrogel system and made it ready for future clinical trials. We highly believe that if translated our technology, has the potential to save humanity from the clutches of cancers.

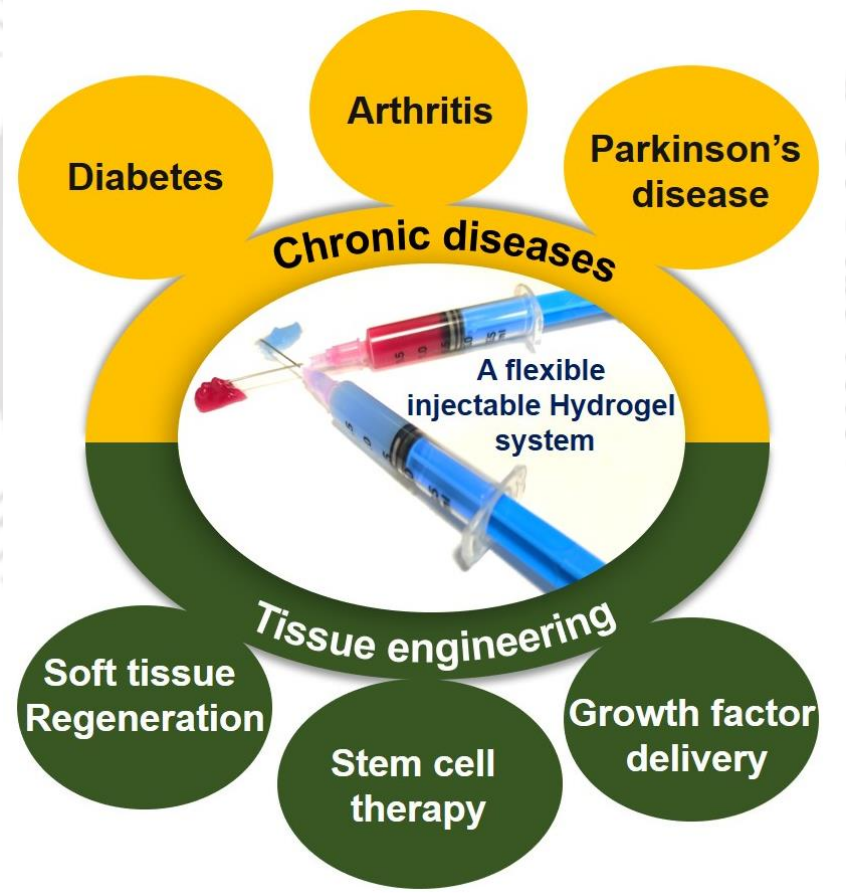

Figure S2. Illustration of prospective future applications of injectable hydrogel system.

Bibliography

[1] A. Jemal, R. Siegel, E. Ward, Y. Hao, J. Xu, T. Murray, M.J. Thun, Cancer statistics, 2008, CA: A Cancer Journal for Clinicians 58(2) (2008) 71-96.

[2] S. Malvia, S.A. Bagadi, U.S. Dubey, S. Saxena, Epidemiology of breast cancer in Indian women, Asia-Pacific Journal of Clinical Oncology 13(4) (2017) 289-295.

[3] S.K. Singh, B.K. Bhunia, N. Bhardwaj, S. Gilotra, B.B. Mandal, Reloadable silk-hydrogel hybrid scaffolds for sustained and targeted delivery of molecules, Molecular Pharmaceutics 13(12) (2016) 4066-4081.

[4] J. Ferlay, I. Soerjomataram, R. Dikshit, S. Eser, C. Mathers, M. Rebelo, D.M. Parkin, D. Forman, F. Bray, Cancer incidence and mortality worldwide: sources, methods and major patterns in GLOBOCAN 2012, International Journal of Cancer 136(5) (2015) E359-E386.

[5] J. Ferlay, M. Colombet, I. Soerjomataram, C. Mathers, D. Parkin, M. Piñeros, A. Znaor, F. Bray, Estimating the global cancer incidence and mortality in 2018: GLOBOCAN sources and methods, International Journal of Cancer 144(8) (2019) 1941-1953.

[6] J. Ferlay, M. Colombet, I. Soerjomataram, Global and regional estimates of the incidence and mortality for 38 cancers, GLOBOCAN 2018 (2018).

[7] H.A. Idikio, Human cancer classification: a systems biology-based model integrating morphology, cancer stem cells, proteomics, and genomics, Journal of Cancer 2 (2011) 107.

[8] D. Lorusso, E. Bria, A. Costantini, M. Di Maio, G. Rosti, A. Mancuso, Patients' perception of chemotherapy side effects: Expectations, doctor–patient communication and impact on quality of life–An Italian survey, European Journal of Cancer Care (2016).

[9] R. Oun, Y.E. Moussa, N.J. Wheate, The side effects of platinum-based chemotherapy drugs: a review for chemists, Dalton Transactions 47(19) (2018) 6645-6653.

[10] D.W. Kim, Y.S. Jo, H.S. Jung, H.K. Chung, J.H. Song, K.C. Park, S.H. Park, J.H. Hwang, S.Y. Rha, G.R. Kweon, An orally administered multitarget tyrosine kinase inhibitor, SU11248, is a novel potent inhibitor of thyroid oncogenic RET/papillary thyroid cancer kinases, The Journal of Clinical Endocrinology & Metabolism 91(10) (2006) 4070-4076.

[11] S. Bettuzzi, M. Brausi, F. Rizzi, G. Castagnetti, G. Peracchia, A. Corti, Chemoprevention of human prostate cancer by oral administration of green tea catechins in volunteers with high-grade prostate intraepithelial neoplasia: a preliminary report from a one-year proof-of-principle study, Cancer Research 66(2) (2006) 1234-1240.

[12] P.M. Hoff, R. Ansari, G. Batist, J. Cox, W. Kocha, M. Kuperminc, J. Maroun, D. Walde, C. Weaver, E. Harrison, Comparison of oral capecitabine versus intravenous fluorouracil plus leucovorin as first-line treatment in 605 patients with metastatic colorectal cancer: results of a randomized phase III study, Journal of Clinical Oncology 19(8) (2001) 2282-2292.

[13] P. Reichardt, G. Von Minckwitz, P. Thuss-Patience, W. Jonat, H. Kölbl, F. Jänicke, D. Kieback, W. Kuhn, A. Schindler, S. Mohrmann, Multicenter phase II study of oral capecitabine (Xeloda ") in patients with metastatic breast cancer relapsing after treatment with a taxane-containing therapy, Annals of Oncology 14(8) (2003) 1227-1233.

[14] W.S. Lasota, D.L. de Valeriola, M.J. Piccart, Potential role of oral anthracyclines in older patients with cancer, Drugs & Aging 4(5) (1994) 392-402.

[15] S. Chia, W. Gradishar, L. Mauriac, J. Bines, F. Amant, M. Federico, L. Fein, G. Romieu, A. Buzdar, J.F. Robertson, Double-blind, randomized placebo controlled trial of fulvestrant compared with exemestane after prior nonsteroidal aromatase inhibitor therapy in postmenopausal women with hormone receptor–positive, advanced breast cancer: results from EFECT, Journal of Clinical Oncology 26(10) (2008) 1664-1670.

[16] N. Dhillon, B.B. Aggarwal, R.A. Newman, R.A. Wolff, A.B. Kunnumakkara, J.L. Abbruzzese, C.S. Ng, V. Badmaev, R. Kurzrock, Phase II trial of curcumin in patients with advanced pancreatic cancer, Clinical Cancer Research 14(14) (2008) 4491-4499.

[17] J. Aisner, Overview of the changing paradigm in cancer treatment: Oral chemotherapy, American Journal of Health-System Pharmacy 64(9) (2007).

[18] K. Hande, Etoposide: four decades of development of a topoisomerase II inhibitor, European Journal of Cancer 34(10) (1998) 1514-1521.

[19] G. Minotti, P. Menna, E. Salvatorelli, G. Cairo, L. Gianni, Anthracyclines: molecular advances and pharmacologic developments in antitumor activity and cardiotoxicity, Pharmacological Reviews 56(2) (2004) 185-229.

[20] K. Tripathi, Essentials of medical pharmacology, JP Medical Ltd 2013.

[21] M. Markman, Hormonal therapy of endometrial cancer, European Journal Of Cancer 41(5) (2005) 673-675.

[22] D.E. Peterson, K. Öhrn, J. Bowen, M. Fliedner, J. Lees, C. Loprinzi, T. Mori, A. Osaguona, D.S. Weikel, S. Elad, Systematic review of oral cryotherapy for management of oral mucositis caused by cancer therapy, Supportive Care in Cancer 21(1) (2013) 327-332.

[23] J. Lankelma, H. Dekker, R.F. Luque, S. Luykx, K. Hoekman, P. van der Valk, P.J. van Diest, H.M. Pinedo, Doxorubicin gradients in human breast cancer, Clinical Cancer Research 5(7) (1999) 1703-1707.

[24] L.R. Dick, P.E. Fleming, Building on bortezomib: second-generation proteasome inhibitors as anti-cancer therapy, Drug Discovery Today 15(5) (2010) 243-249.

[25] M.E. Davis, D.M. Shin, Nanoparticle therapeutics: an emerging treatment modality for cancer, Nature Reviews Drug Discovery 7(9) (2008) 771-782.

[26] F. Kabbinavar, H.I. Hurwitz, L. Fehrenbacher, N.J. Meropol, W.F. Novotny, G. Lieberman, S. Griffing, E. Bergsland, Phase II, randomized trial comparing bevacizumab plus fluorouracil (FU)/leucovorin (LV) with FU/LV alone in patients with metastatic colorectal cancer, Journal of Clinical Oncology 21(1) (2003) 60-65.

[27] W.P. McGuire, W.J. Hoskins, M.F. Brady, P.R. Kucera, E.E. Partridge, K.Y. Look, D.L. Clarke-Pearson, M. Davidson, Cyclophosphamide and cisplatin compared with paclitaxel and cisplatin in patients with stage III and stage IV ovarian cancer, New England Journal of Medicine 334(1) (1996) 1-6.

[28] M. Martin, A. Villar, A. Sole-Calvo, R. Gonzalez, B. Massuti, J. Lizon, C. Camps, A. Carrato, A. Casado, M. Candel, Doxorubicin in combination with fluorouracil and cyclophosphamide (iv FAC regimen, day 1, 21) versus methotrexate in combination with fluorouracil and cyclophosphamide (iv CMF regimen, day 1, 21) as adjuvant chemotherapy for operable breast cancer: a study by the GEICAM group, Annals of Oncology 14(6) (2003) 833-842.

[29] M.I. Koukourakis, G. Kyrias, S. Kakolyris, C. Kouroussis, C. Frangiadaki, A. Giatromanolaki, G. Retalis, V. Georgoulias, Subcutaneous administration of amifostine during fractionated radiotherapy: a randomized phase II study, Journal of Clinical Oncology 18(11) (2000) 2226-2233.

[30] L. Kelland, The resurgence of platinum-based cancer chemotherapy, Nature Reviews Cancer 7(8) (2007) 573-584.

[31] A. Jones, F. MacNeill, S. Jacobs, P. Lonning, M. Dowsett, T. Powles, The influence of intramuscular 4-hydroxyandrostenedione on peripheral aromatisation in breast cancer patients, European Journal of Cancer 28(10) (1992) 1712-1716.

[32] R. Kurzrock, M.G. Rosenblum, S.A. Sherwin, A. Rios, M. Talpaz, J.R. Quesada, J.U. Gutterman, Pharmacokinetics, single-dose tolerance, and biological activity of recombinant gamma-interferon in cancer patients, Oncology 42(Suppl. 1) (1985) 41-50.

[33] G. Gonzalez, T. Crombet, F. Torres, M. Catala, L. Alfonso, M. Osorio, E. Neninger, B. Garcia, A. Mulet, R. Perez, Epidermal growth factor-based cancer vaccine for non-small-cell lung cancer therapy, Annals of Oncology 14(3) (2003) 461-466.

[34] H.L. Kaufman, H. Hörig, F.A. Medina, S. Golding, W.A. Conkright, Strategies for cancer therapy using carcinoembryonic antigen vaccines, Expert Reviews in Molecular Medicine 2(03) (2000) 1-24.

[35] C.N. Landen, W.M. Merritt, L.S. Mangala, A.M. Sanguino, C. Bucana, C. Lu, Y.G. Lin, L.Y. Han, A.A. Kamat, R.E. Schmandt, Intraperitoneal delivery of liposomal siRNA for therapy of advanced ovarian cancer, Cancer Biology & Therapy 5(12) (2006) 1708-1713.

[36] P.H. Sugarbaker, J.T. Mora, P. Carmignani, O.A. Stuart, D. Yoo, Update on chemotherapeutic agents utilized for perioperative intraperitoneal chemotherapy, The oncologist 10(2) (2005) 112-122.

[37] K. Kawakami, M. Kawakami, S.R. Husain, R.K. Puri, Targeting interleukin-4 receptors for effective pancreatic cancer therapy, Cancer Research 62(13) (2002) 3575-3580.

[38] R.F. Ozols, R.C. Young, J.L. Speyer, P.H. Sugarbaker, R. Greene, J. Jenkins, C.E. Myers, Phase I and pharmacological studies of adriamycin administered intraperitoneally to patients with ovarian cancer, Cancer Research 42(10) (1982) 4265-4269.

[39] P. Moreau, H. Pylypenko, S. Grosicki, I. Karamanesht, X. Leleu, M. Grishunina, G. Rekhtman, Z. Masliak, T. Robak, A. Shubina, Subcutaneous versus intravenous administration of bortezomib in patients with relapsed multiple myeloma: a randomised, phase 3, non-inferiority study, The lancet oncology 12(5) (2011) 431-440.

[40] K. Hong, A. Khwaja, E. Liapi, M.S. Torbenson, C.S. Georgiades, J.-F.H. Geschwind, New intra-arterial drug delivery system for the treatment of liver cancer: preclinical assessment in a rabbit model of liver cancer, Clinical Cancer Research 12(8) (2006) 2563-2567.

[41] S. Sharma, D. White, A.R. Imondi, M.E. Placke, D.M. Vail, M.G. Kris, Development of inhalational agents for oncologic use, Journal of Clinical Oncology 19(6) (2001) 1839-1847.

[42] M. Ferrari, Cancer nanotechnology: opportunities and challenges, Nature Reviews Cancer 5(3) (2005) 161-171.

[43] L. Mei, Z. Zhang, L. Zhao, L. Huang, X.-L. Yang, J. Tang, S.-S. Feng, Pharmaceutical nanotechnology for oral delivery of anticancer drugs, Advanced drug delivery reviews 65(6) (2013) 880-890.

[44] D. Peer, J.M. Karp, S. Hong, O.C. Farokhzad, R. Margalit, R. Langer, Nanocarriers as an emerging platform for cancer therapy, Nature nanotechnology 2(12) (2007) 751-760.

[45] A. Schroeder, D.A. Heller, M.M. Winslow, J.E. Dahlman, G.W. Pratt, R. Langer, T. Jacks, D.G. Anderson, Treating metastatic cancer with nanotechnology, Nature Reviews Cancer 12(1) (2012) 39-50.

[46] K. Cho, X. Wang, S. Nie, D.M. Shin, Therapeutic nanoparticles for drug delivery in cancer, Clinical Cancer Research 14(5) (2008) 1310-1316.

[47] S.-r. Ji, C. Liu, B. Zhang, F. Yang, J. Xu, J. Long, C. Jin, D.-l. Fu, Q.-x. Ni, X.-j. Yu, Carbon nanotubes in cancer diagnosis and therapy, Biochimica et Biophysica Acta (BBA)-Reviews on Cancer 1806(1) (2010) 29-35.

[48] N. Oliva, J.o. Conde, K. Wang, N. Artzi, Designing hydrogels for on-demand therapy, Accounts of chemical research 50(4) (2017) 669-679.

[49] J.Y. Seo, B. Lee, T.W. Kang, J.H. Noh, M.J. Kim, Y.B. Ji, H.J. Ju, B.H. Min, M.S. Kim, Electrostatically interactive injectable hydrogels for drug delivery, Tissue engineering and regenerative medicine 15(5) (2018) 513-520.

[50] F. Ullah, M.B.H. Othman, F. Javed, Z. Ahmad, H.M. Akil, Classification, processing and application of hydrogels: A review, Materials Science and Engineering: C 57 (2015) 414-433.

[51] B.D. Ratner, A.S. HOFFMAN, Synthetic hydrogels for biomedical applications, ACS Publications1976.

[52] S. Grijalvo, J. Mayr, R. Eritja, D.D. Díaz, Biodegradable liposome-encapsulated hydrogels for biomedical applications: a marriage of convenience, Biomaterials science 4(4) (2016) 555-574.

[53] D.G. Anderson, J.A. Burdick, R. Langer, Smart biomaterials, Science 305(5692) (2004) 1923-1924.

[54] D. Liu, F. Yang, F. Xiong, N. Gu, The smart drug delivery system and its clinical potential, Theranostics 6(9) (2016) 1306.

[55] A. Gangrade, B.B. Mandal, Injectable Carbon Nanotube Impregnated Silk Based Multifunctional Hydrogel for Localized Targeted and On-Demand Anticancer Drug Delivery, ACS Biomaterials Science & Engineering 5(5) (2019) 2365-2381.

[56] G. Janani, M. Kumar, D. Chouhan, J.C. Moses, A. Gangrade, S. Bhattacharjee, B.B. Mandal, Insight into Silk-Based Biomaterials: From Physicochemical Attributes to Recent Biomedical Applications, ACS Applied Bio Materials (2019).

[57] R. Konwarh, B.K. Bhunia, B.B. Mandal, Opportunities and Challenges in Exploring Indian Nonmulberry Silk for Biomedical Applications, Proceedings of the Indian National Science Academy 83(1) (2017).

[58] C. Cheng, I. Teasdale, O. Brüggemann, Stimuli-Responsive Capsules Prepared from Regenerated Silk Fibroin Microspheres, Macromolecular bioscience 14(6) (2014) 807-816.

[59] M. Srisa-Ard, Y. Baimark, Controlling conformational transition of silk fibroin microspheres by water vapor for controlled release drug delivery, Particulate Science and Technology 31(4) (2013) 379-384.

[60] A.S. Lammel, X. Hu, S.-H. Park, D.L. Kaplan, T.R. Scheibel, Controlling silk fibroin particle features for drug delivery, Biomaterials 31(16) (2010) 4583-4591.

[61] J. Wang, Z. Yin, X. Xue, S.C. Kundu, X. Mo, S. Lu, Natural Non-Mulberry Silk Nanoparticles for Potential-Controlled Drug Release, International Journal of Molecular Sciences 17(12) (2016) 2012.

[62] C. Holland, K. Numata, J. Rnjak-Kovacina, F.P.J.A.h.m. Seib, The biomedical use of silk: past, present, future, 8(1) (2019).

[63] T. Yucel, M.L. Lovett, D.L. Kaplan, Silk-based biomaterials for sustained drug delivery, Journal of Controlled Release 190 (2014) 381-397.

[64] V. Karageorgiou, M. Tomkins, R. Fajardo, L. Meinel, B. Snyder, K. Wade, J. Chen, G. Vunjak-Novakovic, D.L. Kaplan, Porous silk fibroin 3-D scaffolds for delivery of bone morphogenetic protein-2 in vitro and in vivo, Journal of Biomedical Materials Research Part A 78(2) (2006) 324-334.

[65] Z. Ding, Z. Fan, X. Huang, Q. Lu, W. Xu, D.L. Kaplan, Silk–Hydroxyapatite Nanoscale Scaffolds with Programmable Growth Factor Delivery for Bone Repair, ACS Applied Materials & Interfaces 8(37) (2016) 24463-24470.

[66] B. Yavuz, J.L. Morgan, C. Herrera, K. Harrington, B. Perez-Ramirez, P.J. LiWang, D.L. Kaplan, Sustained release silk fibroin discs: Antibody and protein delivery for HIV prevention, Journal of Controlled Release 301 (2019) 1-12.

[67] B. Yavuz, J. Zeki, J. Taylor, K. Harrington, J.M. Coburn, N. Ikegaki, D.L. Kaplan, B. Chiu, Silk Reservoirs for Local Delivery of Cisplatin for Neuroblastoma Treatment: In Vitro and In Vivo Evaluations, Journal of Pharmaceutical Sciences (2019).

[68] C.P. Vepari, D.L. Kaplan, Covalently immobilized enzyme gradients within three-dimensional porous scaffolds, Biotechnol Bioeng 93(6) (2006) 1130-7.

[69] B.B. Mandal, S.C. Kundu, Calcium alginate beads embedded in silk fibroin as 3D dual drug releasing scaffolds, Biomaterials 30(28) (2009) 5170-5177.

[70] A.S. Mehta, B.K. Singh, N. Singh, D. Archana, K. Snigdha, R. Harniman, S.S. Rahatekar, R. Tewari, P. Dutta, Chitosan silk-based three-dimensional scaffolds containing gentamicin-encapsulated calcium alginate beads for drug administration and blood compatibility, Journal of biomaterials applications 29(9) (2015) 1314-1325.

[71] X. Zhang, J. Zhang, B. Shi, Mesoporous bioglass/silk fibroin scaffolds as a drug delivery system: Fabrication, drug loading and release in vitro and repair calvarial defects in vivo, Journal of Wuhan University of Technology-Mater. Sci. Ed. 29(2) (2014) 401-406.

[72] Y. Zhang, N. Cheng, R. Miron, B. Shi, X. Cheng, Delivery of PDGF-B and BMP-7 by mesoporous bioglass/silk fibrin scaffolds for the repair of osteoporotic defects, Biomaterials 33(28) (2012) 6698-6708.

[73] Y. Zhang, C. Wu, T. Luo, S. Li, X. Cheng, R.J. Miron, Synthesis and inflammatory response of a novel silk fibroin scaffold containing BMP7 adenovirus for bone regeneration, Bone 51(4) (2012) 704-713.

[74] L. Uebersax, H.P. Merkle, L. Meinel, Insulin-like growth factor I releasing silk fibroin scaffolds induce chondrogenic differentiation of human mesenchymal stem cells, Journal of Controlled Release 127(1) (2008) 12-21.

[75] M. Farokhi, F. Mottaghitalab, M.A. Shokrgozar, J. Ai, J. Hadjati, M. Azami, Bio-hybrid silk fibroin/calcium phosphate/PLGA nanocomposite scaffold to control the delivery of vascular endothelial growth factor, Materials Science and Engineering C 35(1) (2014) 401-410.

[76] P. Wongpanit, H. Ueda, Y. Tabata, R. Rujiravanit, In vitro and in vivo release of basic fibroblast growth factor using a silk fibroin scaffold as delivery carrier, Journal of Biomaterials Science, Polymer Edition 21(11) (2010) 1403-1419.

[77] S. Lu, X. Wang, Q. Lv, X. Hu, N. Uppal, F. Omenetto, D.L. Kaplan, Stabilization of Enzymes in Silk Films, Biomacromolecules 10(5) (2009) 1032-1042.

[78] J. Zhou, B. Zhang, X. Liu, L. Shi, J. Zhu, D. Wei, J. Zhong, G. Sun, D. He, Facile method to prepare silk fibroin/hyaluronic acid films for vascular endothelial growth factor release, Carbohydrate Polymers 143 (2016) 301-309.

[79] R. Jeencham, W. Tiyaboonchai, M. Sutheerawattananonda, P-025 - Preliminary study of blended silk fibroin for contact lens-based ophthalmic drug delivery, Asian Journal of Pharmaceutical Sciences 11(1) (2016) 136-137.

[80] J.M. Coburn, E. Na, D.L. Kaplan, Modulation of vincristine and doxorubicin binding and release from silk films, Journal of Controlled Release 220, Part A (2015) 229-238.

[81] F.P. Seib, J. Coburn, I. Konrad, N. Klebanov, G.T. Jones, B. Blackwood, A. Charest, D.L. Kaplan, B. Chiu, Focal therapy of neuroblastoma using silk films to deliver kinase and chemotherapeutic agents in vivo, Acta Biomaterialia 20 (2015) 32-38.

[82] A.M. Alam, Q.T. Shubhra, Surface modified thin film from silk and gelatin for sustained drug release to heal wound, Journal of Materials Chemistry B 3(31) (2015) 6473-6479.

[83] J. Zhou, B. Zhang, L. Shi, J. Zhong, J. Zhu, J. Yan, P. Wang, C. Cao, D. He, Regenerated Silk Fibroin Films with Controllable Nanostructure Size and Secondary Structure for Drug Delivery, ACS Applied Materials & Interfaces 6(24) (2014) 21813-21821.

[84] Y. Srisuwan, Y. Baimark, Preparation of Biodegradable Silk Fibroin/Alginate Blend Films for Controlled Release of Antimicrobial Drugs, Advances in Materials Science and Engineering 2013 (2013) 6.

[85] E.M. Pritchard, X. Hu, V. Finley, C.K. Kuo, D.L. Kaplan, Effect of silk protein processing on drug delivery from silk films, Macromolecular bioscience 13(3) (2013) 311-320.

[86] A.L. Laiva, J.R. Venugopal, P. Karuppuswamy, B. Navaneethan, A. Gora, S. Ramakrishna, Controlled release of titanocene into the hybrid nanofibrous scaffolds to prevent the proliferation of breast cancer cells, International Journal of Pharmaceutics 483(1-2) (2015) 115-123.

[87] W. Zhu, C. Feng, X. Zhang, Q. Fu, L. Song, R. Chen, The use of vascular endothelial growth factor with silk fibroin scaffolds and bladder acellular matrix grafts to support bladder reconstruction in rabbit model, Journal of Biomaterials and Tissue Engineering 6(6) (2016) 493-499.

[88] M. Xie, D. Fan, Y. Chen, Z. Zhao, X. He, G. Li, A. Chen, X. Wu, J. Li, Z. Li, J.A. Hunt, Y. Li, P. Lan, An implantable and controlled drug-release silk fibroin nanofibrous matrix to advance the treatment of solid tumour cancers, Biomaterials 103 (2016) 33-43.

[89] M. Xie, Y. Li, Z. Zhao, A. Chen, J. Li, Z. Li, G. Li, X. Lin, Development of silk fibroin-derived nanofibrous drug delivery system in supercritical CO2, Materials Letters 167 (2016) 175-178.

[90] W. Liu, Y. Wang, J. Yao, Z. Shao, X. Chen, Tamoxifen-loaded silk fibroin electrospun fibers, Materials Letters 178 (2016) 31-34.

[91] M. Safdari, E. Shakiba, S.H. Kiaie, A. Fattahi, Preparation and characterization of Ceftazidime loaded electrospun silk fibroin/gelatin mat for wound dressing, Fibers and Polymers 17(5) (2016) 744-750.

[92] S. Calamak, E.A. Aksoy, N. Ertas, C. Erdogdu, M. Sagıroglu, K. Ulubayram, Ag/silk fibroin nanofibers: Effect of fibroin morphology on Ag+ release and antibacterial activity, European Polymer Journal 67 (2015) 99-112.

[93] W. Chen, D. Li, A. Ei-Shanshory, M. El-Newehy, H.A. Ei-Hamshary, S.S. Al-Deyab, C. He, X. Mo, Dexamethasone loaded core–shell SF/PEO nanofibers via green electrospinning reduced endothelial cells inflammatory damage, Colloids and Surfaces B: Biointerfaces 126 (2015) 561-568.

[94] J.M. Grasman, M.P. O'Brien, K. Ackerman, K.A. Gagnon, G.M. Wong, G.D. Pins, The Effect of Sterilization Methods on the Structural and Chemical Properties of Fibrin Microthread Scaffolds, Macromolecular bioscience (2016).

[95] J.C. Moses, S.K. Nandi, B.B. Mandal, Multifunctional Cell Instructive Silk-Bioactive Glass Composite Reinforced Scaffolds Toward Osteoinductive, Proangiogenic, and Resorbable Bone Grafts, Advanced Healthcare Materials 7(10) (2018) 1701418.

[96] G. Janani, S.K. Nandi, B.B. Mandal, Functional hepatocyte clusters on bioactive blend silk matrices towards generating bioartificial liver constructs, Acta Biomaterialia 67 (2018) 167-182.

[97] L.S. Wray, X. Hu, J. Gallego, I. Georgakoudi, F.G. Omenetto, D. Schmidt, D.L. Kaplan, Effect of processing on silk-based biomaterials: Reproducibility and biocompatibility, Journal of Biomedical Materials Research Part B: Applied Biomaterials 99(1) (2011) 89-101.

[98] P.N. Atterberry, T.J. Roark, S.Y. Severt, M.L. Schiller, J.M. Antos, A.R. Murphy, Sustained Delivery of Chemokine CXCL12 from Chemically Modified Silk Hydrogels, Biomacromolecules 16(5) (2015) 1582-1589.

[99] M.A. de Moraes, A. Mahl, C. Regina, M. Ferreira Silva, M.M. Beppu, Formation of silk fibroin hydrogel and evaluation of its drug release profile, Journal of Applied Polymer Science 132(15) (2015).

[100] J. Wu, A. Chen, M. Qin, R. Huang, G. Zhang, B. Xue, J. Wei, Y. Li, Y. Cao, W. Wang, Hierarchical construction of a mechanically stable peptide–graphene oxide hybrid hydrogel for drug delivery and pulsatile triggered release in vivo, Nanoscale 7(5) (2015) 1655-1660.

[101] H. Wu, J. Liu, J. Wu, Y. Wan, Y. Chen, Controlled delivery of platelet-derived growth factor-BB from injectable microsphere/hydrogel composites, Colloids and Surfaces B: Biointerfaces 148 (2016) 308-316.

[102] D. Ma, G. An, M. Liang, Y. Liu, B. Zhang, Y. Wang, A composited PEG-silk hydrogel combining with polymeric particles delivering rhBMP-2 for bone regeneration, Materials Science and Engineering: C 65 (2016) 221-231.

[103] D. Yu, C. Sun, Z. Zheng, X. Wang, D. Chen, H. Wu, X. Wang, F. Shi, Inner ear delivery of dexamethasone using injectable silk-polyethylene glycol (PEG) hydrogel, International journal of pharmaceutics 503(1) (2016) 229-237.

[104] H. Wu, S. Liu, L. Xiao, X. Dong, Q. Lu, D.L. Kaplan, Injectable and pH-responsive silk nanofiber hydrogels for sustained anticancer drug delivery, ACS applied materials & interfaces 8(27) (2016) 17118-17126.

[105] M.L. Lovett, X. Wang, T. Yucel, L. York, M. Keirstead, L. Haggerty, D.L. Kaplan, Silk hydrogels for sustained ocular delivery of anti-vascular endothelial growth factor (anti-VEGF) therapeutics, European Journal of Pharmaceutics and Biopharmaceutics 95, Part B (2015) 271-278.

[106] T. Zhong, Z. Jiang, P. Wang, S. Bie, F. Zhang, B. Zuo, Silk fibroin/copolymer composite hydrogels for the controlled and sustained release of hydrophobic/hydrophilic drugs, International Journal of Pharmaceutics 494(1) (2015) 264-270.

[107] J. Wang, G.J. Li, R. Jiang, Z.P. Yin, S.Z. Lu, Antheraea pernyi Silk Fibroin Microspheres Carried Lysozyme, Advanced Materials Research, Trans Tech Publ, 2014, pp. 875-878.

[108] J. Wang, S. Zhang, T. Xing, B. Kundu, M. Li, S.C. Kundu, S. Lu, Ion-induced fabrication of silk fibroin nanoparticles from Chinese oak tasar Antheraea pernyi, International Journal of Biological Macromolecules 79 (2015) 316-325.

[109] Y. Liu, R. You, G. Liu, X. Li, W. Sheng, J. Yang, M. Li, Antheraea pernyi silk fibroin-coated PEI/DNA complexes for targeted gene delivery in HEK 293 and HCT 116 cells, International Journal of Molecular Sciences 15(5) (2014) 7049-7063.

[110] P.C. Bessa, E.R. Balmayor, H.S. Azevedo, S. Nürnberger, M. Casal, M. Van Griensven, R. Reis, H. Redl, Silk fibroin microparticles as carriers for delivery of human recombinant BMPs. Physical characterization and drug release, Journal of tissue engineering and regenerative medicine 4(5) (2010) 349-355.

[111] S. Sharma, S. Bano, A.S. Ghosh, M. Mandal, H.-W. Kim, T. Dey, S.C. Kundu, Silk fibroin nanoparticles support in vitro sustained antibiotic release and osteogenesis on titanium surface, Nanomedicine: Nanotechnology, Biology and Medicine 12(5) (2016) 1193-1204.

[112] L. Tan, T. Jiang, X. Yang, W. Li, L. Pan, M. Yu, Core–shell biopolymer microspheres for sustained drug release, Journal of Applied Polymer Science 132(14) (2015).

[113] J.C. Moses, A. Gangrade, B.B. Mandal, Carbon Nanotubes and Their Polymer Nanocomposites, Nanomaterials and Polymer Nanocomposites, Elsevier2019, pp. 145-175.

[114] M. Karimi, P. Sahandi Zangabad, S. Baghaee-Ravari, M. Ghazadeh, H. Mirshekari, M.R. Hamblin, Smart nanostructures for cargo delivery: uncaging and activating by light, Journal of the American Chemical Society 139(13) (2017) 4584-4610.

[115] P.K. Bolla, V.A. Rodriguez, R.S. Kalhapure, J. Renukuntla, A review on pH and temperature responsive gels and other less explored drug delivery systems, Journal of Drug Delivery Science and Technology (2018).

[116] D. Mertz, O. Sandre, S. Begin-Colin, Drug releasing nanoplatforms activated by alternating magnetic fields, Biochimica et Biophysica Acta (BBA)-General Subjects 1861(6) (2017) 1617-1641.

[117] N. Poorgholy, B. Massoumi, M. Ghorbani, M. Jaymand, H. Hamishehkar, Intelligent anticancer drug delivery performances of two poly (N-isopropylacrylamide)-based magnetite nanohydrogels, Drug development and industrial pharmacy (2018) 1-8.

[118] F. Wu, M. Zhang, H. Lu, D. Liang, Y. Huang, Y. Xia, Y. Hu, S. Hu, J. Wang, X. Yi, Triple Stimuli-Responsive Magnetic Hollow Porous Carbon-Based Nano-Drug Delivery System for Magnetic Resonance Imaging-Guided Synergistic Photothermal/Chemo-Therapy of Cancer, ACS applied materials & interfaces (2018).

[119] S.A. Shah, M.A. Khan, M. Arshad, S. Awan, M. Hashmi, N. Ahmad, Doxorubicin-loaded photosensitive magnetic liposomes for multi-modal cancer therapy, Colloids and Surfaces B: Biointerfaces 148 (2016) 157-164.

[120] H. Nosrati, A. Mojtahedi, H. Danafar, H. Kheiri Manjili, Enzymatic stimuli-responsive methotrexate-conjugated magnetic nanoparticles for target delivery to breast cancer cells and release study in lysosomal condition, Journal of Biomedical Materials Research Part A 106(6) (2018) 1646-1654.

[121] S. Sengupta, C. Khatua, V.K. Balla, In Vitro Carcinoma Treatment Using Magnetic Nanocarriers under Ultrasound and Magnetic Fields, ACS Omega 3(5) (2018) 5459-5469.

[122] F. Neri, A. Scala, S. Grimato, M. Santoro, S. Spadaro, F. Barreca, F. Cimino, A. Speciale, A. Saija, G. Grassi, Biocompatible silver nanoparticles embedded in a PEG–PLA polymeric matrix for stimulated laser light drug release, Journal of Nanoparticle Research 18(6) (2016) 153.

[123] S. Lee, G. Hwang, T.H. Kim, S.J. Kwon, J.U. Kim, K. Koh, B. Park, H. Hong, K.J. Yu, H. Chae, On-Demand Drug Release from Gold Nanoturf for a Thermo-& Chemo-Therapeutic Esophageal Stent (TES), ACS nano (2018).

[124] A.P. Tiwari, T.I. Hwang, J.-M. Oh, B. Maharjan, S. Chun, B.S. Kim, M.K.K. Joshi, C.H. Park, C.S. Kim, pH/NIR-Responsive Polypyrrole Functionalized Fibrous Localized Drug Delivery Platform for Synergistic Cancer Therapy, ACS applied materials & interfaces (2018).

[125] Y. Jing, A. Danielsson, H.D. Trefná, M. Persson, S. Svedhem, Asymmetric cationic liposomes designed for heat-activated association with cells, Colloids and Surfaces B: Biointerfaces 151 (2017) 112-118.

[126] M. Foldvari, M. Bagonluri, Carbon nanotubes as functional excipients for nanomedicines: II. Drug delivery and biocompatibility issues, Nanomedicine: Nanotechnology, Biology and Medicine 4(3) (2008) 183-200.

[127] H. Huang, Q. Yuan, J. Shah, R. Misra, A new family of folate-decorated and carbon nanotube-mediated drug delivery system: synthesis and drug delivery response, Advanced drug delivery reviews 63(14) (2011) 1332-1339.

[128] N.W. Shi Kam, T.C. Jessop, P.A. Wender, H. Dai, Nanotube molecular transporters: internalization of carbon nanotube− protein conjugates into mammalian cells, Journal of the American Chemical Society 126(22) (2004) 6850-6851.

[129] M. Munk, L.O. Ladeira, B.C. Carvalho, L.S. Camargo, N.R. Raposo, R.V. Serapião, C.C. Quintão, S.R. Silva, J.S. Soares, A. Jorio, Efficient delivery of DNA into bovine preimplantation embryos by multiwall carbon nanotubes, Scientific reports 6 (2016).

[130] N.K. Mehra, S. Palakurthi, Interactions between carbon nanotubes and bioactives: a drug delivery perspective, Drug discovery today 21(4) (2016) 585-597.

[131] Z. Liu, J.T. Robinson, S.M. Tabakman, K. Yang, H. Dai, Carbon materials for drug delivery & cancer therapy, Materials today 14(7) (2011) 316-323.

[132] Z. Liu, K. Chen, C. Davis, S. Sherlock, Q. Cao, X. Chen, H. Dai, Drug delivery with carbon nanotubes for in vivo cancer treatment, Cancer research 68(16) (2008) 6652-6660.

[133] N.W.S. Kam, M. O'Connell, J.A. Wisdom, H. Dai, Carbon nanotubes as multifunctional biological transporters and near-infrared agents for selective cancer cell destruction, Proceedings of the National Academy of Sciences of the United States of America 102(33) (2005) 11600-11605.

[134] H.K. Moon, S.H. Lee, H.C. Choi, In vivo near-infrared mediated tumor destruction by photothermal effect of carbon nanotubes, ACS nano 3(11) (2009) 3707-3713.

[135] V.E. Kagan, N.V. Konduru, W. Feng, B.L. Allen, J. Conroy, Y. Volkov, I.I. Vlasova, N.A. Belikova, N. Yanamala, A. Kapralov, Carbon nanotubes degraded by neutrophil myeloperoxidase induce less pulmonary inflammation, Nature nanotechnology 5(5) (2010) 354.

[136] H. Hu, Y. Ni, V. Montana, R.C. Haddon, V. Parpura, Chemically functionalized carbon nanotubes as substrates for neuronal growth, Nano letters 4(3) (2004) 507-511.

[137] F. Zhang, A. Weidmann, J.B. Nebe, E. Burkel, Osteoblast cell response to surface-modified carbon nanotubes, Materials Science and Engineering: C 32(5) (2012) 1057-1061.

[138] O.J. Yoon, H.J. Lee, Y.M. Jang, H.W. Kim, W.B. Lee, S.S. Kim, N.-E. Lee, Effects of O2 and N2/H2 plasma treatments on the neuronal cell growth on single-walled carbon nanotube paper scaffolds, Applied Surface Science 257(20) (2011) 8535-8541.

[139] D.W. Porter, A.F. Hubbs, R.R. Mercer, N. Wu, M.G. Wolfarth, K. Sriram, S. Leonard, L. Battelli, D. Schwegler-Berry, S. Friend, Mouse pulmonary dose-and time course-responses induced by exposure to multi-walled carbon nanotubes, Toxicology 269(2-3) (2010) 136-147.

[140] X. Deng, F. Wu, Z. Liu, M. Luo, L. Li, Q. Ni, Z. Jiao, M. Wu, Y. Liu, The splenic toxicity of water soluble multi-walled carbon nanotubes in mice, Carbon 47(6) (2009) 1421-1428.

[141] A. Patlolla, B. McGinnis, P. Tchounwou, Biochemical and histopathological evaluation of functionalized single-walled carbon nanotubes in Swiss–Webster mice, Journal of Applied Toxicology 31(1) (2011) 75-83.

[142] A. Pietroiusti, M. Massimiani, I. Fenoglio, M. Colonna, F. Valentini, G. Palleschi, A. Camaioni, A. Magrini, G. Siracusa, A. Bergamaschi, Low doses of pristine and oxidized single-wall carbon nanotubes affect mammalian embryonic development, ACS nano 5(6) (2011) 4624-4633.

[143] V. Biju, Chemical modifications and bioconjugate reactions of nanomaterials for sensing, imaging, drug delivery and therapy, Chemical Society Reviews 43(3) (2014) 744-764.

[144] M. Zhou, S. Liu, Y. Jiang, H. Ma, M. Shi, Q. Wang, W. Zhong, W. Liao, M.M. Xing, Doxorubicin-Loaded Single Wall Nanotube Thermo-Sensitive Hydrogel for Gastric Cancer Chemo-Photothermal Therapy, Advanced functional materials 25(29) (2015) 4730-4739.

[145] C.M. Homenick, H. Sheardown, A. Adronov, Reinforcement of collagen with covalently-functionalized single-walled carbon nanotube crosslinkers, Journal of Materials Chemistry 20(14) (2010) 2887-2894.

[146] T. Ogoshi, Y. Takashima, H. Yamaguchi, A. Harada, Chemically-responsive sol−gel transition of supramolecular single-walled carbon nanotubes (SWNTs) hydrogel made by hybrids of SWNTs and cyclodextrins, Journal of the American Chemical Society 129(16) (2007) 4878-4879.

[147] M.L. Schipper, N. Nakayama-Ratchford, C.R. Davis, N.W.S. Kam, P. Chu, Z. Liu, X. Sun, H. Dai, S.S. Gambhir, A pilot toxicology study of single-walled carbon nanotubes in a small sample of mice, Nature nanotechnology 3(4) (2008) 216.

[148] J. Cheng, K.S. Fernando, L.M. Veca, Y.-P. Sun, A.I. Lamond, Y.W. Lam, S.H. Cheng, Reversible accumulation of PEGylated single-walled carbon nanotubes in the mammalian nucleus, ACS nano 2(10) (2008) 2085-2094.

[149] L. Niu, L. Meng, Q. Lu, Folate-Conjugated PEG on single walled carbon nanotubes for targeting delivery of doxorubicin to cancer cells, Macromolecular bioscience 13(6) (2013) 735-744.

[150] R. Bellingeri, F. Alustiza, N. Picco, D. Acevedo, M.A. Molina, R. Rivero, C. Grosso, C. Motta, C. Barbero, A. Vivas, In vitro toxicity evaluation of hydrogel–carbon nanotubes composites on intestinal cells, Journal of applied polymer science 132(5) (2015).

[151] A.R. Karimi, M. Tarighatjoo, G. Nikravesh, 1, 3, 5-Triazine-2, 4, 6-tribenzaldehyde derivative as a new crosslinking agent for synthesis of pH-thermo dual responsive chitosan hydrogels and their nanocomposites: Swelling properties and drug release behavior, International journal of biological macromolecules 105 (2017) 1088-1095.

[152] G. Cirillo, M. Curcio, O. Vittorio, U.G. Spizzirri, F.P. Nicoletta, N. Picci, S. Hampel, F. Iemma, Dual Stimuli Responsive Gelatin-CNT Hybrid Films as a Versatile Tool for the Delivery of Anionic Drugs, Macromolecular Materials and Engineering 301(12) (2016) 1537-1547.

[153] C. Min, X. Zou, Q. Yang, L. Liao, G. Zhou, L. Liu, Near-infrared light responsive polymeric nanocomposites for cancer therapy, Current topics in medicinal chemistry 17(16) (2017) 1805-1814.

[154] X. Dong, C. Wei, J. Liang, T. Liu, D. Kong, F. Lv, Thermosensitive hydrogel loaded with chitosan-carbon nanotubes for near infrared light triggered drug delivery, Colloids and Surfaces B: Biointerfaces 154 (2017) 253-262.

[155] H. Zhang, X. Zhu, Y. Ji, X. Jiao, Q. Chen, L. Hou, H. Zhang, Z. Zhang, Near-infrared-triggered in situ hybrid hydrogel system for synergistic cancer therapy, Journal of Materials Chemistry B 3(30) (2015) 6310-6326.

[156] Z. Sun, C. Song, C. Wang, Y. Hu, J. Wu, Hydrogel-based controlled drug delivery for cancer treatment: a review, Molecular Pharmaceutics (2019).

[157] M.C. Scicluna, L. Vella-Zarb, The Evolution of Nanocarrier Drug-Delivery Systems and Recent Advancements in Covalent Organic Framework-Drug Systems, ACS Applied Nano Materials (2020).

[158] W.J. Yang, P. Zhou, L. Liang, Y. Cao, J. Qiao, X. Li, Z. Teng, L. Wang, Nanogel-incorporated injectable hydrogel for synergistic therapy based on sequential local delivery of combretastatin-A4 phosphate (CA4P) and doxorubicin (DOX), ACS applied materials & interfaces 10(22) (2018) 18560-18573.

[159] A. Gangrade, B. Gawali, P.K. Jadi, V.G. Naidu, B.B. Mandal, Photo-Electro Active Nanocomposite Silk Hydrogel for Spatiotemporal Controlled Release of

Chemotherapeutics: An In Vivo Approach Towards Suppressing Solid Tumor Growth, ACS Applied Materials & Interfaces (2020).

[160] F. Mottaghitalab, M. Farokhi, M.A. Shokrgozar, F. Atyabi, H. Hosseinkhani, Silk fibroin nanoparticle as a novel drug delivery system, Journal of Controlled Release 206 (2015) 161-176.

[161] H. Wu, S. Liu, L. Xiao, X. Dong, Q. Lu, D.L. Kaplan, Injectable and pH-Responsive Silk Nanofiber Hydrogels for Sustained Anticancer Drug Delivery, ACS Appl. Mater. Interfaces 8(27) (2016) 17118-17126.

[162] B. Yavuz, J. Zeki, J. Taylor, K. Harrington, J.M. Coburn, N. Ikegaki, D.L. Kaplan, B. Chiu, Silk reservoirs for local delivery of cisplatin for neuroblastoma treatment: in vitro and in vivo evaluations, Journal of pharmaceutical sciences 108(8) (2019) 2748-2755.

[163] M.G. Montalbán, S. Chakraborty, J. Peña-García, H. Verli, G. Villora, H. Pérez-Sánchez, F.G. Díaz-Baños, Molecular insight into silk fibroin based delivery vehicle for amphiphilic drugs: Synthesis, characterization and molecular dynamics studies, Journal of Molecular Liquids 299 (2020) 112156.

[164] G. Janani, M. Kumar, D. Chouhan, J.C. Moses, A. Gangrade, S. Bhattacharjee, B.B. Mandal, Insight into Silk-Based Biomaterials: From Physicochemical Attributes to Recent Biomedical Applications, ACS Applied Bio Materials 2(12) (2019) 5460-5491.

[165] Z. Xu, L. Shi, M. Yang, L. Zhu, Preparation and biomedical applications of silk fibroin-nanoparticles composites with enhanced properties - A review, Materials Science and Engineering: C 95 (2019) 302-311.

[166] O. Gianak, G.Z. Kyzas, V.F. Samanidou, E.A. Deliyanni, A review for the synthesis of silk fibroin nanoparticles with different techniques and their ability to be used for drug delivery, Current Analytical Chemistry 15(4) (2019) 339-348.

[167] B.K. Bhunia, B.B. Mandal, Exploring gelation and physicochemical behavior of in situ bioresponsive silk hydrogels for disc degeneration therapy, ACS Biomaterials Science & Engineering 5(2) (2018) 870-886.

[168] M. Floren, C. Migliaresi, A. Motta, Processing techniques and applications of silk hydrogels in bioengineering, Journal of functional biomaterials 7(3) (2016) 26.

[169] N. Bhardwaj, Y.P. Singh, B.B. Mandal, Silk Fibroin Scaffold-Based 3D Co-Culture Model for Modulation of Chondrogenesis without Hypertrophy via Reciprocal Cross-talk and Paracrine Signaling, ACS Biomaterials Science & Engineering (2019).

[170] J.C. Moses, T. Saha, B.B. Mandal, Chondroprotective and osteogenic effects of silk-based bioinks in developing 3D bioprinted osteochondral interface, Bioprinting 17 (2020) e00067.

[171] M. Kumar, P. Gupta, S. Bhattacharjee, S.K. Nandi, B.B. Mandal, Immunomodulatory injectable silk hydrogels maintaining functional islets and promoting anti-inflammatory M2 macrophage polarization, Biomaterials 187 (2018) 1-17.

[172] S. Mehrotra, B.A.G. Melo, M. Hirano, W. Keung, R.A. Li, B.B. Mandal, S.R. Shin, Nonmulberry Silk Based Ink for Fabricating Mechanically Robust Cardiac Patches and Endothelialized Myocardium-on-a-Chip Application, Advanced Functional Materials 30(12) (2020) 1907436.

[173] E. Dondajewska, W. Juzwa, A. Mackiewicz, H. Dams-Kozlowska, Heterotypic breast cancer model based on a silk fibroin scaffold to study the tumor microenvironment, Oncotarget 9(4) (2018) 4935-4950.

[174] J.P. Kumar, R. Konwarh, M. Kumar, A. Gangrade, B.B. Mandal, Potential nanomedicine applications of multifunctional carbon nanoparticles developed using green technology, ACS Sustainable Chemistry & Engineering 6(1) (2018) 1235-1245.

[175] Q. Sun, S.H. Tan, Q. Chen, R. Ran, Y. Hui, D. Chen, C.-X. Zhao, Microfluidic formation of coculture tumor spheroids with stromal cells as a novel 3D tumor model for drug testing, ACS Biomaterials Science & Engineering 4(12) (2018) 4425-4433.

[176] J. Li, Y. Zhou, W. Chen, Z. Yuan, B. You, Y. Liu, S. Yang, F. Li, C. Qu, X. Zhang, A novel 3D in vitro tumor model based on silk fibroin/chitosan scaffolds to mimic the tumor microenvironment, ACS applied materials & interfaces 10(43) (2018) 36641-36651.

[177] K. Wang, F.M. Kievit, S.J. Florczyk, Z.R. Stephen, M. Zhang, 3D porous chitosan–alginate scaffolds as an in vitro model for evaluating nanoparticle-mediated tumor targeting and gene delivery to prostate cancer, Biomacromolecules 16(10) (2015) 3362-3372.

[178] X. Song, Z. Zhang, J. Zhu, Y. Wen, F. Zhao, L. Lei, N. Phan-Thien, B.C. Khoo, J. Li, Thermoresponsive Hydrogel Induced by Dual Supramolecular Assemblies and Its Controlled Release Property for Enhanced Anticancer Drug Delivery, Biomacromolecules (2020).

[179] I. Takeuchi, Y. Shimamura, Y. Kakami, T. Kameda, K. Hattori, S. Miura, H. Shirai, M. Okumura, T. Inagi, H. Terada, Transdermal delivery of 40-nm silk fibroin nanoparticles, Colloids and Surfaces B: Biointerfaces 175 (2019) 564-568.

[180] S. Bhowmick, A. Jana, K. Singh, P. Gupta, A. Gangrade, B.B. Mandal, N. Das, Coordination-driven self-assembly of ionic irregular hexagonal metallamacrocycles via an organometallic clip and their cytotoxicity potency, Inorganic chemistry 57(7) (2017) 3615-3625.

[181] J. Coates, Interpretation of infrared spectra, a practical approach, Encyclopedia of analytical chemistry: applications, theory and instrumentation (2006).

[182] J. Qu, Y. Liu, Y. Yu, J. Li, J. Luo, M. Li, Silk fibroin nanoparticles prepared by electrospray as controlled release carriers of cisplatin, Materials Science and Engineering: C 44 (2014) 166-174.

[183] L. Qi, Q. Luo, Y. Zhang, F. Jia, Y. Zhao, F. Wang, Advances in Toxicological Research of the Anticancer Drug Cisplatin, Chemical research in toxicology 32(8) (2019) 1469-1486.

[184] T. Boulikas, M. Vougiouka, Recent clinical trials using cisplatin, carboplatin and their combination chemotherapy drugs, Oncology reports 11(3) (2004) 559-595.

[185] G. Mandriota, R. Di Corato, M. Benedetti, F. De Castro, F.P. Fanizzi, R. Rinaldi, Design and application of cisplatin-loaded magnetic nanoparticle clusters for smart chemotherapy, ACS applied materials & interfaces 11(2) (2018) 1864-1875.

[186] S.H. Alavizadeh, F. Gheybi, A.R. Nikpoor, A. Badiee, S. Golmohammadzadeh, M.R. Jaafari, Therapeutic efficacy of cisplatin thermosensitive liposomes upon mild hyperthermia in C26 tumor bearing BALB/c mice, Molecular pharmaceutics 14(3) (2017) 712-721.

[187] B. Subia, T. Dey, S. Sharma, S.C. Kundu, Target Specific Delivery of Anticancer Drug in Silk Fibroin Based 3D Distribution Model of Bone–Breast Cancer Cells, 7(4) (2015) 2269-2279.

[188] M.F. Gencoglu, L.E. Barney, C.L. Hall, E.A. Brooks, A.D. Schwartz, D.C. Corbett, K.R. Stevens, S.R. Peyton, Comparative study of multicellular tumor spheroid formation methods and implications for drug screening, ACS biomaterials science & engineering 4(2) (2018) 410-420.

[189] Y.P. Singh, J.C. Moses, N. Bhardwaj, B.B. Mandal, Injectable hydrogels: a new paradigm for osteochondral tissue engineering, Journal of Materials Chemistry B 6(35) (2018) 5499-5529.

[190] Q. Li, J. Wen, C. Liu, Y. Jia, Y. Wu, Y. Shan, Z. Qian, J. Liao, Graphene-nanoparticle-based self-healing hydrogel in preventing postoperative recurrence of breast cancer, ACS Biomaterials Science & Engineering 5(2) (2019) 768-779.

[191] Y. Qi, H. Min, A. Mujeeb, Y. Zhang, X. Han, X. Zhao, G.J. Anderson, Y. Zhao, G. Nie, Injectable hexapeptide hydrogel for localized chemotherapy prevents breast cancer recurrence, ACS applied materials & interfaces 10(8) (2018) 6972-6981.

[192] Y.P. Jia, K. Shi, F. Yang, J.F. Liao, R.X. Han, L.P. Yuan, Y. Hao, M. Pan, Y. Xiao, Z.Y. Qian, Multifunctional Nanoparticle Loaded Injectable Thermoresponsive Hydrogel as NIR Controlled Release Platform for Local Photothermal Immunotherapy to Prevent Breast Cancer Postoperative Recurrence and Metastases, Advanced Functional Materials (2020) 2001059.

[193] B. Zhuang, T. Chen, Z. Xiao, Y. Jin, Drug-loaded implantable surgical cavity-adaptive hydrogels for prevention of local tumor recurrence, International Journal of Pharmaceutics 577 (2020) 119048.

[194] F.P. Seib, E.M. Pritchard, D.L. Kaplan, Self-Assembling Doxorubicin Silk Hydrogels for the Focal Treatment of Primary Breast Cancer, Advanced functional materials 23(1) (2013) 58-65.

[195] R. Dikshit, P.C. Gupta, C. Ramasundarahettige, V. Gajalakshmi, L. Aleksandrowicz, R. Badwe, R. Kumar, S. Roy, W. Suraweera, F. Bray, Cancer mortality in India: a nationally representative survey, The Lancet 379(9828) (2012) 1807-1816.

[196] F. Song, X. Li, Q. Wang, L. Liao, C. Zhang, Nanocomposite hydrogels and their applications in drug delivery and tissue engineering, Journal of biomedical nanotechnology 11(1) (2015) 40-52.

[197] B.B. Mandal, S. Kapoor, S.C. Kundu, Silk fibroin/polyacrylamide semi-interpenetrating network hydrogels for controlled drug release, Biomaterials 30(14) (2009) 2826-2836.

[198] J. Shi, A.R. Votruba, O.C. Farokhzad, R. Langer, Nanotechnology in drug delivery and tissue engineering: from discovery to applications, Nano letters 10(9) (2010) 3223-3230.

[199] T.R. Hoare, D.S. Kohane, Hydrogels in drug delivery: progress and challenges, Polymer 49(8) (2008) 1993-2007.

[200] C. Vepari, D.L. Kaplan, Silk as a biomaterial, Progress in polymer science 32(8-9) (2007) 991-1007.

[201] R. Konwarh, P. Gupta, B.B. Mandal, Silk-microfluidics for advanced biotechnological applications: A progressive review, Biotechnology advances 34(5) (2016) 845-858.

[202] R. Konwarh, B.K. Bhunia, B.B. Mandal, Opportunities and Challenges in Exploring Indian Non-mulberry Silk for Biomedical Applications, Proceedings of the Indian National Science Academy 83(1) (2017) 85-101.

[203] B.B. Mandal, S.C. Kundu, Non-bioengineered silk gland fibroin protein: Characterization and evaluation of matrices for potential tissue engineering applications, Biotechnology and bioengineering 100(6) (2008) 1237-1250.

[204] B.B. Mandal, J.K. Mann, S. Kundu, Silk fibroin/gelatin multilayered films as a model system for controlled drug release, European Journal of Pharmaceutical Sciences 37(2) (2009) 160-171.

[205] D.N. Rockwood, R.C. Preda, T. Yücel, X. Wang, M.L. Lovett, D.L. Kaplan, Materials fabrication from Bombyx mori silk fibroin, Nature protocols 6(10) (2011).

[206] T. Yucel, P. Cebe, D.L. Kaplan, Vortex-induced injectable silk fibroin hydrogels, Biophysical journal 97(7) (2009) 2044-2050.

[207] N. Guziewicz, A. Best, B. Perez-Ramirez, D.L. Kaplan, Lyophilized silk fibroin hydrogels for the sustained local delivery of therapeutic monoclonal antibodies, Biomaterials 32(10) (2011) 2642-2650.

[208] W. Zhang, X. Wang, S. Wang, J. Zhao, L. Xu, C. Zhu, D. Zeng, J. Chen, Z. Zhang, D.L. Kaplan, The use of injectable sonication-induced silk hydrogel for VEGF 165 and BMP-2 delivery for elevation of the maxillary sinus floor, Biomaterials 32(35) (2011) 9415-9424.

[209] X. Wang, B. Partlow, J. Liu, Z. Zheng, B. Su, Y. Wang, D.L. Kaplan, Injectable silk-polyethylene glycol hydrogels, Acta biomaterialia 12 (2015) 51-61.

[210] E. Allard-Vannier, K. Hervé-Aubert, K. Kaaki, T. Blondy, A. Shebanova, K.V. Shaitan, A.A. Ignatova, M.-L. Saboungi, A.V. Feofanov, I. Chourpa, Folic acid-capped PEGylated magnetic nanoparticles enter cancer cells mostly via clathrin-dependent endocytosis, Biochimica et Biophysica Acta (BBA)-General Subjects (2016).

[211] J. Ledermann, S. Canevari, T. Thigpen, Targeting the folate receptor: diagnostic and therapeutic approaches to personalize cancer treatments, Annals of Oncology 26(10) (2015) 2034-2043.

[212] Z. Li, A.L.B. de Barros, D.C.F. Soares, S.N. Moss, L. Alisaraie, Functionalized Single-Walled Carbon Nanotubes: Cellular Uptake, Biodistribution and Applications in Drug Delivery, International Journal of Pharmaceutics (2017).

[213] H. Li, X. Fan, X. Chen, Near-Infrared Light Activation of Proteins Inside Living Cells Enabled by Carbon Nanotube-Mediated Intracellular Delivery, ACS applied materials & interfaces 8(7) (2016) 4500-4507.

[214] G. Cirillo, S. Hampel, U.G. Spizzirri, O.I. Parisi, N. Picci, F. Iemma, Carbon nanotubes hybrid hydrogels in drug delivery: a perspective review, BioMed research international 2014 (2014).

[215] A. Servant, L. Methven, R.P. Williams, K. Kostarelos, Electroresponsive polymer–carbon nanotube hydrogel hybrids for pulsatile drug delivery in vivo, Advanced healthcare materials 2(6) (2013) 806-811.

[216] H.J. Yao, L. Sun, Y. Liu, S. Jiang, Y. Pu, J. Li, Y. Zhang, Monodistearoylphosphatidylethanolamine-hyaluronic acid functionalization of single-walled carbon nanotubes for targeting intracellular drug delivery to overcome multidrug resistance of cancer cells, Carbon 96 (2016) 362-376.

[217] J.C. M, P.J.T. Reardon, R. Konwarh, J.C. Knowles, B.B. Mandal, Mimicking Hierarchical Complexity of the Osteochondral Interface Using Electrospun Silk–Bioactive Glass Composites, ACS applied materials & interfaces 9(9) (2017) 8000-8013.

[218] G. Janani, S.K. Nandi, B.B. Mandal, Functional hepatocyte clusters on bioactive blend silk matrices towards generating bioartificial liver constructs, Acta biomaterialia (2017).

[219] Y. Zhang, J. Li, M. Lang, X. Tang, L. Li, X. Shen, Folate-functionalized nanoparticles for controlled 5-fluorouracil delivery, Journal of Colloid and Interface Science 354(1) (2011) 202-209.

[220] J. Coates, Interpretation of infrared spectra, a practical approach, Encyclopedia of analytical chemistry (2000).

[221] H.-J. Shin, H.-K. Kwon, J.-H. Lee, X. Gui, A. Achek, J.-H. Kim, S. Choi, Doxorubicin-induced necrosis is mediated by poly-(ADP-ribose) polymerase 1 (PARP1) but is independent of p53, Scientific reports 5 (2015) 15798.

[222] K. Sugimoto, K. Tamayose, M. Sasaki, K. Hayashi, K. Oshimi, Low-dose doxorubicin-induced necrosis in Jurkat cells and its acceleration and conversion to apoptosis by antioxidants, British journal of haematology 118(1) (2002) 229-238.

[223] C. Carvalho, R.X. Santos, S. Cardoso, S. Correia, P.J. Oliveira, M.S. Santos, P.I. Moreira, Doxorubicin: the good, the bad and the ugly effect, Current medicinal chemistry 16(25) (2009) 3267-3285.

[224] B.I. Kharisov, O.V. Kharissova, A.V. Dimas, The dispersion, solubilization and stabilization in "solution" of single-walled carbon nanotubes, RSC advances 6(73) (2016) 68760-68787.

[225] H. Dumortier, S. Lacotte, G. Pastorin, R. Marega, W. Wu, D. Bonifazi, J.-P. Briand, M. Prato, S. Muller, A. Bianco, Functionalized carbon nanotubes are non-cytotoxic and preserve the functionality of primary immune cells, Nano letters 6(7) (2006) 1522-1528.

[226] S.Y. Madani, A. Mandel, A.M. Seifalian, A concise review of carbon nanotube's toxicology, Nano reviews 4(1) (2013) 21521.

[227] K. Fujita, M. Fukuda, S. Endoh, J. Maru, H. Kato, A. Nakamura, N. Shinohara, K. Uchino, K. Honda, Size effects of single-walled carbon nanotubes on in vivo and in vitro pulmonary toxicity, Inhalation toxicology 27(4) (2015) 207-223.

[228] B. Kang, S. Chang, Y. Dai, D. Yu, D. Chen, Cell Response to Carbon Nanotubes: Size-Dependent Intracellular Uptake Mechanism and Subcellular Fate, Small 6(21) (2010) 2362-2366.

[229] K.S. Munir, C. Wen, Deterioration of the Strong sp2 Carbon Network in Carbon Nanotubes during the Mechanical Dispersion Processing—A Review, Critical Reviews in Solid State and Materials Sciences 41(5) (2016) 347-366.

[230] E.o. Lepvrier, C. Doigneaux, L. Moullintraffort, A. Nazabal, C. Garnier, Optimized protocol for protein macrocomplexes stabilization using the EDC, 1-ethyl-3-(3-(dimethylamino) propyl) carbodiimide, zero-length cross-linker, Analytical chemistry 86(21) (2014) 10524-10530.

[231] X. Zhang, L. Meng, Q. Lu, Z. Fei, P.J. Dyson, Targeted delivery and controlled release of doxorubicin to cancer cells using modified single wall carbon nanotubes, Biomaterials 30(30) (2009) 6041-6047.

[232] Y. Wang, Z. Xu, Interaction mechanism of doxorubicin and SWCNT: protonation and diameter effects on drug loading and releasing, RSC advances 6(1) (2016) 314-322.

[233] A. Gupta, K. Mita, K.P. Arunkumar, J. Nagaraju, Molecular architecture of silk fibroin of Indian golden silkmoth, Antheraea assama, Scientific reports 5 (2015) 12706.

[234] S. Hämälistö, M. Jäättelä, Lysosomes in cancer—living on the edge (of the cell), Current opinion in cell biology 39 (2016) 69-76.

[235] S. Smart, A. Cassady, G. Lu, D. Martin, The biocompatibility of carbon nanotubes, Carbon 44(6) (2006) 1034-1047.

[236] X. Zhang, W. Hu, J. Li, L. Tao, Y. Wei, A comparative study of cellular uptake and cytotoxicity of multi-walled carbon nanotubes, graphene oxide, and nanodiamond, Toxicology Research 1(1) (2012) 62-68.

[237] W. Liu, L. Nie, F. Li, Z.P. Aguilar, H. Xu, Y. Xiong, F. Fu, H. Xu, Folic acid conjugated magnetic iron oxide nanoparticles for nondestructive separation and detection of ovarian cancer cells from whole blood, Biomaterials science 4(1) (2016) 159-166.

[238] B. Subia, S. Chandra, S. Talukdar, S.C. Kundu, Folate conjugated silk fibroin nanocarriers for targeted drug delivery, Integrative Biology 6(2) (2014) 203-214.

[239] L. Huang, K. Tao, J. Liu, C. Qi, L. Xu, P. Chang, J. Gao, X. Shuai, G. Wang, Z. Wang, Design and Fabrication of Multifunctional Sericin Nanoparticles for Tumor Targeting and pH-Responsive Subcellular Delivery of Cancer Chemotherapy Drugs, ACS applied materials & interfaces 8(10) (2016) 6577-6585.

[240] K. Patel, B.S. Raj, Y. Chen, X. Lou, Cytotoxicity of folic acid conjugated hollow silica nanoparticles toward Caco2 and 3T3 cells, with and without encapsulated DOX, Colloids and Surfaces B: Biointerfaces 140 (2016) 213-222.

[241] P. Hansakul, K. Aree, S. Tanuchit, A. Itharat, Growth arrest and apoptosis via caspase activation of dioscoreanone in human non-small-cell lung cancer A549 cells, BMC complementary and alternative medicine 14(1) (2014) 413.

[242] P. Allen, D. Davies, Apoptosis detection by flow cytometry, Flow Cytometry, Springer2007, pp. 147-163.

[243] M. Khan, S. Varadharaj, J.C. Shobha, M.U. Naidu, N.L. Parinandi, V.K. Kutala, P. Kuppusamy, C-phycocyanin ameliorates doxorubicin-induced oxidative stress and apoptosis in adult rat cardiomyocytes, Journal of cardiovascular pharmacology 47(1) (2006) 9-20.

[244] W. Tsang, S.P. Chau, S. Kong, K. Fung, T. Kwok, Reactive oxygen species mediate doxorubicin induced p53-independent apoptosis, Life sciences 73(16) (2003) 2047-2058.

[245] Y.-W. Eom, M.A. Kim, S.S. Park, M.J. Goo, H.J. Kwon, S. Sohn, W.-H. Kim, G. Yoon, K.S. Choi, Two distinct modes of cell death induced by doxorubicin: apoptosis and cell death through mitotic catastrophe accompanied by senescence-like phenotype, Oncogene 24(30) (2005) 4765-4777.

[246] Y. Patil, Y. Amitay, P. Ohana, H. Shmeeda, A. Gabizon, Targeting of pegylated liposomal mitomycin-C prodrug to the folate receptor of cancer cells: Intracellular activation and enhanced cytotoxicity, Journal of Controlled Release 225 (2016) 87-95.

[247] N. Ma, J. Liu, W. He, Z. Li, Y. Luan, Y. Song, S. Garg, Folic acid-grafted bovine serum albumin decorated graphene oxide: An efficient drug carrier for targeted cancer therapy, Journal of Colloid and Interface Science 490 (2017) 598-607.

[248] S. Sharifi, J. Barar, M.S. Hejazi, N. Samadi, Doxorubicin Changes Bax/Bcl-xL Ratio, Caspase-8 and 9 in Breast Cancer Cells, Advanced Pharmaceutical Bulletin 5(3) (2015) 351.

[249] M. Zhou, Y. Li, Q. Hu, X.-c. Bai, W. Huang, C. Yan, S.H. Scheres, Y. Shi, Atomic structure of the apoptosome: mechanism of cytochrome c-and dATP-mediated activation of Apaf-1, Genes & development 29(22) (2015) 2349-2361.

[250] S. Zhang, X. Liu, T. Bawa-Khalfe, L.-S. Lu, Y.L. Lyu, L.F. Liu, E.T. Yeh, Identification of the molecular basis of doxorubicin-induced cardiotoxicity, Nature medicine 18(11) (2012) 1639-1642.

[251] J. Shi, L. Zhang, Y.-W. Zhang, M. Surma, R.M. Payne, L. Wei, Downregulation of doxorubicin-induced myocardial apoptosis accompanies postnatal heart maturation, American Journal of Physiology-Heart and Circulatory Physiology 302(8) (2012) H1603-H1613.

[252] S. Fulda, K. Debatin, Extrinsic versus intrinsic apoptosis pathways in anticancer chemotherapy, Oncogene 25(34) (2006) 4798-4811.

[253] K. Huang, J. Zhang, K.L. O'Neill, C.B. Gurumurthy, R.M. Quadros, Y. Tu, X. Luo, Cleavage by caspase 8 and mitochondrial membrane association activate the BH3-only protein bid during TRAIL-induced apoptosis, Journal of Biological Chemistry 291(22) (2016) 11843-11851.

[254] E. Lorenzo, C. Ruiz-Ruiz, A.J. Quesada, G. Hernández, A. Rodríguez, A. López-Rivas, J.M. Redondo, Doxorubicin induces apoptosis and CD95 gene expression in human primary endothelial cells through a p53-dependent mechanism, Journal of Biological Chemistry 277(13) (2002) 10883-10892.

[255] Y. Shizukuda, S. Matoba, O.Y. Mian, T. Nguyen, P.M. Hwang, Targeted disruption of p53 attenuates doxorubicin-induced cardiac toxicity in mice, Molecular and cellular biochemistry 273(1) (2005) 25-32.

[256] S. Wang, E.A. Konorev, S. Kotamraju, J. Joseph, S. Kalivendi, B. Kalyanaraman, Doxorubicin induces apoptosis in normal and tumor cells via distinctly different

mechanisms intermediacy of H2O2-and p53-dependent pathways, Journal of Biological Chemistry 279(24) (2004) 25535-25543.

[257] H.S. El-Sawy, A.M. Al-Abd, T.A. Ahmed, K.M. El-Say, V.P. Torchilin, Stimuli-responsive nano-architecture drug-delivery systems to solid tumor micromilieu: past, present, and future perspectives, ACS nano 12(11) (2018) 10636-10664.

[258] H.G. Prigerson, Y. Bao, M.A. Shah, M.E. Paulk, T.W. LeBlanc, B.J. Schneider, M.M. Garrido, M.C. Reid, D.A. Berlin, K.B. Adelson, Chemotherapy use, performance status, and quality of life at the end of life, JAMA oncology 1(6) (2015) 778-784.

[259] A. Raza, T. Rasheed, F. Nabeel, U. Hayat, M. Bilal, H. Iqbal, Endogenous and exogenous stimuli-responsive drug delivery systems for programmed site-specific release, Molecules 24(6) (2019) 1117.

[260] J. Ge, E. Neofytou, T.J. Cahill III, R.E. Beygui, R.N. Zare, Drug release from electric-field-responsive nanoparticles, ACS nano 6(1) (2011) 227-233.

[261] G. Cirillo, U. Gianfranco Spizzirri, M. Curcio, S. Hampel, O. Vittorio, D. Restuccia, N. Picci, F. Iemma, Carbon nanohybrids as electro-responsive drug delivery systems, Mini reviews in medicinal chemistry 16(8) (2016) 658-667.

[262] Y. Cheng, C. He, J. Ding, C. Xiao, X. Zhuang, X. Chen, Thermosensitive hydrogels based on polypeptides for localized and sustained delivery of anticancer drugs, Biomaterials 34(38) (2013) 10338-10347.

[263] L. Zheng, C.e. Li, X. Huang, X. Lin, W. Lin, F. Yang, T. Chen, Thermosensitive hydrogels for sustained-release of sorafenib and selenium nanoparticles for localized synergistic chemoradiotherapy, Biomaterials 216 (2019) 119220.

[264] C. Liu, X. Guo, C. Ruan, H. Hu, B.-P. Jiang, H. Liang, X.-C. Shen, An injectable thermosensitive photothermal-network hydrogel for near-infrared-triggered drug delivery and synergistic photothermal-chemotherapy, Acta biomaterialia 96 (2019) 281-294.

[265] M.A.C. Stuart, W.T. Huck, J. Genzer, M. Müller, C. Ober, M. Stamm, G.B. Sukhorukov, I. Szleifer, V.V. Tsukruk, M. Urban, Emerging applications of stimuli-responsive polymer materials, Nature materials 9(2) (2010) 101.

[266] P.D. Thornton, A. Heise, Highly specific dual enzyme-mediated payload release from peptide-coated silica particles, Journal of the American Chemical Society 132(6) (2010) 2024-2028.

[267] X. Ling, J. Tu, J. Wang, A. Shajii, N. Kong, C. Feng, Y. Zhang, M. Yu, T. Xie, Z. Bharwani, Glutathione-responsive prodrug nanoparticles for effective drug delivery and cancer therapy, ACS nano 13(1) (2018) 357-370.

[268] T. Thambi, V. Deepagan, H.Y. Yoon, H.S. Han, S.-H. Kim, S. Son, D.-G. Jo, C.-H. Ahn, Y.D. Suh, K. Kim, Hypoxia-responsive polymeric nanoparticles for tumor-targeted drug delivery, Biomaterials 35(5) (2014) 1735-1743.

[269] Y. Namiki, T. Namiki, H. Yoshida, Y. Ishii, A. Tsubota, S. Koido, K. Nariai, M. Mitsunaga, S. Yanagisawa, H. Kashiwagi, A novel magnetic crystal–lipid nanostructure for magnetically guided in vivo gene delivery, Nature nanotechnology 4(9) (2009) 598.

[270] Y. Li, H. An, X. Wang, P. Wang, F. Qu, Y. Jiao, K. Zhang, Q. Liu, Ultrasound-triggered release of sinoporphyrin sodium from liposome-microbubble complexes and its enhanced sonodynamic toxicity in breast cancer, Nano Research 11(2) (2018) 1038-1056.

[271] L. Deng, Q. Li, S.a. Al-Rehili, H. Omar, A. Almalik, A. Alshamsan, J. Zhang, N.M. Khashab, Hybrid iron oxide–graphene oxide–polysaccharides microcapsule: a micro-matryoshka for on-demand drug release and antitumor therapy in vivo, ACS applied materials & interfaces 8(11) (2016) 6859-6868.

[272] P. Zhang, H. Huang, J. Huang, H. Chen, J. Wang, K. Qiu, D. Zhao, L. Ji, H. Chao, Noncovalent ruthenium (II) complexes–single-walled carbon nanotube composites for bimodal photothermal and photodynamic therapy with near-infrared irradiation, ACS applied materials & interfaces 7(41) (2015) 23278-23290.

[273] C. Guilbaud-Chéreau, B. Dinesh, R. Schurhammer, D. Collin, A. Bianco, C. Ménard-Moyon, Protected Amino Acid–Based Hydrogels Incorporating Carbon Nanomaterials for Near-Infrared Irradiation-Triggered Drug Release, ACS applied materials & interfaces 11(14) (2019) 13147-13157.

[274] C. Gao, P. Dong, Z. Lin, X. Guo, B.P. Jiang, S. Ji, H. Liang, X.C. Shen, Near-Infrared Light Responsive Imaging-Guided Photothermal and Photodynamic Synergistic Therapy Nanoplatform Based on Carbon Nanohorns for Efficient Cancer Treatment, Chemistry–A European Journal 24(49) (2018) 12827-12837.

[275] R. Borah, G.C. Ingavle, S.R. Sandeman, A. Kumar, S.V. Mikhalovsky, Amine-Functionalized Electrically Conductive Core–Sheath MEH-PPV: PCL Electrospun Nanofibers for Enhanced Cell–Biomaterial Interactions, ACS Biomaterials Science & Engineering 4(9) (2018) 3327-3346.

[276] J.P. Kumar, B.B. Mandal, Silk sericin induced pro-oxidative stress leads to apoptosis in human cancer cells, Food and chemical toxicology 123 (2019) 275-287.

[277] M. Zheng, H. Xu, X.-H. Liao, C.P. Chen, A.L. Zhang, W. Lu, L. Wang, D. Yang, J. Wang, H. Liu, Inhibition of the prolyl isomerase Pin1 enhances the ability of sorafenib to induce cell death and inhibit tumor growth in hepatocellular carcinoma, Oncotarget 8(18) (2017) 29771.

[278] N. Pilco-Ferreto, G.M. Calaf, Influence of doxorubicin on apoptosis and oxidative stress in breast cancer cell lines, International journal of oncology 49(2) (2016) 753-762.

[279] C. Soldani, A. Scovassi, Poly (ADP-ribose) polymerase-1 cleavage during apoptosis: an update, Apoptosis 7(4) (2002) 321-328.

[280] E. Szegezdi, U. Fitzgerald, A. Samali, Caspase-12 and ER-stress-mediated apoptosis: the story so far, Annals of the new York Academy of Sciences 1010(1) (2003) 186-194.

[281] C.G. Nebigil, L.G. Désaubry, Updates in anthracycline-mediated cardiotoxicity, Frontiers in Pharmacology 9 (2018) 1262.

[282] E.L. O'Callaghan, R.M. Lataro, E.L. Roloff, A.S. Chauhan, H.C. Salgado, E. Duncan, A. Nogaret, J.F.R. Paton, Enhancing respiratory sinus arrhythmia increases cardiac output in rats with left ventricular dysfunction, The Journal of Physiology 598(3) (2020) 455-471.

[283] Z. Zhao, Y. Li, M.-B. Xie, Silk fibroin-based nanoparticles for drug delivery, International journal of molecular sciences 16(3) (2015) 4880-4903.

[284] J.S. Im, B.C. Bai, Y.-S. Lee, The effect of carbon nanotubes on drug delivery in an electro-sensitive transdermal drug delivery system, Biomaterials 31(6) (2010) 1414-1419.

[285] M. Han, Z. Li, D. Bi, Y. Guo, H. Kuang, X. Wang, Novel folate-targeted docetaxel-loaded nanoparticles for tumour targeting: in vitro and in vivo evaluation, RSC advances 6(69) (2016) 64306-64314.

[286] A. Ivorra, B. Al-Sakere, B. Rubinsky, L.M. Mir, Use of conductive gels for electric field homogenization increases the antitumor efficacy of electroporation therapies, Physics in Medicine & Biology 53(22) (2008) 6605.

[287] T. Murakami, Photodynamic Action of Single-Walled Carbon Nanotubes, Chemical and Pharmaceutical Bulletin 65(7) (2017) 629-636.

[288] B.R.C.D. Menezes, K.F. Rodrigues, B.C.D.S. Fonseca, R.G. Ribas, T.L.D.A. Montanheiro, G.P. Thim, Recent advances in the use of carbon nanotubes as smart biomaterials, Journal of Materials Chemistry B 7(9) (2019) 1343-1360.

[289] V.E. Kagan, N.V. Konduru, W. Feng, B.L. Allen, J. Conroy, Y. Volkov, I.I. Vlasova, N.A. Belikova, N. Yanamala, A. Kapralov, Y.Y. Tyurina, J. Shi, E.R. Kisin, A.R. Murray, J. Franks, D. Stolz, P. Gou, J. Klein-Seetharaman, B. Fadeel, A. Star, A.A. Shvedova, Carbon nanotubes degraded by neutrophil myeloperoxidase induce less pulmonary inflammation, Nature Nanotechnology 5(5) (2010) 354-359.

[290] J. Hou, B. Wan, Y. Yang, X.-M. Ren, L.-H. Guo, J.-F. Liu, Biodegradation of Single-Walled Carbon Nanotubes in Macrophages through Respiratory Burst Modulation, 17(3) (2016) 409.

[291] D. Elgrabli, W. Dachraoui, H. De Marmier, C. Ménard-Moyon, D. Bégin, S. Bégin-Colin, A. Bianco, D. Alloyeau, F. Gazeau, Intracellular degradation of functionalized carbon nanotube/iron oxide hybrids is modulated by iron via Nrf2 pathway, Scientific reports 7(1) (2017) 1-13.

APPENDIX

APPENDIX

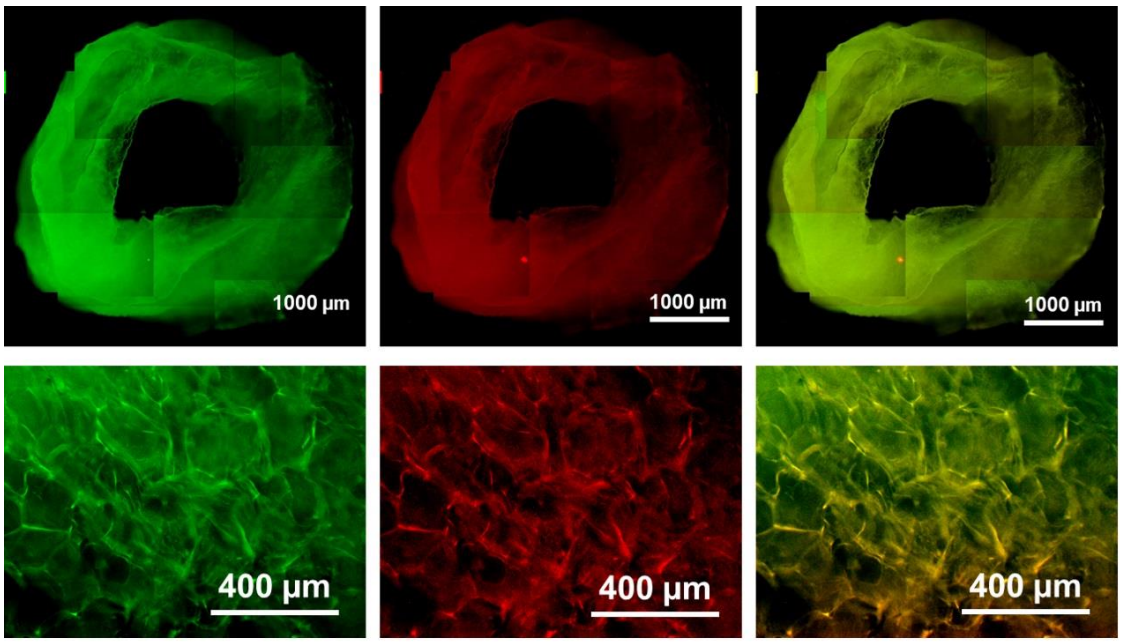

Figure A2.1. *Representative composite images showing green (left), red (middle) and merged (right) autofluorescence of silk scaffold. The top and bottom panel images were captured at low (4X) and high (40X) magnifications, respectively, using fluorescence microscope.*

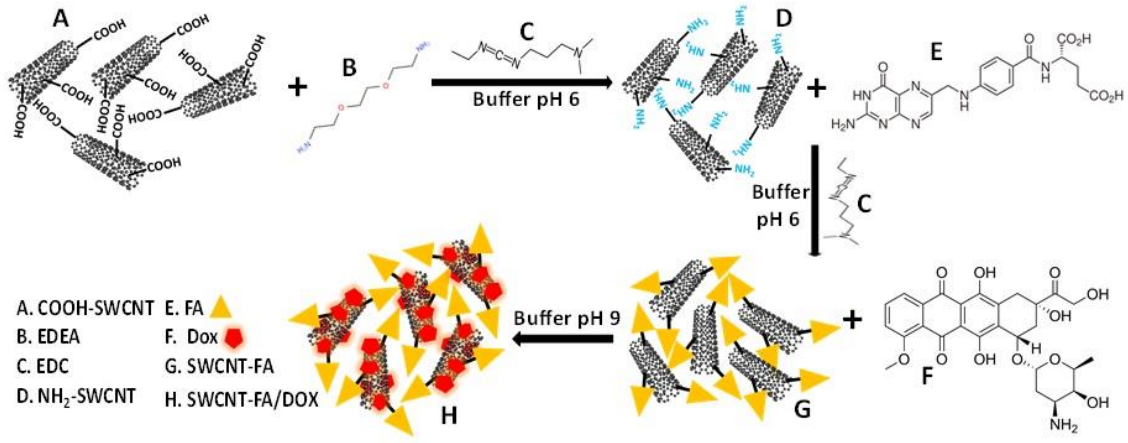

Figure A3.1. *Representation of FA functionalization of SWCNT and its loading with DOX.*

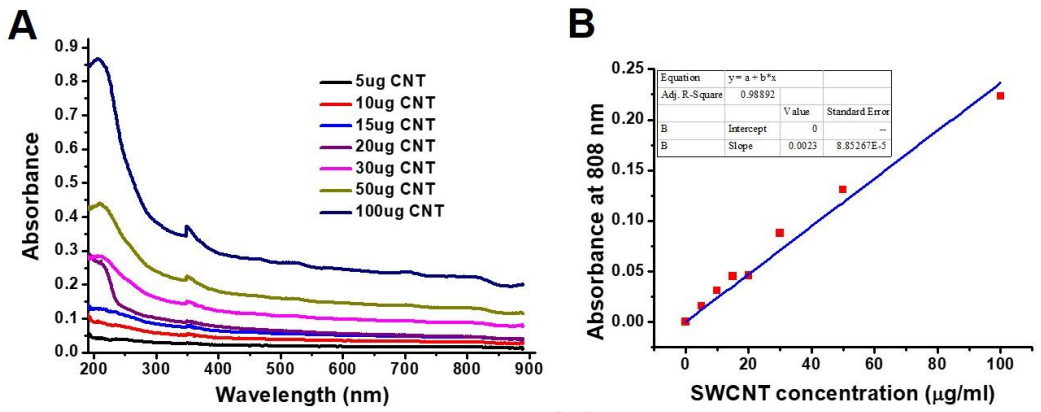

Figure A3.2. (A) *Absorbance scan at variable wavelength and (B) standard plot at 808 nm of increasing concentration of SWCNT.*

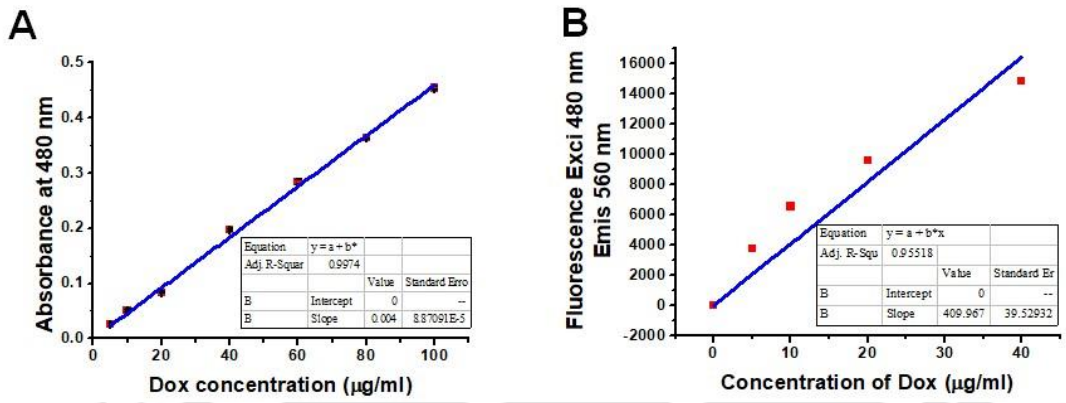

Figure A3.3. *Dox standard plot by (A) absorbance at 480 nm and (B) fluorescence by excitation at 480 nm and emission at 560 nm.*

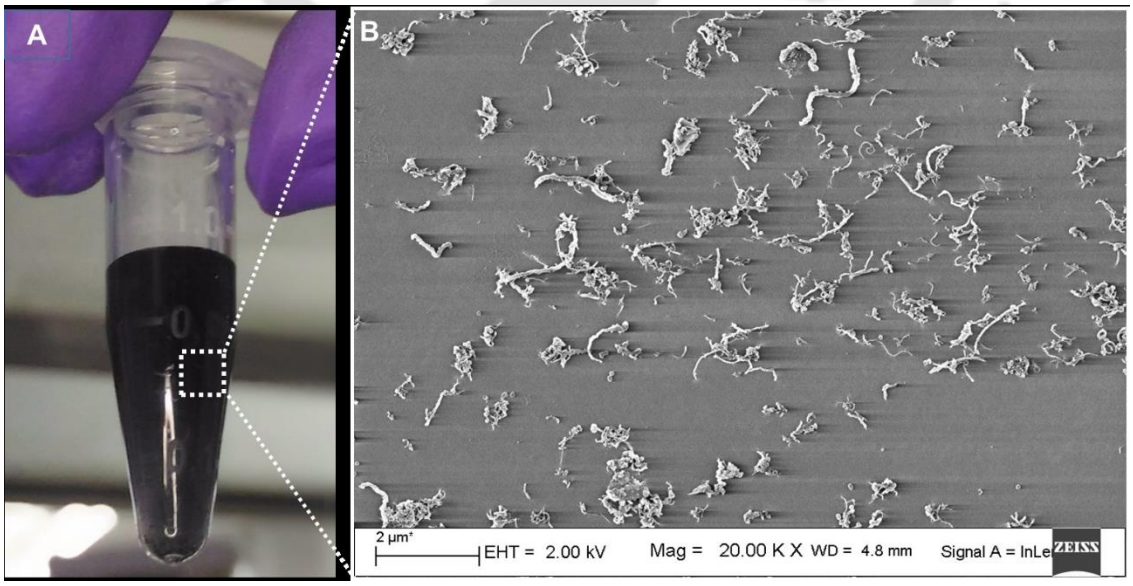

Figure A3.4. *Representation image of aqueous dispersed SWCNT (A) and its FESEM (B).*

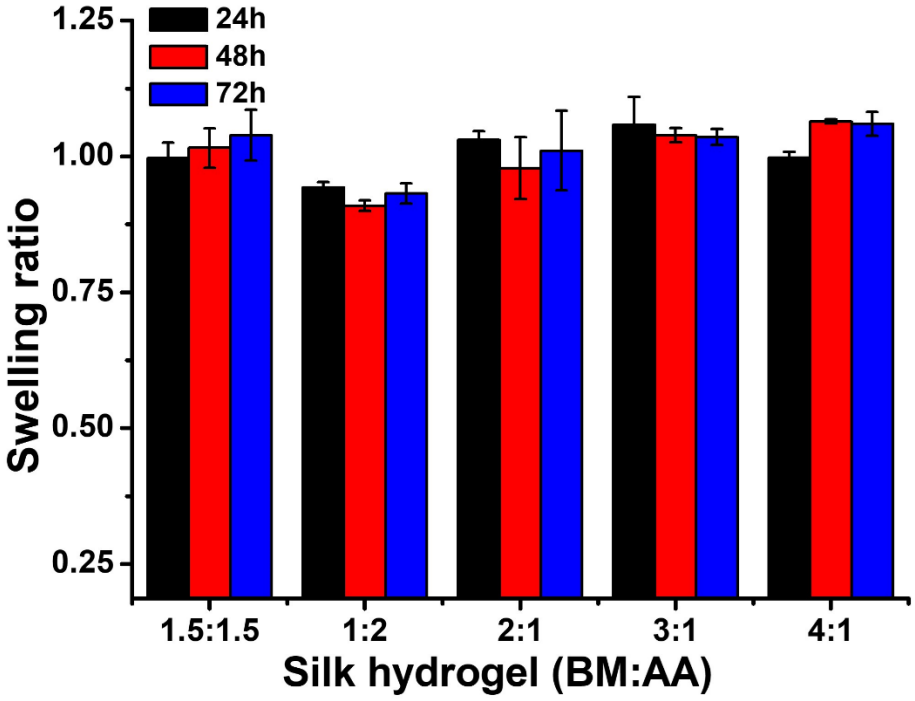

Figure A3.5. *Swelling of different ratio hydrogel into PBS till 72 h.*

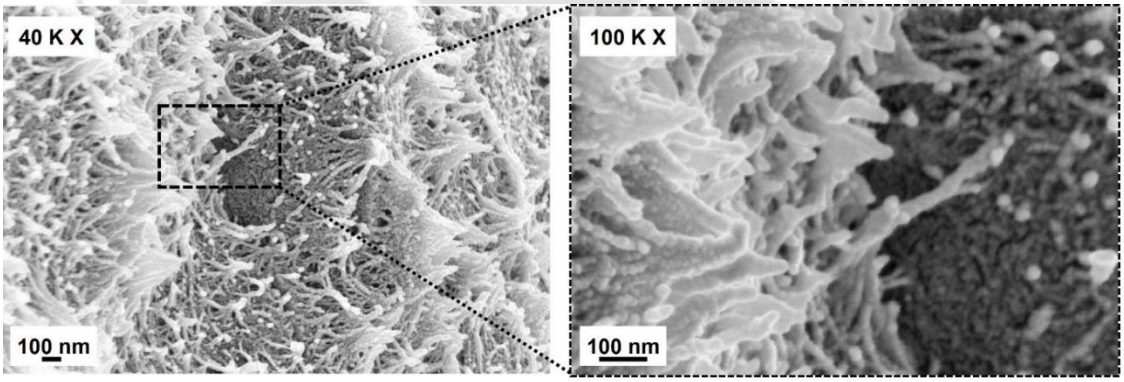

Figure A3.6. *Representative FESEM image of SWCNT embedded silk hydrogel.*

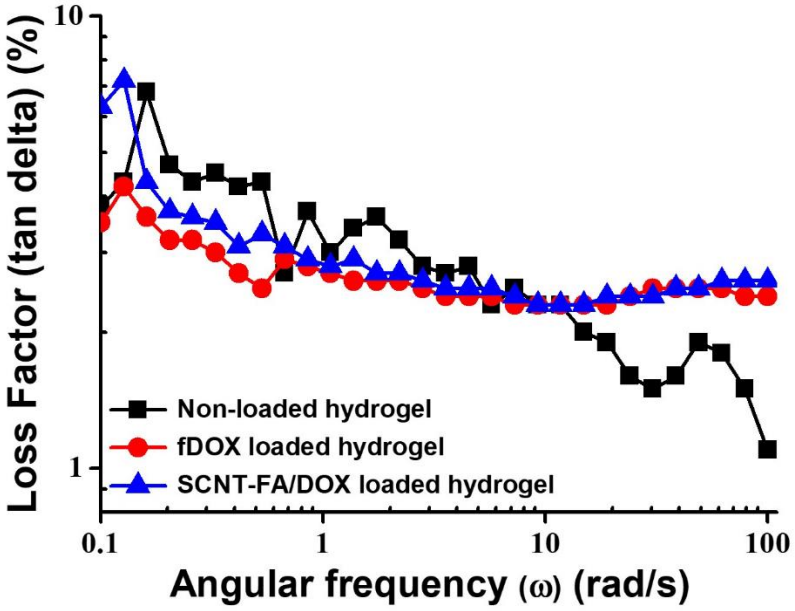

Figure A3.7. *Loss factor plot of SWCNT-FA/DOX, fDOX and non-loaded silk hydrogel.*

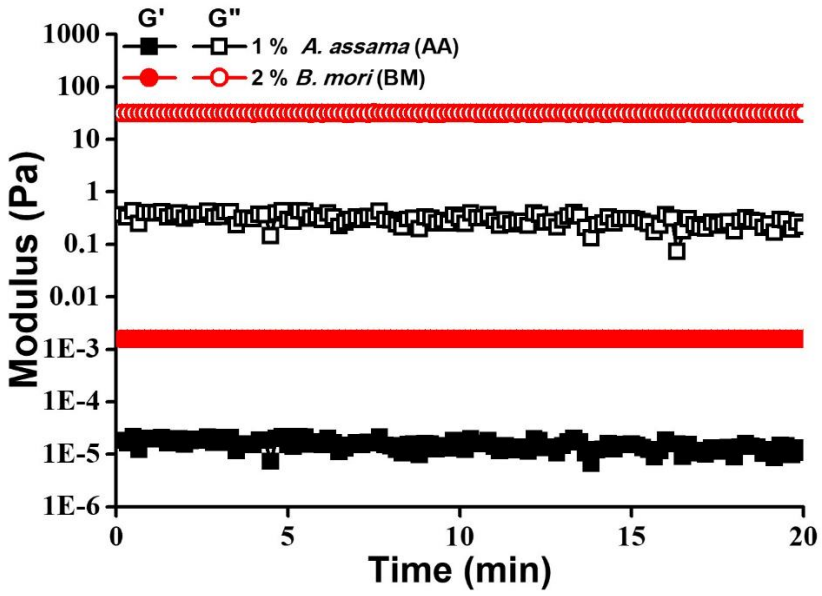

Figure A3.8. *BM and AA did not form the gel over time when exposed to 0.2% shear strain and 10 rad/s angular frequency in rheometer.*

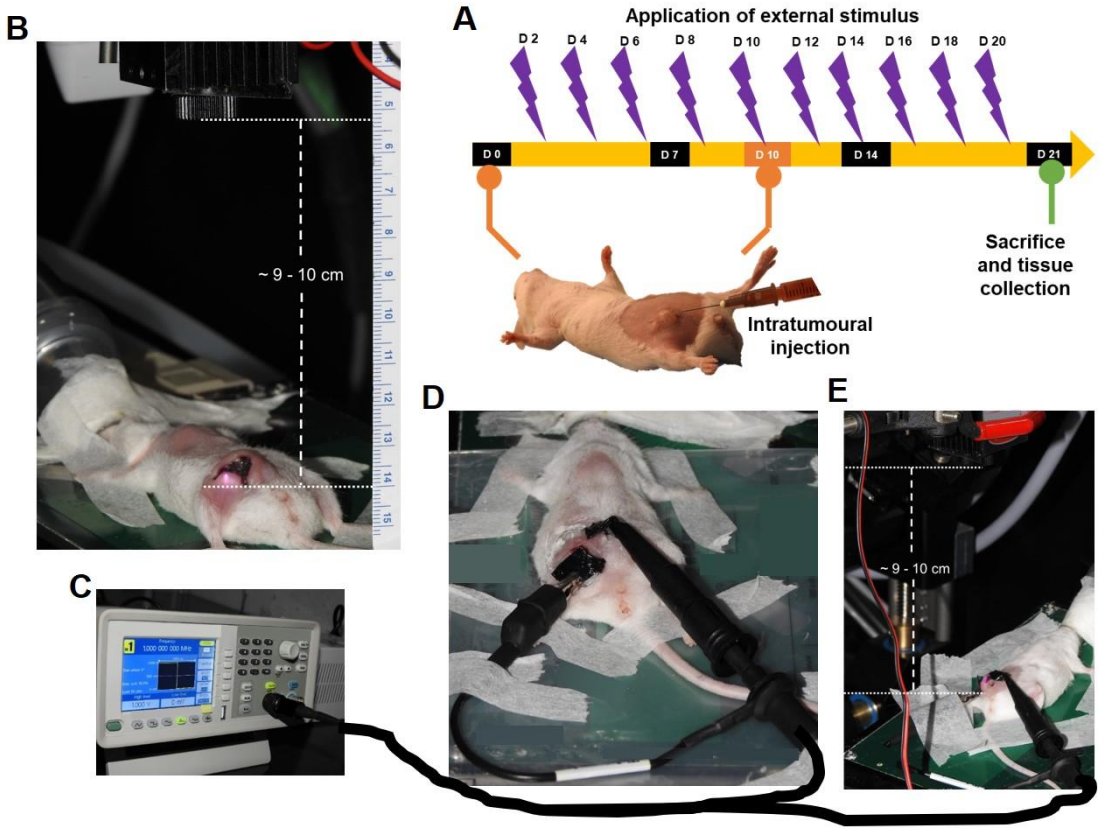

Figure A4.1. (A) *Breast cancer tumor was developed in Balb/c mice by directly injecting mice 4T1 breast cancer cell line in the fourth mammary fat pad. The tumor regression study started when the tumor volume reached 100 mm^3 and is considered as day 0. Tumour was continuously observed for 21 days, and ultrasound images were captured at days 0, 7, 14 and 21. Intratumor injection of Silk@fDOX to Group 3 animals and Silk@SWCNT-FA/DOX to Group 4, 5, 6 and 7 animals was administered twice at day 0 and day 10 during the study. NIR light and electrical voltage were externally applied both individually and simultaneously at each alternate day. Animals were sacrificed at day 21, and tumors, along with other tissues, were collected for further analysis. External setup of NIR laser* ***(B)*** *functional generator* ***(C)*** *for electrical stimulus applied alone on* ***(D)*** *and together with NIR laser in* ***(E)****.*

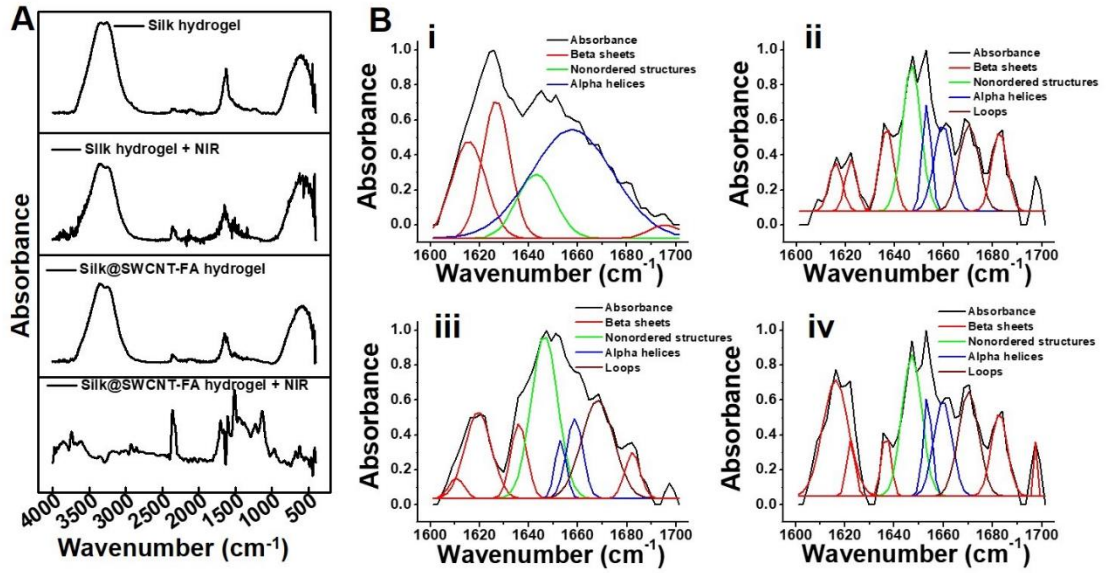

Figure A4.2. *(A) FTIR spectra from 400 cm^{-1} to 4000 cm^{-1} of silk and hydrogel with and without NIR laser exposure. (B) Representative deconvoluted amide I peaks of (i) silk hydrogel without NIR, (ii) with NIR, and (iii) Silk@SWCNT-FA nanocomposite hydrogel without NIR, (iv) with NIR laser exposure showing the secondary structure.*

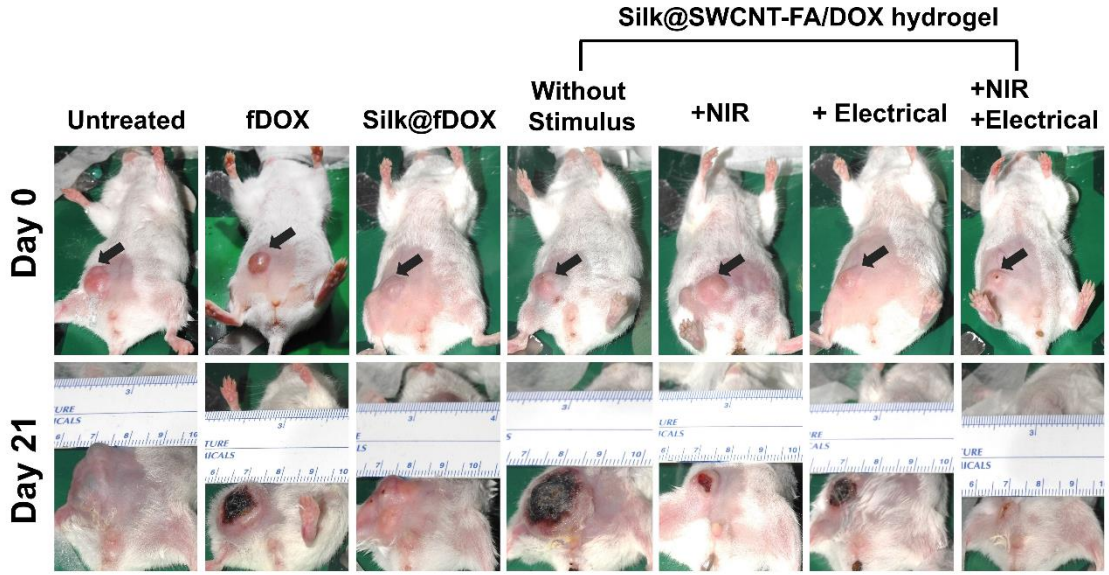

Figure A4.3. *The representative animals of all the groups were arranged, and picture was taken at the beginning (day 0) and end (day 21) of the experiment.*

LIST OF PUBLICATIONS

List of Publications

(A) Patent:

1. Biman B. Mandal and **Ankit Gangrade** "Injectable Nanocomposite Silk Hydrogel for Targeted and Controlled Delivery of Therapeutic Agents" [Indiian Patent file Application No. – 201931004799]

(B) Journal Publications from Ph.D. Thesis:

1. **Ankit Gangrade**, Basveshwar Gawali, Jadi Praveen Kumar, Vegi GM Naidu and Biman B. Mandal. "Photo-Electro Active Nanocomposite Silk Hydrogel for Spatiotemporal Controlled Release of Chemotherapeutics: An *In Vivo* Approach Towards Suppressing Solid Tumor Growth." ***ACS Applied Materials & Interfaces*** 12 (2020): 25, 27905–27916. **(IF – 8.758)**
2. **Ankit Gangrade** and Biman B. Mandal. "An Injectable Carbon Nanotube Impregnated Silk Based Multifunctional Hydrogel for Localized Targeted and On-Demand Anticancer Drug Delivery." ***ACS Biomaterials Science & Engineering*** 5, no. 5 (2019): 2365-2381. **(IF – 4.432)**
3. **Ankit Gangrade** and Biman B. Mandal. "Drug Delivery of Anticancer Drugs from Injectable 3D Porous Silk Scaffold for Prevention of Gastric Cancer Growth and Recurrence" ***ACS Biomaterials Science & Engineering*** (2020) 6, 11, 6195–6206. **(IF – 4.432)**
4. Janani Guru, Manishekhar Kumar, Dimple Chouhan, Joseph Christakiran Moses, **Ankit Gangrade**, Sohenii Bhattacharjee, and Biman B. Mandal. "Insight into Silk-Based Biomaterials: From Physicochemical Attributes to Recent Biomedical Applications." ***ACS Applied Bio Materials***, no. 2 (2019): 12, 5460-5491.

(C) Journal Publications from Collaborative Research Projects:

5. Khushwant Singh[$], **Ankit Gangrade**[$], Achintya Jana, Biman B. Mandal, and Neeladri Das. "Design, Synthesis, Characterization, and Antiproliferative Activity of Organoplatinum Compounds Bearing a 1, 2, 3-Triazole Ring." ***ACS Omega*** 4, no. 1 (2019): 835-841. **([$]Equal Contribution) (IF – 2.870)**

6. Khushwant Singh, **Ankit Gangrade**, Sourav Bhowmick, Achintya Jana, Biman B. Mandal, and Neeladri Das. "Self-Assembly of a [1+ 1] Ionic Hexagonal Macrocycle and Its Antiproliferative Activity." ***Frontiers in Chemistry,*** 6 (2018): 87. **(IF – 4.155)**
7. Sourav Bhowmick, Achintya Jana, Khushwant Singh, Prerak Gupta, **Ankit Gangrade**, Biman B. Mandal, and Neeladri Das. "Coordination-Driven Self-Assembly of Ionic Irregular Hexagonal Metallamacrocycles Via an Organometallic Clip and Their Cytotoxicity Potency." ***Inorganic Chemistry,*** 57, no. 7 (2017): 3615-3625. **(IF – 4.85)**
8. Jadi Praveen Kumar, Rocktotpal Konwarh, Manishekhar Kumar, **Ankit Gangrade**, and Biman B. Mandal. "Potential Nanomedicine Applications of Multifunctional Carbon Nanoparticles Developed Using Green Technology." ***ACS Sustainable Chemistry & Engineering,*** 6, no. 1 (2017): 1235-1245. **(IF – 7.632)**

(D) Book Chapter:

1. Joseph Christakiran M., **Ankit Gangrade** and Biman B. Mandal. "Carbon Nanotubes and Their Polymer Nanocomposites." *Nanomaterials and Polymer Nanocomposites: Raw Materials to Applications,* Elsevier, 2019. 145-175.

(E) Conferences/Workshops:

1. **Ankit Gangrade** and Biman B. Mandal. "Silk Fibroin Nanoparticle Embedded Injectable Silk Hydrogel for Sustained Delivery of Anticancer Drug." *International Conference on Advanced Nanomaterials and Nanotechnology (ICANN-2019), Organized by IIT Guwahati, 18-21st December 2019.* **(Poster Presentation).**
2. **Ankit Gangrade,** Basveshwar Gawali, Jadi Praveen Kumar, VGM Naidu and Biman B. Mandal. "Near-infrared and Electric Field Multi-responsive Silk Nanocomposite Hydrogel for Localized and Synergistic Tumor Therapy." *Nanobioteck 2019, Organized by Indian Society of Nanomedicine (ISNM) in partnership with the Department of Biotechnology (DBT), Govt. of India, from 21st – 23rd November 2019.* **(Oral Presentation).**

3. **Ankit Gangrade** and Biman B. Mandal. "Site-Specific On-Demand Delivery of Anticancer Drug Using Multi-Responsive Silk Based Nanocomposite Hydrogel." *Research Conclave 2019, Indian Institute of Technology Guwahati, 14-16th March 2019.* **(Poster Presentation).**
4. **Ankit Gangrade**, Participated in National Conference on "New Trends in Multi-Modal Molecular Imaging Applications for Animal Studies in Drug Discovery" *Organized by National Institute of Pharmaceutical Education and Research (NIPER) Guwahati, Assam, 20-21st November 2018.* **(Workshop Attended).**
5. **Ankit Gangrade** and Biman B. Mandal. "NIR/Electric Field Responsive Silk Nanocomposite Hydrogel for Localized On-Demand Anticancer Therapeutics Delivery." *Nanobioteck 2018, All India Institute of Medical Sciences (AIIMS, New Delhi), Organized by Indian Society of Nanomedicine (ISNM), 24-27th October 2018.* **(Poster Presentation).**
6. **Ankit Gangrade** and Biman B. Mandal. "Localized and Targeted Anticancer Drug Delivery Using Nano Hybrid Injectable Silk Hydrogel." *Research Conclave 2018, Indian Institute of Technology Guwahati, 8-11th March 2018.* **(Poster Presentation).**
7. **Ankit Gangrade** and Biman B. Mandal. "Dual-Stimuli Responsive Minimally Invasive Injectable Silk Hydrogel Loaded With Carbon Nanotubes for Localized Anticancer Drug Delivery." *International Conference on Advanced Nanomaterials and Nanotechnology (ICANN-2017), Organized by IIT Guwahati, 18-21st December 2017.* **(Poster Presentation).**
8. **Ankit Gangrade** and Biman B. Mandal. "Targeted Delivery of Anticancer Drug using Functionalized Carbon Nanotubes." *Research Conclave 2017, Indian Institute of Technology Guwahati, 16-19th March 2017.* **(Poster Presentation).**
9. **Ankit Gangrade**, Participated in 9th TCS annual event and flow cytometry workshop on "Flow Application in Basic, Applied and Clinical Biology (FABACTCS 2016)", *Organized by Indian Institute of Technology Guwahati, Guwahati, Assam from 03-05th November 2016.* **(Workshop Attended).**
10. **Ankit Gangrade** and Biman B. Mandal, "Folic Acid Functionalized Carbon Nanotubes for Cancer Targeted Drug Delivery." *Nanobioteck 2016, All India Institute of Medical Sciences (AIIMS, New Delhi), Organized by Indian Society of Nanomedicine (ISNM), 24-26th November 2016.* **(Poster Presentation).** (Best Poster Award)

(F) Media Highlights:

1. **IIT Guwahati researchers develop nature-derived nanomaterial for targeted delivery of cancer drugs.** Covered on 25th & 26th September 2019, by 10+ press release including, *The Times of India*, *ET Health World*, *India Today*, *BW Education*, *India Education Diary*, *Careers360*, *World News In Click*, *The Times of India - Education Times*, *Medical Buyer*, *The India Saga*, and *Shiksha*.

   https://timesofindia.indiatimes.com/home/education/news/iit-guwahati-researchers-develop-nature-derived-nanomaterials-for-targeted-delivery-of-cancer-drugs/articleshow/71304041.cms

2. **Silk Based Hydrogels May Help In Localized And Targeted Cancer Drug Delivery**, *SCISOUP* Blog on JUL 10, 2020.

   http://www.scisoup.org/article/2020/silk-based-hydrogels-may-help-in-localized-and-targeted-cancer-drug-delivery.html

3. **YouTube video explaining our work**

   https://www.youtube.com/watch?v=LHFP01YC15s&t=9s